Supporting Information

Design of Dy^{III} single-molecule magnets with molecularly installed luminescent thermometers based on bridging $[Pt^{II}(CN)_2(C^N)]^-$ complexes

Pawel J. Bonarek,[a] Mikolaj Zychowicz,[ab] Jan Rzepiela,[ab] Michal Liberka,[ab] Sebastian Baś,[a] Jakub J. Zakrzewski,*[ab] and Szymon Chorazy*[a]

[a]Faculty of Chemistry, Jagiellonian University, Gronostajowa 2, 30-387 Krakow, Poland

[b]Doctoral School of Exact and Natural Sciences, Jagiellonian University, Łojasiewicza 11, 30-348 Kraków, Poland

Corresponding authors: j.zakrzewski@uj.edu.pl; simon.chorazy@uj.edu.pl

Experimental details

Materials

Dysprosium(III) nitrate *n*-hydrate, ($Dy^{III}(NO_3)_3 \cdot nH_2O$, CAS: 100641-13-2; Sigma-Aldrich), yttrium(III) nitrate hexahydrate ($Y^{III}(NO_3)_3 \cdot 6H_2O$ CAS: 13494-98-9; Sigma-Aldrich), 4(1H)-pyridone (4-pyone, CAS: 108-96-3, Sigma-Aldrich), pyridazin-4(1H)-one (4-pydzone, CAS: 17417-57-1; Sigma-Aldrich), potassium cyanide (KCN, CAS: 151-50-8, Sigma-Aldrich), potassium tetrachloroplatinate(II) ($K_2[PtCl_4]$, CAS: 10025-99-7, abcr GmbH), tetrabutylammonium bromide (TBABr, CAS: 1643-19-2; Sigma-Aldrich), silver perchlorate ($AgClO_4$, CAS: 7783-93-9; Sigma-Aldrich), magnesium sulfate ($MgSO_4$, CAS: 7487-88-9; Sigma-Aldrich), 2-phenylpyridine (Hppy, CAS: 1008-89-5; Sigma-Aldrich), 4-methoxypyridine (CAS: 620-08-6; Sigma-Aldrich), iodomethane (CAS: 74-88-4; Sigma-Aldrich), tetrabutylammonium perchlorate ($TBAClO_4$, CAS: 1923-70-2; Sigma-Aldrich), and all organic solvents purchased from commercial sources were used without further purification. Note that the commercial *n*-hydrate of dysprosium(III) nitrate was used for which the number of water of crystallization is stated not to be stable, thus depends on the external conditions, mainly a humidity level; however, the number of water molecules is expected to oscillate around hexahydrate which is the typical form for nitrates of heavier lanthanide(3+) ions. Therefore, for the calculations of synthetic procedures, the composition with six water molecules per Dy(III) center was used. We found that the small variation of the real used amount of this Dy(III) salt, which could have appeared depending on the humidity conditions, did not change the final products, having also a negligible impact on the related synthetic yields. Tetrabutylammonium dicyanido(2-phenylpyridinato)platinate(II), $TBA[Pt^{II}(CN)_2(ppy)]$, and *N*-methyl-pyridin-4(1H)-one (4-Mepyone) were synthesized by optimizing previously reported methods (see below).[S1–S3]

Synthesis of $TBA[Pt^{II}(CN)_2(ppy)]$

The synthesis was performed as follows by optimizing literature procedures.[S1,S2] An aqueous solution of $K_2[Pt^{II}Cl_4]$ (0.12 $mol \cdot dm^{-3}$) was mixed with an identical volume of an aqueous solution of TBABr (0.26 $mol \cdot dm^{-3}$). Then, the resulting tetrabutylammonium tetrachloroplatinate(II), $TBA_2[Pt^{II}Cl_4]$, was extracted with dichloromethane, DCM (7-fold excess to water). Next, the organic phase was dried with anhydrous $MgSO_4$ and evaporated to obtain a red oily product, which was dissolved in anhydrous ethanol (volume equal to the volume of DCM used at the previous stage), together with one-quarter of its amount of DCM. To the obtained solution, 2-phenylpyridine (Hppy) was added (1:0.95 molar ratio of ligand to $K_2[Pt^{II}Cl_4]$). The mixture was stirred for 7 days at room temperature, which resulted in a color change from red to yellowish green. Then, a precipitate was separated by filtration, the solution was evaporated to about 30% of the original volume, and a 6-fold excess of diethyl ether was added. The mixture was left overnight to precipitate $[Pt^{II}_2(\mu\text{-}Cl)_2(ppy)_2]$, which was filtered, dried in the air, and weighed. In the following step, the product was suspended in acetonitrile, MeCN (6 $mg \cdot mL^{-1}$), and was mixed with the MeCN solution of silver(I) perchlorate (15 $mmol \cdot dm^{-3}$) of equal volume. After stirring for 7 hours at room temperature in the dark, the impurities and by-products were filtered off, the solution was evaporated to dryness, and the separated product, i.e., $[Pt^{II}(MeCN)_2(ppy)]ClO_4$, was washed with diethyl ether, then dried and weighed. The compound was dissolved in methanol (55 $mmol \cdot dm^{-3}$), combined with an identical volume of methanolic solution of potassium cyanide (110 $mmol \cdot dm^{-3}$), and stirred for an hour. The precipitated $KClO_4$ was filtered off and the solution was evaporated to dryness. The collected yellow product, $K[Pt^{II}(CN)_2(ppy)]$, was dissolved in acetone (4/3 volume of the evaporated methanol). To the solution, $TBAClO_4$ (1:1 molar ratio to the complex) was added and the resulting mixture was stirred for an hour, after which $KClO_4$ was filtered off, the solution was evaporated to dryness, then the final product was washed with water. It was purified by dissolving in DCM and precipitation of yellow needle-shaped crystals of the objective precursor, $TBA[Pt^{II}(CN)_2(ppy)]$ (its crystal structure was tested by the single-crystal X-ray diffraction, SC-XRD, experiment which gave the data identical to the literature)[S2], was caused by the addition of diethyl ether excess. However, the final product obtained after additional recrystallization was found to be still contaminated by the small amount of $TBAClO_4$ as shown by the CHN elemental analyses. We found that these contaminations varied depending on the synthesis but had no influence on the crystallization of the reported materials of **1**–**4**. To ensure the integrity of the presented approach, in all the syntheses, we always used the

amount of the precursor assuming negligibly small amounts of impurity checking in several syntheses that the resulting products are identical and the synthetic yields are also only slightly affected. IR spectra for TBA[$Pt^{II}(CN)_2(ppy)$]: literature ν (cm^{-1}):[S2] 2122 (vs, C≡N), 2110 (vs, C≡N), 1604 (s), 1581 (m), 1560 (m), 885 (m, TBA^+), 778 (s), 745 (m); experimental ν (cm^{-1}): 2123 (vs), 2111 (vs), 1608 (s), 1583 (m), 1563 (m), 1483 (s), 1092 (vs), 887 (m), 774 (s), 744 (m).

Synthesis of 4-Mepyone ligand

The synthesis of the 4-Mepyone ligand was performed according to the procedure presented in Scheme 1 below, based on the synthesis described by Beak and Bonham.[S3] To the ACE pressure vessel, a 2.470 ml portion of 4-methoxypyridine was added (2.66g, 24.4 mmol, 1 eq.) together with a catalytic amount of iodomethane (300 mg, 0.132 ml, 2.1 mmol, 0.086 eq). The reactor was tightly closed and the resulting solution was stirred and heated overnight at 130°C. After colling down to room temperature iodomethane was evaporated under the fume hood, and yellowish crystals of the product were formed. Then, the final compound was purified by column chromatography on an alumina gel with chloroform elution. The resulting product was obtained as colorless crystals with an 81% yield (2.16 g, 19.8 mmol).
^{1}H NMR (400 MHz, $CDCl_3$, Me_4Si) δ: 7.35 (d, J = 7.6 Hz, 2H), 6.33 (d, J = 7.7 Hz, 2H), 3.69 (s, 3H).
$^{13}C\{^1H\}$ NMR (101 MHz, $CDCl_3$, Me_4Si) δ: 178.6, 140.9, 118.5, 43.6.

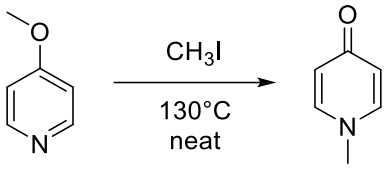

Scheme 1 Synthesis of *N*-methylpyridin-4(1H)-one, 4-Mepyone.

Synthesis of 1

A solution containing 32.1 mg (ca. 0.5 mmol) of TBA[$Pt^{II}(CN)_2(ppy)$] in 1 mL of acetonitrile and a methanolic solution (2 mL) of $Dy^{III}(NO_3)_3{\cdot}nH_2O$ (11.4 mg, ca. 0.25 mmol) were separately prepared. Both were added together to a narrow and tall vial, and the resulting mixture was layered with ca. 4 mL of diethyl ether. Within ca. 5 days, yellow crystals of **1** appeared. Their composition, $\{[Dy^{III}(MeOH)_2(NO_3)]_2[Pt^{II}(CN)_2(ppy)]_4\}{\cdot}2MeCN{\cdot}2.5Et_2O$ (**1**), was determined based on the results of the SC-XRD experiment. The crystals are stable only in the mother solution, the similar-to-synthesis mixed-solvent solution, or when covered by a protective grease (e.g., Apiezon® N grease). In the air, the non-coordinated organic solvent molecules are gradually exchanged with water which presumably leads to structural modification; however, this was not investigated further as all crucial physical studies were performed on well-protected samples of **1**. For the air-dried material of the expected formula of $\{[Dy^{III}(MeOH)_2(NO_3)][Pt^{II}(CN)_2(ppy)]_2\}{\cdot}H_2O$, the water content was established based on CHN elemental analysis. Calculated: C, 30.3%; H, 2.4%; N, 8.8%; found: C, 30.3%; H, 2.6%; N, 8.7%. M_W = 1109.2 g/mol; yield (based on Dy): 20%.

Synthesis of 2

A solution containing 32.1 mg (ca. 0.5 mmol) of TBA[$Pt^{II}(CN)_2(ppy)$] in 1 mL of acetonitrile, a methanolic solution (1 mL) of $Dy^{III}(NO_3)_3{\cdot}nH_2O$ (11.4 mg, ca. 0.25 mmol), and an acetonitrile (1 mL) solution containing 4.8 mg of 4-pyone were separately prepared. They were added together to a narrow and tall vial in the order of Ln^{III} salt, ligand, and Pt^{II} salt, and the resulting mixture (after a few minutes of stirring) was layered with ca. 4 mL of diethyl ether. Within ca. 5 days, yellow crystals of **2** appeared. Their composition, $\{[Dy^{III}(MeOH)(NO_3)(4\text{-pyone})][Dy^{III}(NO_3)(4\text{-pyone})_2][Pt^{II}(CN)_2(ppy)]_4\}{\cdot}1.5MeCN{\cdot}2MeOH$ (**2**), was determined based on the results of the SC-XRD experiment. The crystals are stable only in the mother solution, the similar-to-synthesis mixed-solvent solution, or when covered by a protective grease (e.g., Apiezon® N grease). In the air, the non-coordinated organic solvent molecules are gradually exchanged with water which presumably leads to structural modification; however, this was not investigated further as all crucial physical studies were performed on well-protected samples of **2**. For the air-dried material of the expected formula of

{[Dy^{III}(MeOH)(NO_3)(4-pyone)][Dy^{III}(NO_3)(4-pyone)$_2$][Pt^{II}($CN)_2$(ppy)]$_4$}·2H_2O, the water content was established based on CHN elemental analysis. Calculated: C, 33.9%; H, 2.3%; N, 9.9%; found: C, 34.1%; H, 2.4%; N, 10.0%. M_W = 2407.6 g/mol; yield (based on Dy): 42%.

Synthesis of 3

A solution containing 32.1 mg (ca. 0.5 mmol) of TBA[Pt^{II}($CN)_2$(ppy)] in 1 mL of acetonitrile, a methanolic solution (1 mL) of $Dy^{III}(NO_3)_3 \cdot n H_2O$ (11.4 mg, ca. 0.25 mmol), and an acetonitrile (1 mL) solution containing 4.8 mg of 4-pydzone were separately prepared. They were added together to a narrow and tall vial in the order of Ln^{III} salt, ligand, 100 μL of DMF, and Pt^{II} salt, and the resulting mixture (after a few minutes of stirring) was layered with ca. 4 mL of diethyl ether. Within ca. 5 days, yellow crystals of **3** appeared. Their composition, {[Dy^{III}(MeOH)(NO_3)(4-pydzone)][Dy^{III}(NO_3)(4-pydzone)$_2$][Pt^{II}($CN)_2$(ppy)]$_4$}·MeCN·2MeOH·0.5Et_2O (**3**), was determined based on the results of the SC-XRD experiment. The crystals are stable only in the mother solution, the similar-to-synthesis mixed-solvent solution, or when covered by a protective grease (e.g., Apiezon® N grease). In the air, the non-coordinated organic solvent molecules are gradually exchanged with water which presumably leads to structural modification; however, this was not investigated further as all crucial physical studies were performed on well-protected samples of **3**. For the air-dried material of the expected formula of {[Dy^{III}(MeOH)(NO_3)(4-pydzone)][Dy^{III}(NO_3)(4-pydzone)$_2$][Pt^{II}($CN)_2$(ppy)]$_4$}·2H_2O, the water content was established based on CHN elemental analysis. Calculated: C, 32.4%; H, 2.2%; N, 11.6%; found: C, 32.8%; H, 2.5%; N, 11.2%. M_W = 2410.6 g/mol; yield (based on Dy): 13%.

Synthesis of 4

A solution containing 32.1 mg (ca. 0.5 mmol) of TBA[Pt^{II}($CN)_2$(ppy)] in 1 mL of acetonitrile, a methanolic solution (1 mL) of $Dy^{III}(NO_3)_3 \cdot n H_2O$ (11.4 mg, ca. 0.25 mmol), and an acetonitrile (1 mL) solution of containing 5.5 mg of 4-Mepyone were separately prepared. They were added together to a narrow and tall vial in the order of Ln^{III} salt, ligand, 100 μL of DMF, and Pt^{II} salt, and the resulting mixture (after a few minutes of stirring) was layered with ca. 4 mL of diethyl ether. Within ca. 5 days, yellow crystals of **4** appeared. Their composition, {[Dy^{III}(4-Mepyone)$_2$(NO_3)]$_2$[Pt^{II}($CN)_2$(ppy)]$_4$}·0.5MeCN·2MeOH (**4**), was determined based on the results of the SC-XRD experiment. The crystals are stable only in the mother solution, the similar-to-synthesis mixed-solvent solution, or when covered by a protective grease (e.g., Apiezon® N grease). In the air, the non-coordinated organic solvent molecules are gradually exchanged with water which presumably leads to structural modification; however, this was not investigated further as all crucial physical studies were performed on well-protected samples of **4**. For the air-dried material of the expected formula of {[Dy^{III}(4-Mepyone)$_2$(NO_3)][Pt^{II}($CN)_2$(ppy)]$_2$}·H_2O, the water content was established based on CHN elemental analysis. Calculated: C, 36.1%; H, 2.6%; N, 10.0%; found: C, 36.0%; H, 2.7%; N, 9.9%. M_W = 1263.4 g/mol; yield (based on Dy): 53%.

Syntheses of magnetically diluted samples, 1md, 2md, 3md, and 4md

All magnetically diluted samples of compounds **1–4** (**1md**–**4md**) were prepared analogously as their non-diluted derivatives. For this purpose, the starting amounts of the salts of Dy^{3+} and Y^{3+} ions used for all syntheses of diluted samples were adjusted to have 5% for Dy(III) salt and 95% for Y(III) salt in molar percentages counting 100% for the whole amount of the lanthanide salts. Similar behavior and time of crystallization were observed for **1md**–**4md** as were found for the original syntheses. Despite this, the final ratio between these two lanthanides within the obtained crystalline phases had to be determined on the air-dried samples using the EDX-MA method on an SEM microscope (see below). The resulting compositions, depicted by the percentage of Dy(III) centers, the respective samples are as follows. **1md**, 4.84(95)%; **2md**, 5.04(50)%; **3md**, 6.42(54)%; **4md**, 4.21(51)%.

X-ray crystallography

Single-crystal X-ray diffraction (SC-XRD) analyses for **1**–**3** were performed on a Bruker D8 Venture diffractometer equipped with Photon III CPAD detector, Mo Kα INCOATEC IμS 3.0 microfocus sealed tube radiation source, and

Helios® optics while those for **4** was performed on a Bruker D8Quest Eco Photon50 CMOS diffractometer equipped with the graphite monochromated MoKα radiation (Table S1). For the SC-XRD studies, the selected single crystals of **1–4** were covered by Apiezon® N grease and mounted onto the Micro Mounts™ holders. The measurements were performed at 100(2) K, the data reduction and cell refinement were performed using SAINT and SADABS programs, and the crystal structures were solved using a direct method using a SHELXT-2014/5 program integrated within the Apex4 software.[S4,S5] All crystal structures were refined following a weighted full-matrix least-squares method on F^2 on SHELX-2018/3 within the WinGX ver. 2014/1 integrated system.[S6] All non-hydrogen atoms were refined anisotropically. The hydrogen atoms of the organic ligands and those bonded to C-atoms of solvent molecules were calculated at the idealized positions and refined using a riding model. The H-atoms of the hydroxyl groups of solvent molecules were found from the electron density map and also refined using the riding model. A few restraints (ISOR and DELU) were applied for non-hydrogen atoms to ensure the convergence of the refinement procedure and maintain the proper coordination geometry. The crystallographic data were deposited in the CCDC database. Deposition numbers are 2287738–2287741 for **1**–**4**, respectively. The detailed parameters of crystal data and structure refinement are presented in Table S1 while the representative structural parameters of the obtained models are shown in Table S2. The structural Fig. were prepared by using the Mercury 3.10.3 software. Powder X-ray diffraction (P-XRD) patterns of all samples were collected on a Bruker D8Advance Eco diffractometer equipped with CuKα radiation (λ = 1.5418 Å) on the polycrystalline samples closed in glass capillaries under the respective mother liquors.

Physical techniques

The physical measurements related to crucial magnetic and optical properties were performed on the polycrystalline solid-state samples of the investigated compounds that were washed and covered by the solution composed of methanol, acetonitrile, and diethyl ether in the 2:1:4 ratio, in which these compounds exhibit the identical structure and composition as found in the SC-XRD experiment. In such a manner magnetic properties were measured for the samples sealed in glass tubes under vacuum. These tubes were further mounted into the plastic straws inserted into the magnetometer. Both alternate- (*ac*) and direct-current (*dc*) magnetic data were collected using a Quantum Design MPMS-3 Evercool magnetometer.

Temperature-variable photoluminescent studies were performed using an FS5 spectrofluorometer (Edinburgh Instruments) equipped with an excitation source in the form of a Xe (150 W) arc lamp and an R928P Hamamatsu photomultiplier as a signal detector, while the emission lifetime measurements employed an FS5 multichannel scaling module with a Xe flash lamp (5 W). Such measurements utilized a CS204SI-FMX-1SS cooling power optical He cryostat (Advanced Research Systems, Inc.) equipped with a DE-204SI closed-cycle cryo-cooler (cold head), a water-cooled He compressor (ARS-4HW model), and a model 335 cryogenic temperature controller (Lake Shore Cryotronics). The respective samples were sealed under solution in plastic bags, covered in vacuum grease, and mounted between two quartz plates. The absolute emission quantum yields were determined using the samples under solution in plastic bags. This was done following a direct excitation method using an integrating sphere module for the FS5 spectrofluorometer, based on the procedure described previously.[S7]

The ^{1}H and ^{13}C{^{1}H} NMR spectra were recorded for the proper solutions of investigated organic compounds with Me_4Si as an internal standard at room temperature using Jeol 400 MHz ECZR spectrometer. Infrared (IR) absorption spectra measured for the air-dried polycrystalline samples of **1**–**4** were collected on a Thermo Scientific Nicolet iN10 Fourier transform infrared (FTIR) microscope in the 4000–700 cm^{-1} range, while the UV-vis-NIR absorption spectra were recorded in a transmission mode for the thin films of powder samples dispersed between two quartz plates in paraffin oil, using a Shimadzu 3600i Plus UV-vis-NIR spectrophotometer. The thermogravimetric (TG) analysis, CHNS elemental analysis, and the determination of the Dy/Y ratios for the magnetically diluted samples (**1md**–**4md**) were performed on the air-dried powder samples. For the TG analysis under a nitrogen atmosphere, a Netzsch TG 209 F1 Libra apparatus was used, the CHNS analysis employed an Elementar Vario Micro Cube CHNS analyzer, and the Dy/Y ratios were determined using a Hitachi S-4700 SEM microscope equipped with an energy-dispersive X-ray (EDX) NORAN Vintage microanalysis (MA) system.

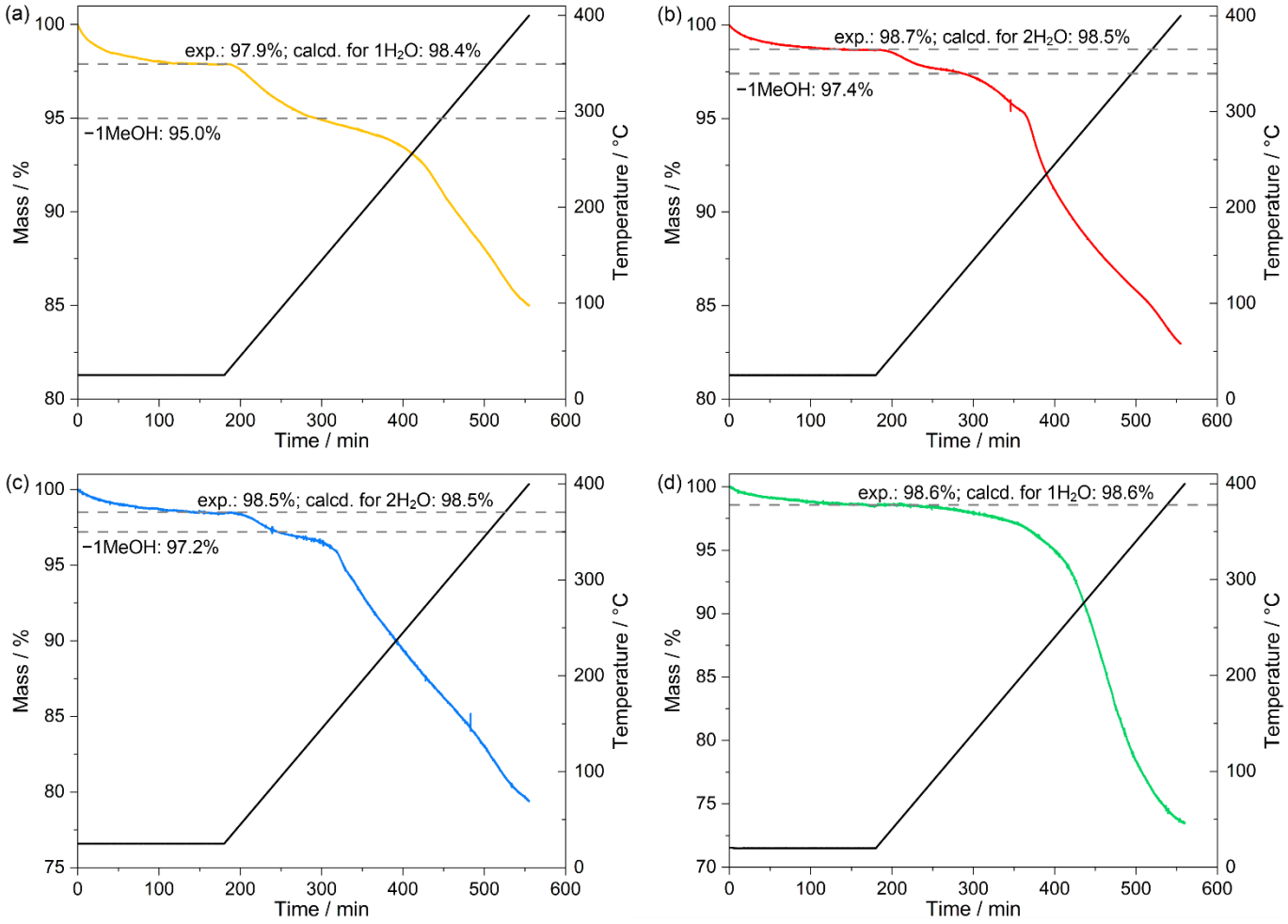

Fig. S1 Thermogravimetric curves for compounds **1–4** (a–d, respectively). Before the start of heating (as visualized on the graphs), the samples were dried for 3 hours in the flow of dry nitrogen, which resulted in the removal of the weakly bonded water molecules. The results show that all the compounds are hydrated when exposed to an air atmosphere and readily lose all of the non-coordinated solvent molecules. This is confirmed by CHN analysis and IR spectra (see Experimental details and Fig. S2). The grey, dashed lines mark steps corresponding to the loss of water molecules and, later, coordinated methanol. Note that in the case of **1** (a), the removals of 1 H_2O and 1 MeOH per the formula unit are indicated on the graph while the formula contains 2 MeOH molecules. The removal of the second MeOH molecule per the formula unit is expected to appear at a higher temperature but it presumably leads to the overall decomposition of the sample giving a broad weight loss instead of the clear step of the mass decrease. Thus, this step was not indicated on the graph.

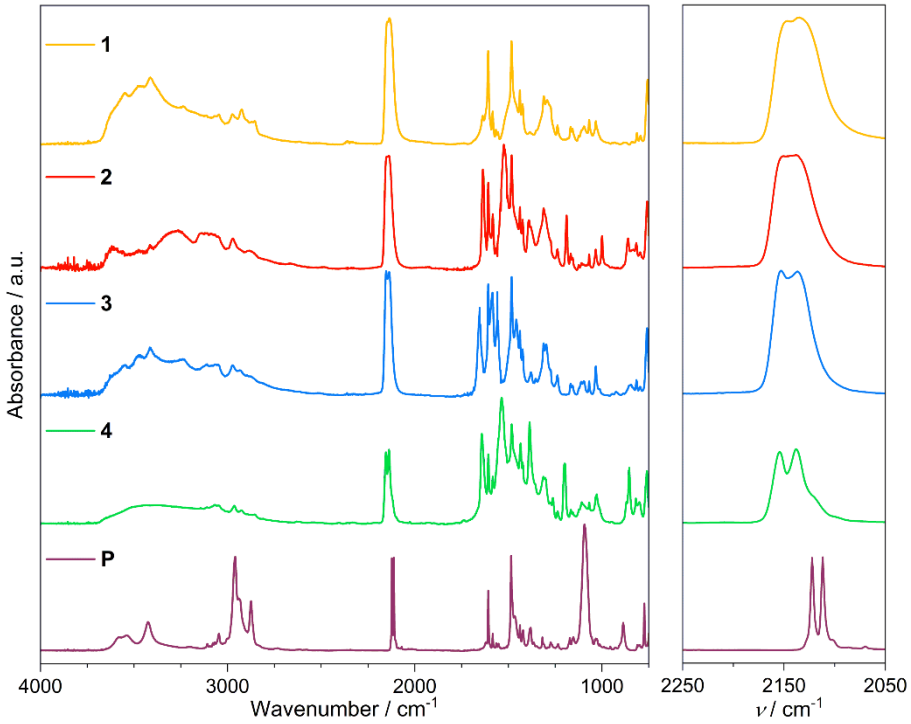

Fig. S2 The IR absorption spectra of compounds **1**–**4** and the TBA[$Pt^{II}(CN)_2(ppy)$] precursor (marked here as **P**). The cyanido-related bands are presented on the right side of the figure. For **1**–**4**, they are wider and situated at higher energies when compared with the precursor. It indicates that cyanides act as bridging ligands. None of the spectra shows an additional band related to acetonitrile, expected around 2250 cm^{-1}. There is no signal originating from OH vibrations of methanol molecules around 3500 cm^{-1} for the IR spectra of **4**. However, for the whole series of **1**–**4**, a broad band related to H-bonded water molecules (3300 cm^{-1}) is visible, as well as methanol-related bands are found for **1**–**3**. This agrees well with the determined compositions and their changes in the air (i.e., the exchange of non-coordinated organic solvent molecules with water, see Experimental details). Note that for the precursor **P**, the analogous IR peaks also appear above at higher wavenumbers than 3000 cm^{-1}; they can be also assigned to water molecules as the precursor was found to be hygroscopic, thus the investigated crystals by the IR spectra can contain such water molecules.

Table S1 Details of crystal data and structure refinement for **1**–**4**.

compound	**1**	**2**	**3**	**4**
CCDC number	2287738	2287739	2287740	2287741
formula	$Dy_8Pt_{16}C_{282}H_{321}N_{64}O_{50}$	$Dy_4Pt_8C_{145}H_{125.5}N_{36.5}O_{24}$	$Dy_4Pt_8C_{142}H_{128}N_{42}O_{25}$	$Dy_4Pt_8C_{157}H_{120}N_{37}O_{23}$
formula weight / g·mol^{-1}	9828.45	4974.03	5033.58	5103.61
T / K	100(2)			
λ / Å	0.71075 (Mo Kα)			
crystal system	monoclinic	triclinic		monoclinic
space group	$P2_1/c$	$P\bar{1}$		$P2_1/n$
a / Å	26.9547(13)	15.8627(11)	15.7982(13)	16.0526(9)
b / Å	15.9063(7)	17.3706(13)	17.3783(15)	19.3915(10)
c / Å	19.2062(10)	18.0173(13)	17.8978(15)	27.7623(15)
α / deg	90	99.150(2)	98.509(3)	90
β / deg	90.203(2)	112.085(2)	111.678(3)	95.115(2)
γ / deg	90	108.731(2)	109.076(3)	90
V / Å^3	8234.6(7)	4129.3(5)	4108.6(6)	8607.5(8)
Z	4	1	1	2
ρ_{calc} / g·cm^{-3}	1.982	2.012	2.034	1.969
μ / cm^{-1}	8.626	8.603	8.649	8.257
F(000)	4637	2346	2362	4786
crystal type	green block			
crystal size / mm × mm × mm	0.11 × 0.07 × 0.06	0.16 × 0.09 × 0.07	0.15 × 0.06 × 0.04	0.09 × 0.06 × 0.03
θ range /deg	1.981–26.402	2.116–25.026	2.132–25.027	2.287–25.027
limiting indices	-33 < h < 33 -18 < k < 19 -24 < l < 24	-18 < h < 18 -20 < k < 20 -21 < l < 21	-18 < h < 18 -20 < k < 20 -21 < l < 21	-19 < h < 19 -22 < k < 23 -32 < l < 33
collected reflections	79263	70093	71111	71781
unique reflections	16758	14584	14517	15151
R_{int}	0.0532	0.0787	0.0725	0.0801
completeness / %	99.3	99.9	99.8	99.7
data/parameters/restraints	16758/980/0	14584/1034/140	14517/1043/40	15143/1072/521
GOF on F^2	1.085	1.12	1.053	1.198
final R indices [$I \geq 2\sigma(I)$]	R_1 = 0.0365, wR_2 = 0.0745	R_1 = 0.0528, wR_2 = 0.1157	R_1 = 0.046, wR_2 = 0.1037	R_1 = 0.1245, wR_2 = 0.2834
final R indices (all data)	R_1 = 0.0437, wR_2 = 0.0773	R_1 = 0.0663, wR_2 = 0.1217	R_1 = 0.0589, wR_2 = 0.1108	R_1 = 0.1466, wR_2 = 0.2923
largest diff. (peak/hole) / e·Å^{-3}	3.724/–1.932	2.818/–2.044	3.978/–3.332	8.305/–4.444

Comment to Table S1 – the SC-XRD data for compound 4

As can be deduced from Table S1, the R_{int} value (0.0801) for compound **4** is not significantly worse (larger) than for the other compounds (0.053–0.079 range); however, the final *R* indices are significantly higher. It is important to note here that within the refinement procedure for this compound, we found a lot of relatively large residual electron density peaks that could not be reasonably assigned to any atoms as they are situated too close to the other atoms at positions too short for the chemically accessible bond lengths. These peaks are due to the relatively bad quality of the crystals for this compound, in particular, they are signs of the significant twinning of the crystals and the general structural disorder related to relatively weak interactions between coordination chains for this compound. We attempted to perform the twinning refinement for the crystals of this compound but the related procedures were not successful due to the complicated relationships between the twinning components. We found this twinning issue for all the crystals of this compound so we checked several crystals and selected the best-quality data for the presentation in the article.

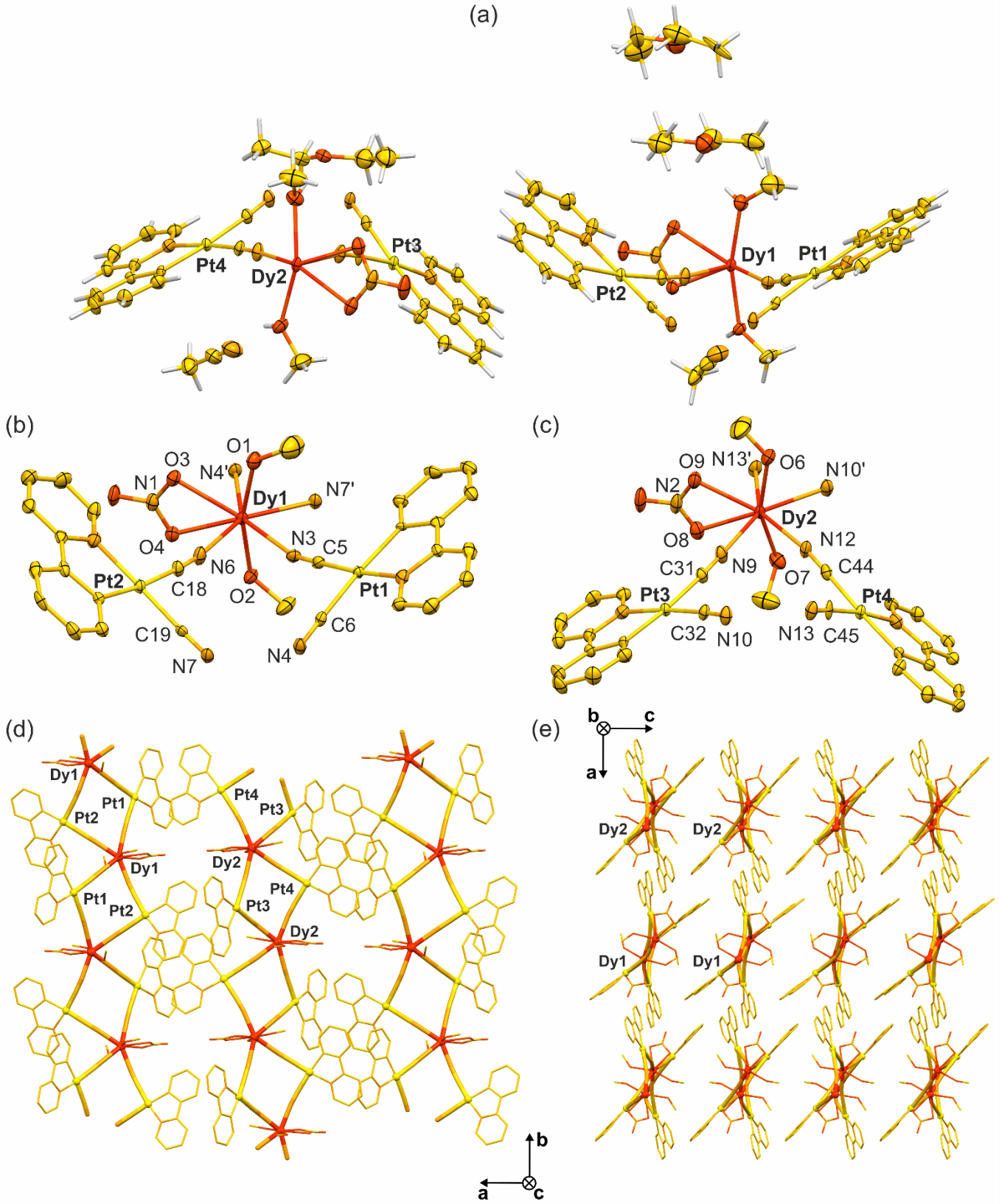

Fig. S3 Supplementary structural views of the crystal structure of **1**: (a) the asymmetric unit, (b,c) the insights into the coordination sphere of the two symmetrical independent Dy(III) complexes, presented together with the atoms labeling scheme, (d) the projection of the structure along the *c* axis, positioned perpendicular to the supramolecular layers of the $\{Dy_2Pt_4\}_n$ coordination chains, and (e) the projection of the structure along the *b* axis, which is in parallel to the direction of the expansion of the $\{Dy_2Pt_4\}_n$ chains, showcasing their packing within the crystal structure. The thermal ellipsoids of non-hydrogen atoms in (a–c) are presented at the 50% probability level. For clarity, hydrogen atoms and solvent molecules are omitted in (b–e).

Table S2 Detailed structural parameters of Dy(III) complexes in **1**.

Dy1		**Dy2**	
distances			
Dy1–O1 / Å	2.320(5)	Dy2–O6 / Å	2.314(5)
Dy1–O2 / Å	2.337(5)	Dy2–O7 / Å	2.347(6)
Dy1–O3 / Å	2.459(4)	Dy2–O9 / Å	2.470(5)
Dy1–O4 / Å	2.458(5)	Dy2–O8 / Å	2.436(5)
Dy1–N4 / Å	2.412(6)	Dy2–N13 / Å	2.429(6)
Dy1–N7 / Å	2.452(5)	Dy2–N10/ Å	2.419(6)
Dy1–N3 / Å	2.429(5)	Dy2–N12 / Å	2.428(6)
Dy1–N6 / Å	2.424(6)	Dy2–N9 / Å	2.406(6)
angles			
O1–Dy1–O2 / °	163.98(17)	O6–Dy2–O7 / °	157.75(18)
O1–Dy1–N1 / °	98.35(18)	O6–Dy2–N2 / °	100.5(2)
O1–Dy1–N4 / °	92.6(2)	O6–Dy2–N13 / °	97.1(2)
O1–Dy1–N7 / °	83.86(19)	O6–Dy2–N10 / °	81.1(2)
O1–Dy1–N3 / °	84.14(19)	O6–Dy2–N12 / °	82.3(2)
O1–Dy1–N6 / °	91.3(2)	O6–Dy2–N9 / °	85.2(2)
O2–Dy1–N1 / °	97.16(17)	O7–Dy2–N2 / °	99.7(2)
O2–Dy1–N4 / °	88.93(19)	O7–Dy2–N13 / °	98.2(2)
O2–Dy1–N7 / °	81.41(18)	O7–Dy2–N10 / °	88.7(2)
O2–Dy1–N3 / °	85.31(18)	O7–Dy2–N12 / °	71.73(18)
O2–Dy1–N6 / °	97.3(2)	O7–Dy2–N9 / °	91.7(2)
O3–Dy1–N4 / °	72.35(17)	O9–Dy2–N13 / °	71.73(18)
O3–Dy1–N6 / °	73.09(17)	O9–Dy2–N9 / °	74.37(19)
O4–Dy1–N4 / °	72.53(18)	O8–Dy2–N13 / °	74.21(19)
O4–Dy1–N6 / °	74.38(18)	O8–Dy2–N9 / °	75.73(19)
N4–Dy1–N7 / °	72.28(18)	N13–Dy2–N10 / °	71.26(19)
N7–Dy1–N3 / °	71.85(18)	N10–Dy2–N12 / °	72.38(19)
N3–Dy1–N6 / °	73.72(18)	N12–Dy2–N9 / °	72.76(19)

Table S3 Results of Continuous Shape Measure (CShM) analysis for eight-coordinated Dy(III) complexes in the crystal structure of **1**.

Dy(III) center	CShM parameters*					Determined geometry
	SAPR-8	TDD-8	JBTPR-8	BTPR-8	JSD-8	
Dy1	3.855	**1.719**	3.292	2.777	2.620	TDD-8
Dy2	3.634	**1.757**	3.205	2.642	2.832	TDD-8

*CShM parameters:

CShM SAPR-8 – the parameter related to the square antiprism geometry (D_{4d} symmetry)

CShM TDD-8 – the parameter related to the triangular dodecahedron geometry (D_{2d} symmetry)

CShM JBTPR-8 – the parameter related to the J50 biaugmented trigonal prism geometry (C_{2v} symmetry)

CShM BTPR-8 – the parameter related to the biaugmented trigonal prism geometry (C_{2v} symmetry)

CShM JSD-8 – the parameter related to the J84 snub diphenoid geometry (D_{2d} symmetry)

The value of CShM = 0 is ascribed to the ideal geometry. The increase of the CShM parameter above 0 represents the increasing distortion from the ideal polyhedron.[S8,S9]

Additional remark. We performed additional CShM calculations for the hypothetical Dy(III) coordination sphere, analogous to those found for Dy1 and Dy2 centers of **1** but replacing two O-atoms of a nitrate ion with a single O-atom placed in the center of the distance between these two O-atoms. As a result, we could treat the resulting coordination sphere as a real seven-coordinated one. Then, we checked the resulting CShM parameters corresponding to the pentagonal bipyramidal geometry; they are 0.508 and 0.940 for Dy1 and Dy2 centers, indicating that, with this approach, the coordination spheres are close to an ideal pentagonal bipyramidal geometry, as was suggested by the structural views (Fig. 1).

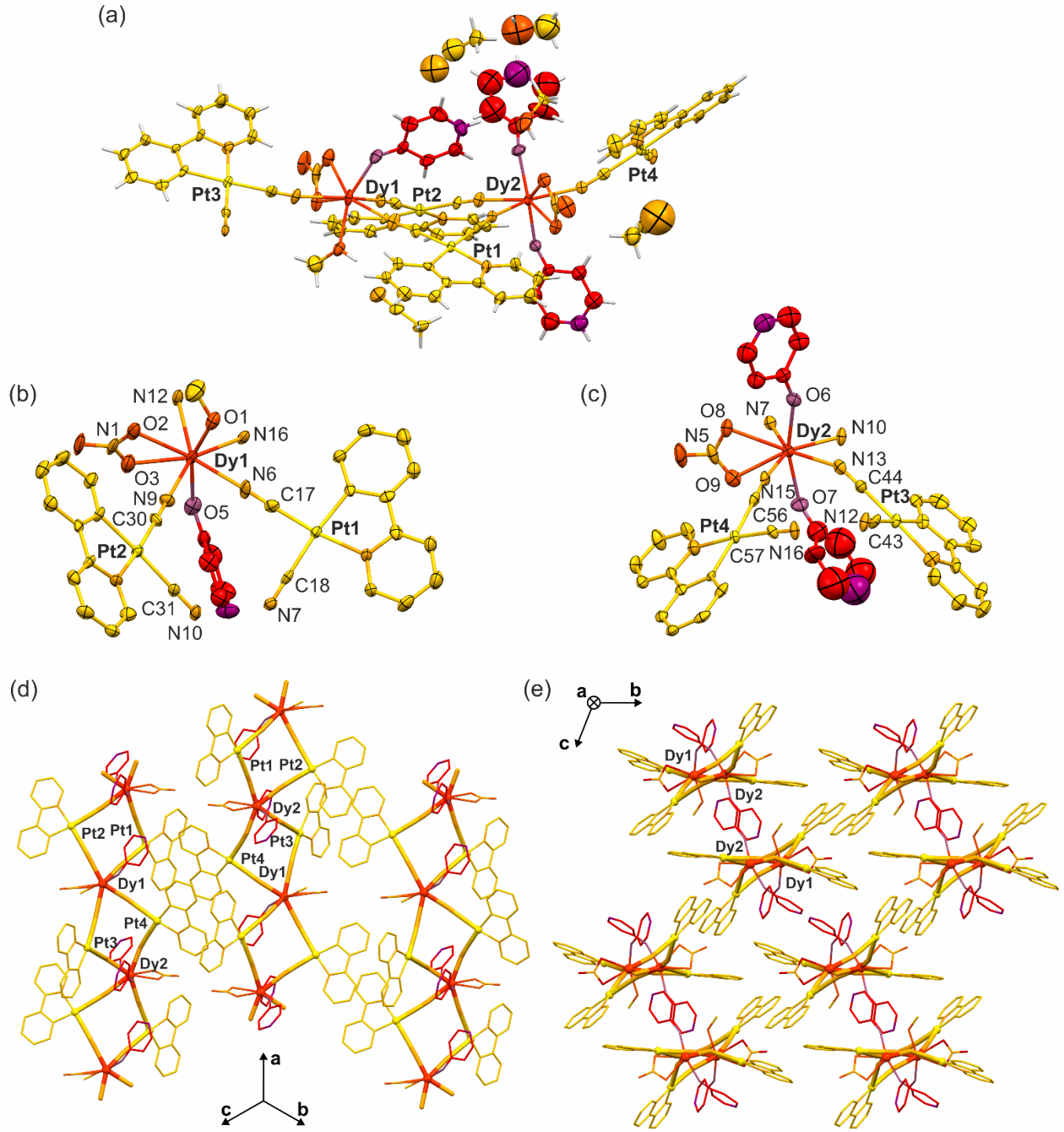

Fig. S4 Supplementary structural views of the crystal structure of **2**: (a) the asymmetric unit, (b,c) the insights into the coordination sphere of the two symmetrically independent Dy(III) complexes, presented together with the atoms labeling scheme, (d) the projection of the structure along the [111] direction, positioned perpendicular to the supramolecular layers of the $\{Dy_2Pt_4\}_n$ chains, and € the projection of the structure along the *a* axis, which is in parallel to the direction of the expansion of the $\{Dy_2Pt_4\}_n$ chains, showcasing their packing within the crystal structure. The thermal ellipsoids of non-hydrogen atoms in (a–c) are presented at the 50% probability level. For clarity, hydrogen atoms and solvent molecules are omitted in (b–e).

Table S4 Detailed structural parameters of Dy(III) complexes in **2**.

Dy1		**Dy2**	
distances			
Dy1–O1 / Å	2.329(10)	Dy2–O6 / Å	2.214(8)
Dy1–O5 / Å	2.281(10)	Dy2–O7 / Å	2.258(9)
Dy1–O2 / Å	2.530(9)	Dy2–O8 / Å	2.503(8)
Dy1–O3 / Å	2.439(10)	Dy2–O9 / Å	2.465(9)
Dy1–N12 / Å	2.435(10)	Dy2–N15 / Å	2.454(10)
Dy1–N16 / Å	2.450(10)	Dy2–N13 / Å	2.517(11)
Dy1–N6 / Å	2.416(11)	Dy2–N10 / Å	2.452(10)
Dy1–N9 / Å	2.413(10)	Dy2–N7 / Å	2.431(11)
angles			
O1–Dy1–O5 / °	155.6(3)	O6–Dy2–O7 / °	161.6(3)
O1–Dy1–N1 / °	101.4(4)	O6–Dy2–N5 / °	101.2(4)
O1–Dy1–N12 / °	82.3(4)	O6–Dy2–N15 / °	91.4(3)
O1–Dy1–N16 / °	90.5(4)	O6–Dy2–N13 / °	82.8(3)
O1–Dy1–N6 / °	75.1(4)	O6–Dy2–N10 / °	88.1(3)
O1–Dy1–N9 / °	89.1(4)	O6–Dy2–N7 / °	92.8(3)
O5–Dy1–N1 / °	99.7(4)	O7–Dy2–N5 / °	96.5(4)
O5–Dy1–N12 / °	116.0(3)	O7–Dy2–N15 / °	88.7(3)
O5–Dy1–N16 / °	81.6(3)	O7–Dy2–N13 / °	79.6(3)
O5–Dy1–N6 / °	80.6(4)	O7–Dy2–N10 / °	81.2(4)
O5–Dy1–N9 / °	86.0(3)	O7–Dy2–N7 / °	98.2(3)
O2–Dy1–N12 / °	69.9(3)	O8–Dy2–N15 / °	74.2(3)
O2–Dy1–N9 / °	70.3(3)	O8–Dy2–N7 / °	71.5(3)
O3–Dy1–N12 / °	76.2(3)	O9–Dy2–N15 / °	76.0(3)
O3–Dy1–N9 / °	78.3(3)	O9–Dy2–N7 / °	72.3(3)
N12–Dy1–N16 / °	70.4(3)	N15–Dy2–N13 / °	72.8(3)
N16–Dy1–N6 / °	74.0(3)	N13–Dy2–N10 / °	71.9(3)
N6–Dy1–N9 / °	75.9(4)	N10–Dy2–N7 / °	72.5(3)

Table S5 Results of Continuous Shape Measure (CShM) analysis for eight-coordinated Dy(III) complexes in the crystal structure of **2**.

Dy(III) center	CShM parameters*					Determined geometry
	SAPR-8	TDD-8	JBTPR-8	BTPR-8	JSD-8	
Dy1	2.879	2.571	1.994	**1.345**	3.737	BTPR-8
Dy2	3.846	**1.880**	2.800	2.587	2.407	TDD-8

*CShM parameters:

CShM SAPR-8 – the parameter related to the square antiprism geometry (D_{4d} symmetry)

CShM TDD-8 – the parameter related to the triangular dodecahedron geometry (D_{2d} symmetry)

CShM JBTPR-8 – the parameter related to the J50 biaugmented trigonal prism geometry (C_{2v} symmetry)

CShM BTPR-8 – the parameter related to the biaugmented trigonal prism geometry (C_{2v} symmetry)

CShM JSD-8 – the parameter related to the J84 snub diphenoid geometry (D_{2d} symmetry)

The value of CShM = 0 is ascribed to the ideal geometry. The increase of the CShM parameter above 0 represents the increasing distortion from the ideal polyhedron.[S8,S9]

Additional remark. We performed additional CShM calculations for the hypothetical Dy(III) coordination sphere, analogous to those found for Dy1 and Dy2 centers of **2** but replacing two O-atoms of a nitrate ion with a single O-atom placed in the center of the distance between these two O-atoms. As a result, we could treat the resulting coordination sphere as a real seven-coordinated one. Then, we checked the resulting CShM parameters corresponding to the pentagonal bipyramidal geometry; they are 2.202 and 0.727 for Dy1 and Dy2 centers, indicating that, with this approach, the coordination sphere of Dy2 is close to an ideal pentagonal bipyramidal geometry, as was suggested by the structural views (Fig. 1), while those for Dy1 is more distorted.

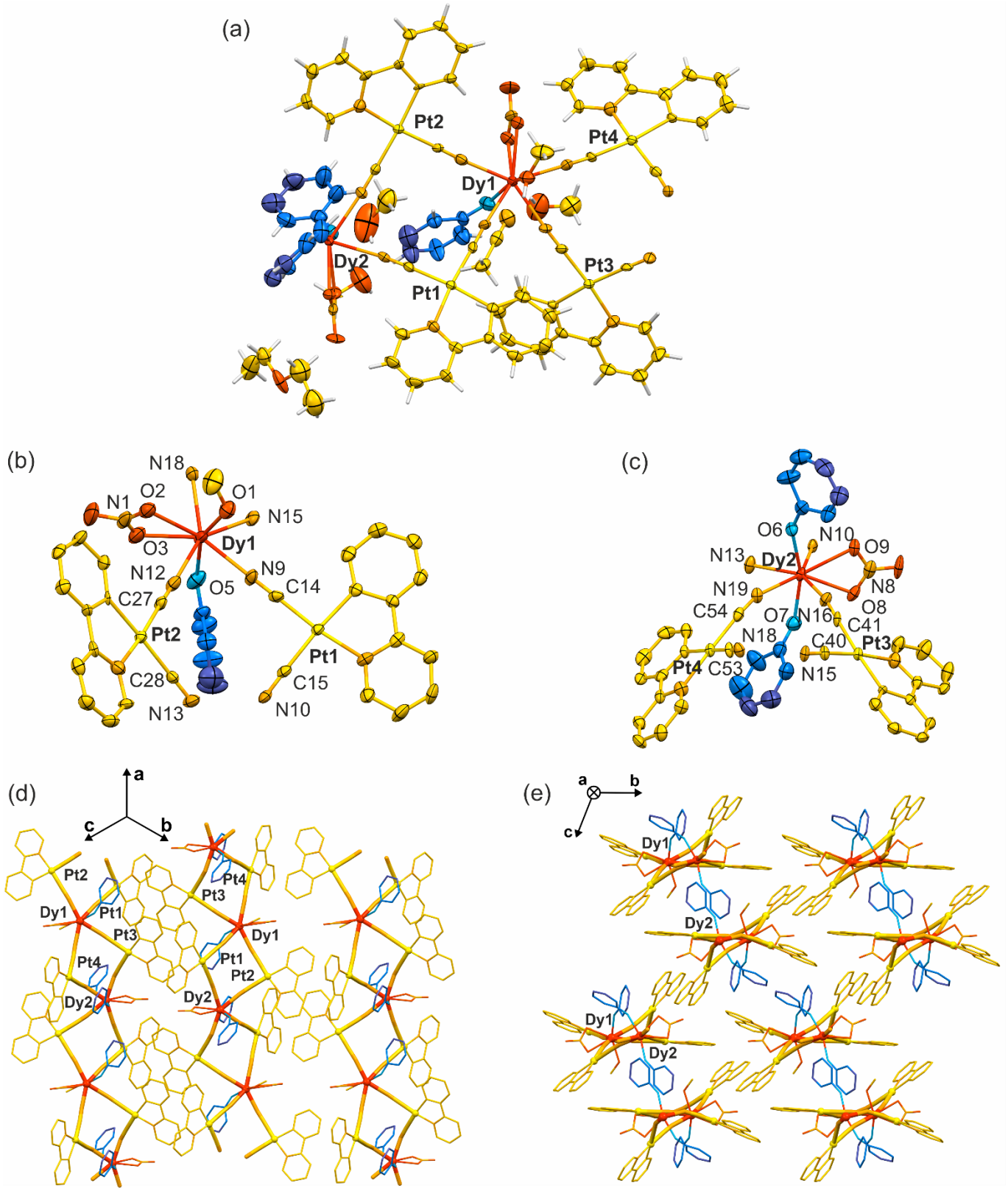

Fig. S5 Supplementary structural views of the crystal structure of **3**: (a) the asymmetric unit, (b,c) the insights into the coordination sphere of the two symmetrically independent Dy(III) complexes, presented together with the atoms labeling scheme, (d) the projection of the structure along the [111] direction, positioned perpendicular to the supramolecular layers of the $\{Dy_2Pt_4\}_n$ chains, and (e) the projection of the structure along the *a* axis, which is in parallel to the direction of the expansion of the $\{Dy_2Pt_4\}_n$ chains, showcasing their packing within the crystal. The thermal ellipsoids of non-hydrogen atoms in (a–c) are presented at the 50% probability level. For clarity, hydrogen atoms and solvent molecules are omitted in (b–e).

Table S6 Detailed structural parameters of Dy(III) complexes in **3**.

Dy1		**Dy2**	
distances			
Dy1–O1 / Å	2.330(9)	Dy2–O6 / Å	2.239(7)
Dy1–O5 / Å	2.290(9)	Dy2–O7 / Å	2.256(8)
Dy1–O2 / Å	2.496(8)	Dy2–O9 / Å	2.492(7)
Dy1–O3 / Å	2.432(9)	Dy2–O8 / Å	2.460(7)
Dy1–N18 / Å	2.415(9)	Dy2–N16 / Å	2.456(9)
Dy1–N15 / Å	2.442(9)	Dy2–N19 / Å	2.498(9)
Dy1–N9 / Å	2.404(9)	Dy2–N13 / Å	2.437(9)
Dy1–N12 / Å	2.401(10)	Dy2–N10 / Å	2.433(9)
angles			
O1–Dy1–O5 / °	155.0(3)	O6–Dy2–O7 / °	160.9(3)
O1–Dy1–N1 / °	102.2(4)	O6–Dy2–N8 / °	100.2(3)
O1–Dy1–N18 / °	82.8(3)	O6–Dy2–N16 / °	90.6(3)
O1–Dy1–N15 / °	91.8(3)	O6–Dy2–N19 / °	82.3(3)
O1–Dy1–N9 / °	76.3(3)	O6–Dy2–N13 / °	87.4(3)
O1–Dy1–N12 / °	90.6(3)	O6–Dy2–N10 / °	94.0(3)
O5–Dy1–N1 / °	99.6(4)	O7–Dy2–N8 / °	98.1(3)
O5–Dy1–N18 / °	115.7(3)	O7–Dy2–N16 / °	89.6(3)
O5–Dy1–N15 / °	79.7(3)	O7–Dy2–N19 / °	79.6(3)
O5–Dy1–N9 / °	78.8(3)	O7–Dy2–N13 / °	81.2(3)
O5–Dy1–N12 / °	84.8(3)	O7–Dy2–N10 / °	97.1(3)
O2–Dy1–N18 / °	70.3(3)	O9–Dy2–N16 / °	74.5(3)
O2–Dy1–N12 / °	70.7(3)	O9–Dy2–N10 / °	72.3(3)
O3–Dy1–N18 / °	76.4(3)	O8–Dy2–N16 / °	75.3(3)
O3–Dy1–N12 / °	78.0(3)	O8–Dy2–N10 / °	72.9(3)
N18–Dy1–N15 / °	70.9(3)	N16–Dy2–N19 / °	71.9(3)
N15–Dy1–N9 / °	73.5(3)	N19–Dy2–N13 / °	71.9(3)
N9–Dy1–N12 / °	76.1(3)	N13–Dy2–N10 / °	72.6(3)

Table S7 Results of Continuous Shape Measure (CShM) analysis for eight-coordinated Dy(III) complexes in the crystal structure of **3**.

Dy(III) center	CShM parameters*					Determined geometry
	SAPR-8	TDD-8	JBTPR-8	BTPR-8	JSD-8	
Dy1	2.716	2.384	1.984	**1.309**	3.771	BTPR-8
Dy2	4.001	**1.760**	3.008	2.720	2.409	TDD-8

*CShM parameters:

CShM SAPR-8 – the parameter related to the square antiprism geometry (D_{4d} symmetry)

CShM TDD-8 – the parameter related to the triangular dodecahedron geometry (D_{2d} symmetry)

CShM JBTPR-8 – the parameter related to the J50 biaugmented trigonal prism geometry (C_{2v} symmetry)

CShM BTPR-8 – the parameter related to the biaugmented trigonal prism geometry (C_{2v} symmetry)

CShM JSD-8 – the parameter related to the J84 snub diphenoid geometry (D_{2d} symmetry)

The value of CShM = 0 is ascribed to the ideal geometry. The increase of the CShM parameter above 0 represents the increasing distortion from the ideal polyhedron.[S8,S9]

Additional remark. We performed additional CShM calculations for the hypothetical Dy(III) coordination sphere, analogous to those found for Dy1 and Dy2 centers of **2** but replacing two O-atoms of a nitrate ion with a single O-atom placed in the center of the distance between these two O-atoms. As a result, we could treat the resulting coordination sphere as a real seven-coordinated one. Then, we checked the resulting CShM parameters corresponding to the pentagonal bipyramidal geometry; they are 2.372 and 0.674 for Dy1 and Dy2 centers, indicating that, with this approach, the coordination sphere of Dy2 is close to an ideal pentagonal bipyramidal geometry, as was suggested by the structural views (Fig. 1), while those for Dy1 is more distorted.

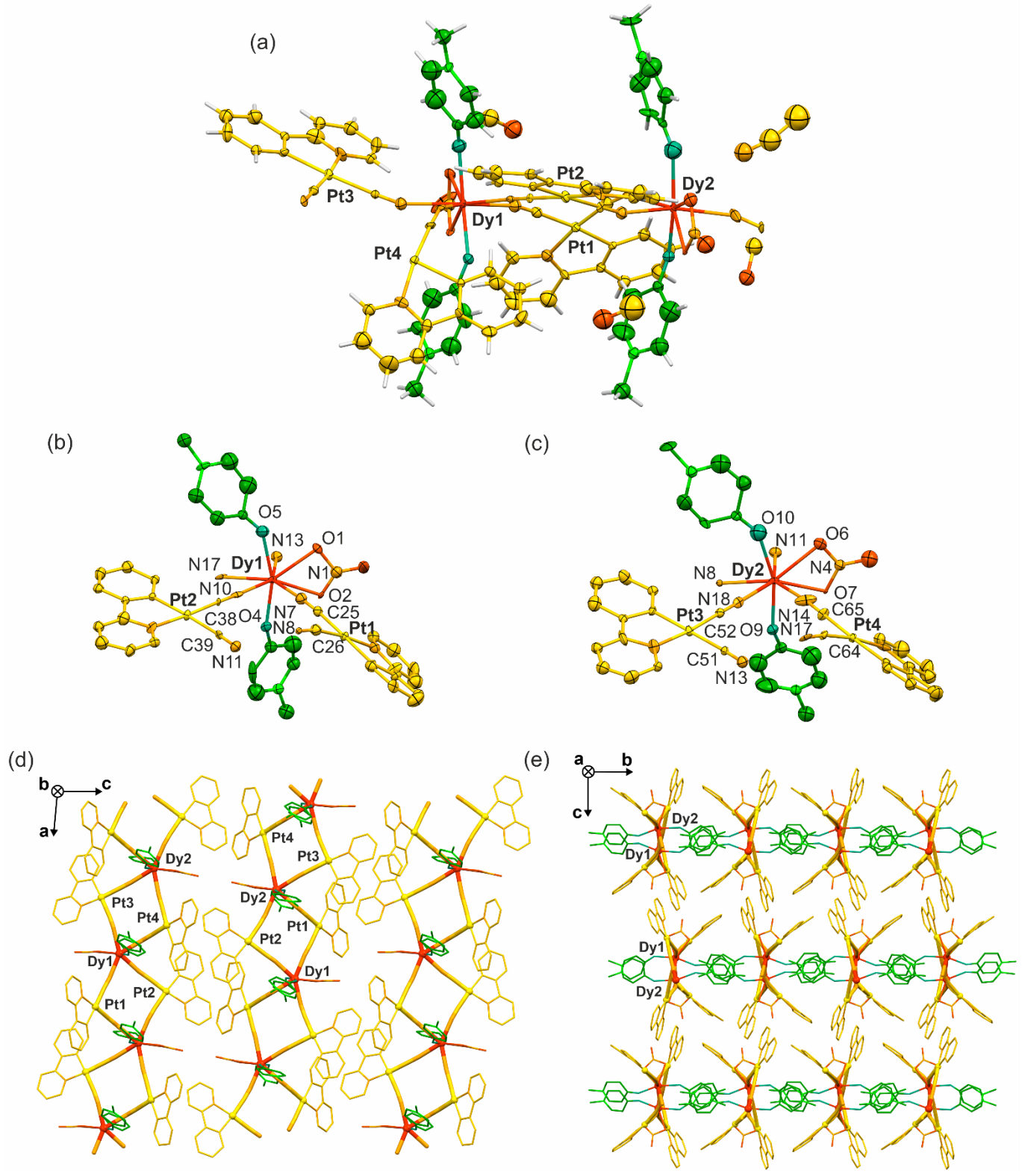

Fig. S6 Supplementary structural views of the crystal structure of **4**: (a) the asymmetric unit, (b,c) the insights into the coordination sphere of the two symmetrically independent Dy(III) complexes, presented together with the atoms labeling scheme, (d) the projection of the structure along the *b* axis, positioned perpendicular to the supramolecular layers of the $\{Dy_2Pt_4\}_n$ chains, and € the projection of the structure along the *a* axis, which is in parallel to the direction of the expansion of the $\{Dy_2Pt_4\}_n$ chains, showcasing their packing within the crystal structure. The thermal ellipsoids of non-hydrogen atoms in (a–c) are presented at the 50% probability level. For clarity, hydrogen atoms and solvent molecules are omitted in (b–e).

Table S8 Detailed structural parameters of Dy(III) complexes in **4**.

Dy1		**Dy2**	
distances			
Dy1–O4 / Å	2.23(3)	Dy2–O9 / Å	2.24(2)
Dy1–O5 / Å	2.33(3)	Dy2–O10 / Å	2.36(4)
Dy1–O2 / Å	2.43(2)	Dy2–O7 / Å	2.392(18)
Dy1–O1 / Å	2.44(2)	Dy2–O6 / Å	2.51(3)
Dy1–N13 / Å	2.47(3)	Dy2–N14 / Å	2.46(3)
Dy1–N17 / Å	2.46(3)	Dy2–N18 / Å	2.46(3)
Dy1–N10 / Å	2.47(3)	Dy2–N8 / Å	2.49(2)
Dy1–N7 / Å	2.42(3)	Dy2–N11 / Å	2.43(3)
angles			
O4–Dy1–O5 / °	161.8(9)	O9–Dy2–O10 / °	161.9(11)
O4–Dy1–N1 / °	100.1(9)	O9–Dy2–N4 / °	100.6(9)
O4–Dy1–N13 / °	96.3(10)	O9–Dy2–N14 / °	89.5(10)
O4–Dy1–N17 / °	79.2(9)	O9–Dy2–N18 / °	84.2(9)
O4–Dy1–N10 / °	83.9(9)	O9–Dy2–N8 / °	78.0(8)
O4–Dy1–N7 / °	89.0(10)	O9–Dy2–N11 / °	97.4(10)
O5–Dy1–N1 / °	97.9(10)	O10–Dy2–N4 / °	97.5(10)
O5–Dy1–N13 / °	86.7(10)	O10–Dy2–N14 / °	96.8(12)
O5–Dy1–N17 / °	84.6(9)	O10–Dy2–N18 / °	81.9(11)
O5–Dy1–N10 / °	83.4(9)	O10–Dy2–N8 / °	86.6(10)
O5–Dy1–N7 / °	99.3(10)	O10–Dy2–N11 / °	87.2(11)
O2–Dy1–N13 / °	73.9(9)	O7–Dy2–N14 / °	73.0(10)
O2–Dy1–N7 / °	72.8(9)	O7–Dy2–N11 / °	76.2(9)
O1–Dy1–N13 / °	73.5(9)	O6–Dy2–N14 / °	74.3(11)
O1–Dy1–N7 / °	75.4(9)	O6–Dy2–N11 / °	74.7(9)
N13–Dy1–N17 / °	73.2(10)	N14–Dy2–N18 / °	71.1(12)
N17–Dy1–N10 / °	72.1(9)	N18–Dy2–N8 / °	71.4(8)
N10–Dy1–N7 / °	71.9(10)	N8–Dy2–N11 / °	73.3(9)

Table S9 Results of Continuous Shape Measure (CShM) analysis for eight-coordinated Dy(III) complexes in the crystal structure of **4**.

Dy(III) center	CShM parameters*					Determined geometry
	SAPR-8	TDD-8	JBTPR-8	BTPR-8	JSD-8	
Dy1	2.993	**1.651**	2.849	2.397	2.594	TDD-8
Dy2	3.083	**1.767**	3.062	2.581	2.664	TDD-8

*CShM parameters:

CShM SAPR-8 – the parameter related to the square antiprism geometry (D_{4d} symmetry)

CShM TDD-8 – the parameter related to the triangular dodecahedron geometry (D_{2d} symmetry)

CShM JBTPR-8 – the parameter related to the J50 biaugmented trigonal prism geometry (C_{2v} symmetry)

CShM BTPR-8 – the parameter related to the biaugmented trigonal prism geometry (C_{2v} symmetry)

CShM JSD-8 – the parameter related to the J84 snub diphenoid geometry (D_{2d} symmetry)

The value of CShM = 0 is ascribed to the ideal geometry. The increase of the CShM parameter above 0 represents the increasing distortion from the ideal polyhedron.[S8,S9]

Additional remark. We performed additional CShM calculations for the hypothetical Dy(III) coordination sphere, analogous to those found for Dy1 and Dy2 centers of **1** but replacing two O-atoms of a nitrate ion with a single O-atom placed in the center of the distance between these two O-atoms. As a result, we could treat the resulting coordination sphere as a real seven-coordinated one. Then, we checked the resulting CShM parameters corresponding to the pentagonal bipyramidal geometry; they are 0.805 and 0.765 for Dy1 and Dy2 centers, indicating that, with this approach, the coordination spheres are close to an ideal pentagonal bipyramidal geometry, as was suggested by the structural views (Fig. 1).

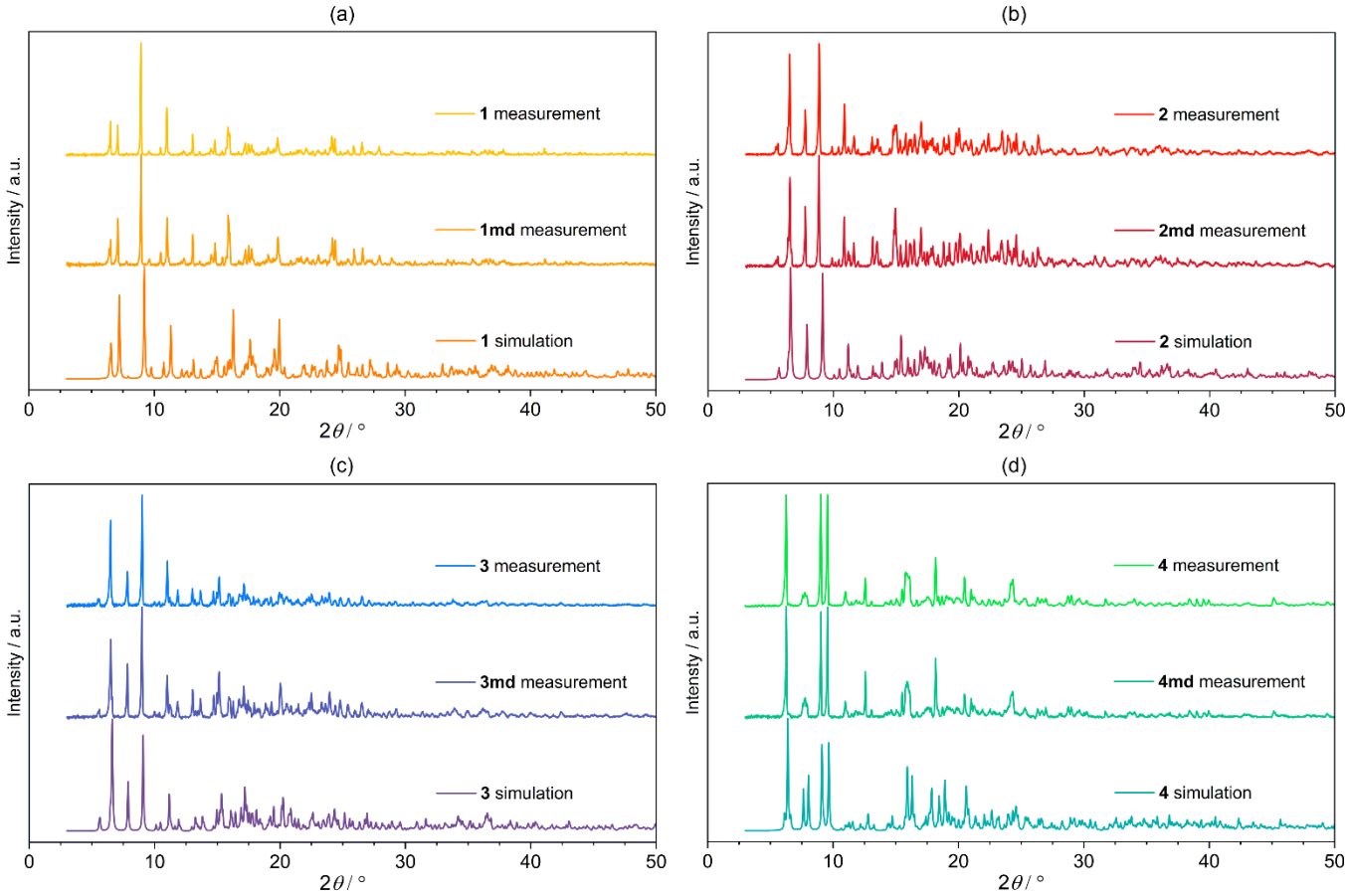

Fig. S7 Experimental (labeled as **measurement**) powder X-ray diffraction (P-XRD) patterns for (a) **1** and **1md**, (b) **2** and **2md** (c) **3** and **3md**, and (d) **4** and **4md**, compared with the calculated (labeled as **simulation**) diffraction patterns based on the single-crystal X-ray diffraction (SC-XRD) data of **1**–**4**.

Comment to Fig. S8–S17 and Table S10 – basic optical properties

The UV-vis-NIR absorption spectra are almost identical for all of the compounds **1–4** (see Fig. S8 below). Their significant absorption bands lie mostly in the UV region, which manifests as a pale–yellow color of the crystals. The set of weak sharp peaks near 475 nm corresponds to the first local maximums of the excitation spectra (see Fig. S13–S17). In Table S10, all the data about the emission lifetimes and quantum yields were gathered. For **1**–**4**, emission lifetimes are almost the same for all of the observed emission peaks. However, they change greatly with the temperature, from ca. 1 μs at room temperature to ca. 20 μs at the temperature of liquid nitrogen. The emission quantum yields at room temperature (Fig. S14) are rather moderate, ranging from just over 3% for compound **3** to ca. 10% for compounds **1** and **4**.

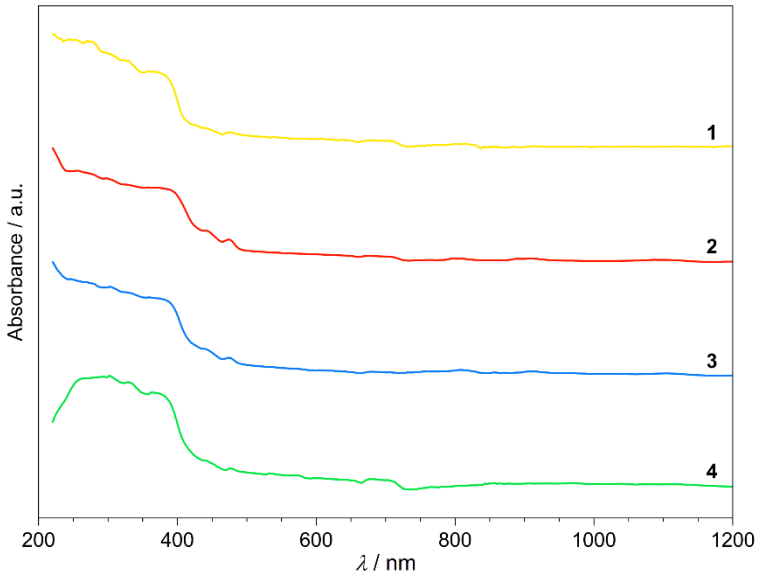

Fig. S8 Room-temperature solid-state UV-vis-NIR absorption spectra of compounds **1**–**4**, collected in the 220–1200 nm range.

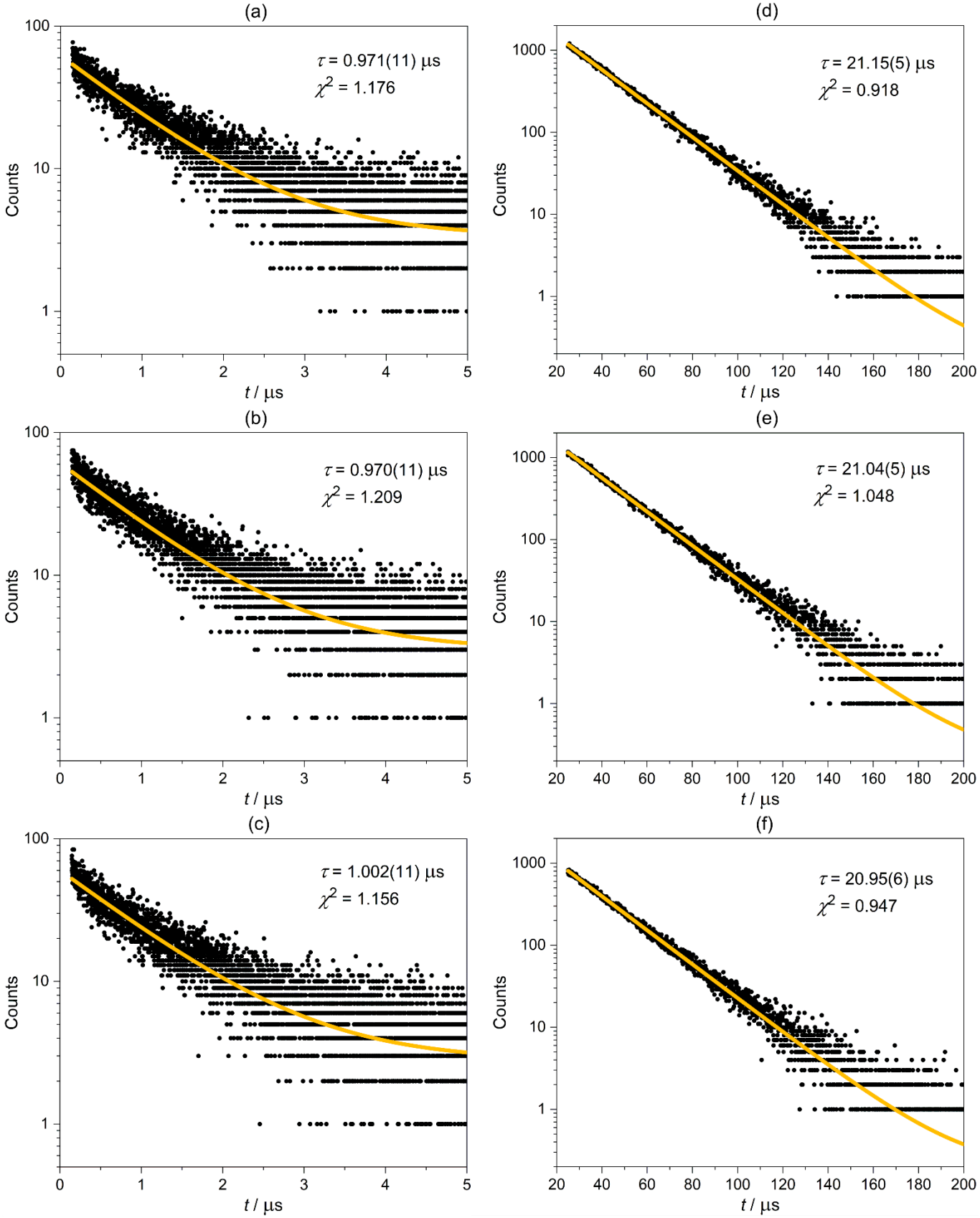

Fig. S9 Emission decay profiles for **1** under the 374 nm diode laser excitation, collected at room temperature (left part, a–c) and at 77 K (right part, d–f) with the emission slit fixed at 484 nm (a), 515 nm (b), 550 nm (c), and at 476 nm (d), 510 nm (e), 545 nm (f), for the high and low temperature, respectively.

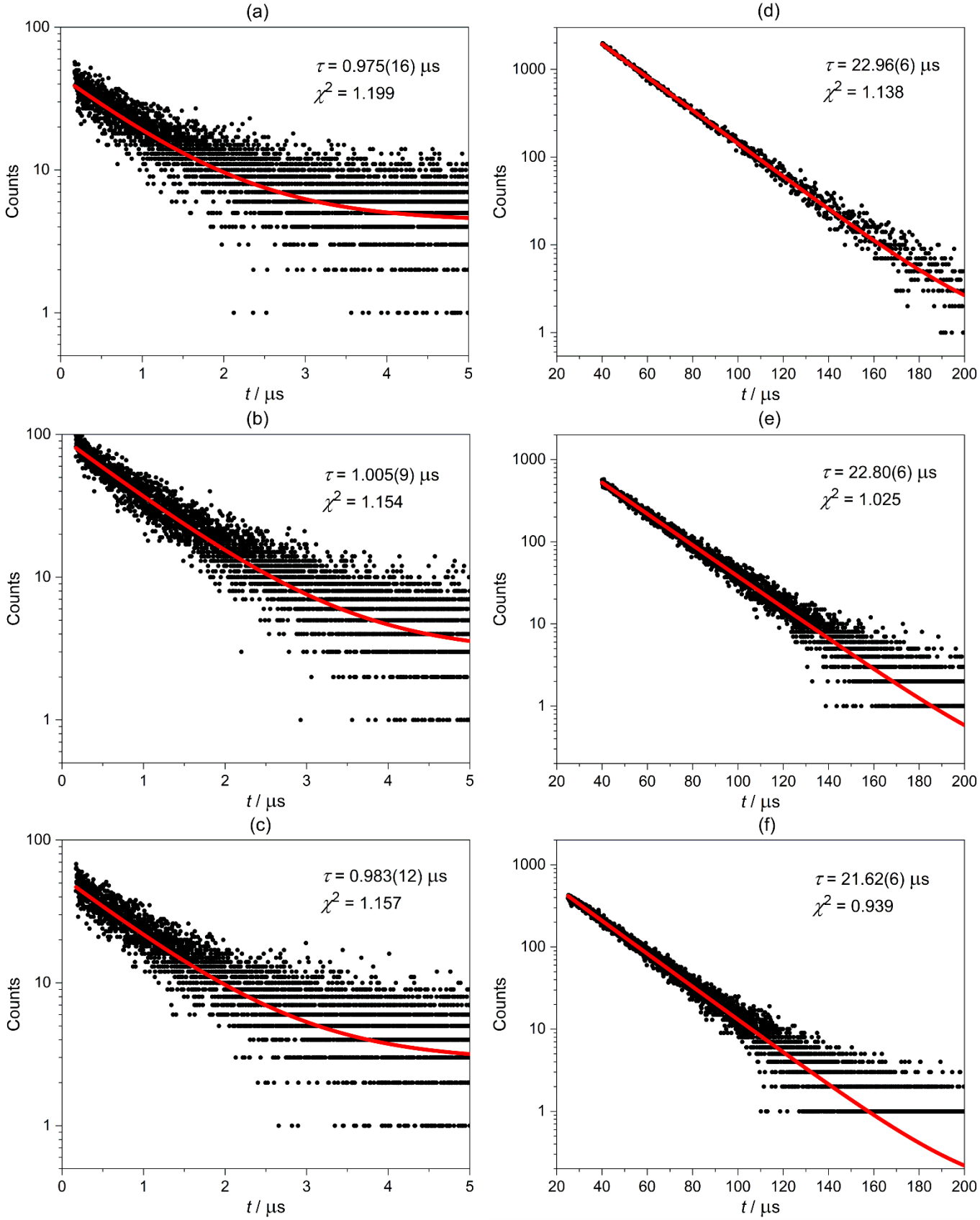

Fig. S10 Emission decay profiles for **2** under the 374 nm diode laser excitation, collected at room temperature (left part, a–c) and at 77 K (right part, d–f) with the emission slit fixed at 484 nm (a), 515 nm (b), 550 nm (c), and at 472 nm (d), 508 nm (e), 540 nm (f), for the high and low temperature, respectively.

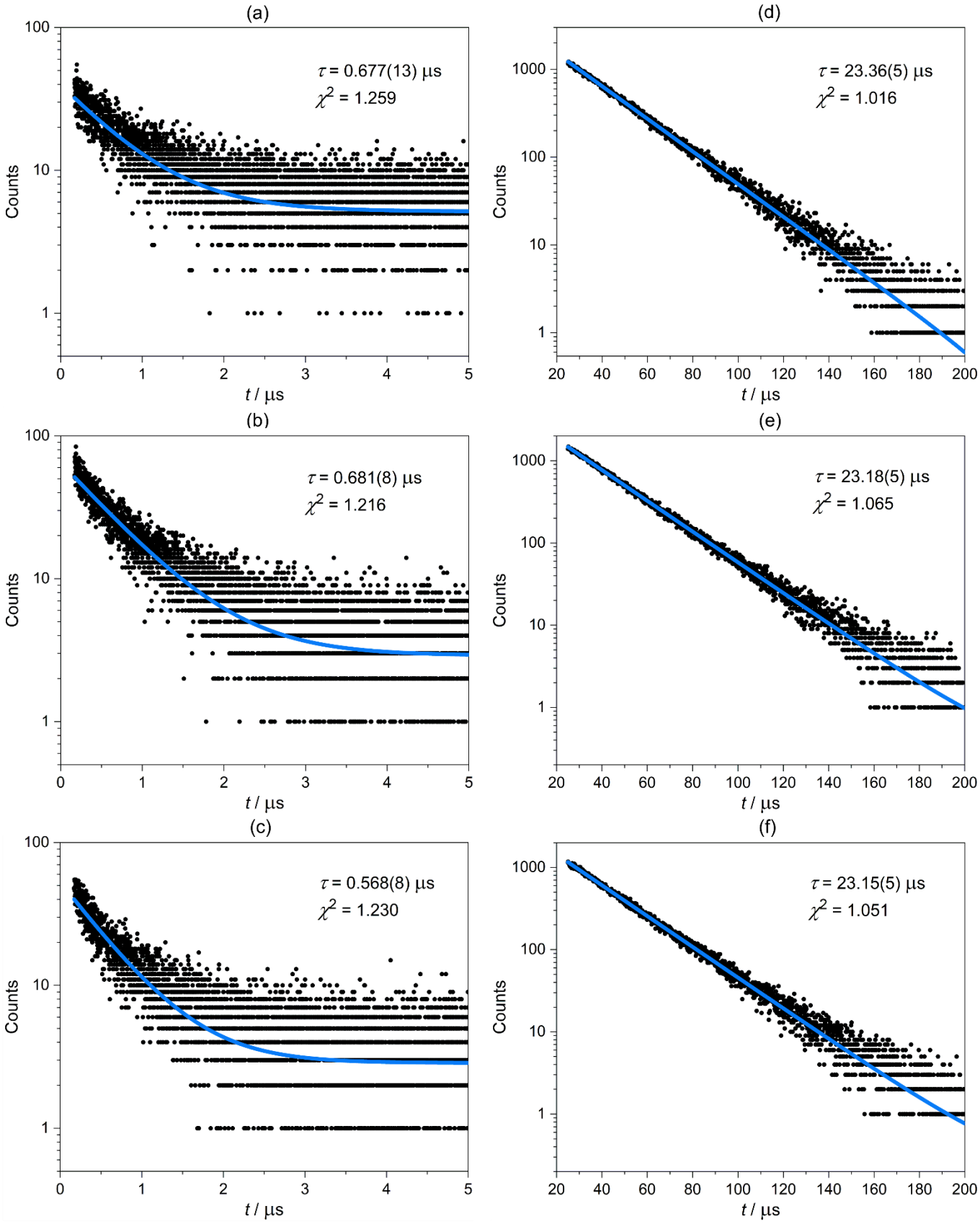

Fig. S11 Emission decay profiles for **3** under the 374 nm diode laser excitation, collected at room temperature (left part, a–c) and at 77 K (right part, d–f) with the emission slit fixed at 484 nm (a), 515 nm (b), 550 nm (c), and at 475 nm (d), 510 nm (e), 540 nm (f), for the high and low temperature, respectively.

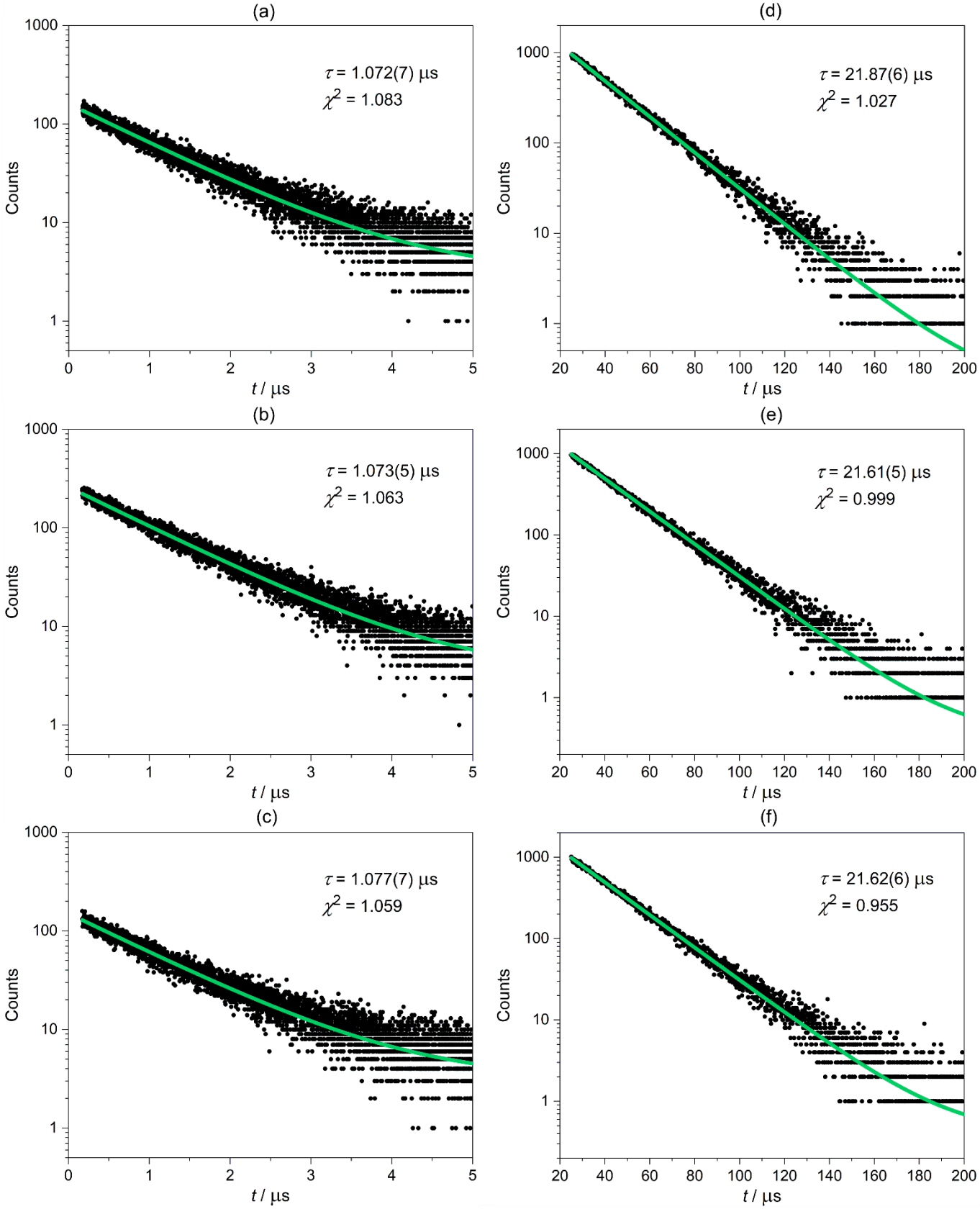

Fig. S12 Emission decay profiles for **4** under the 374 nm diode laser excitation, collected at room temperature (left part, a–c) and at 77 K (right part, d–f) with the emission slit fixed at 484 nm (a), 515 nm (b), 550 nm (c), and at 475 nm (d), 510 nm (e), 540 nm (f), for the high and low temperature, respectively.

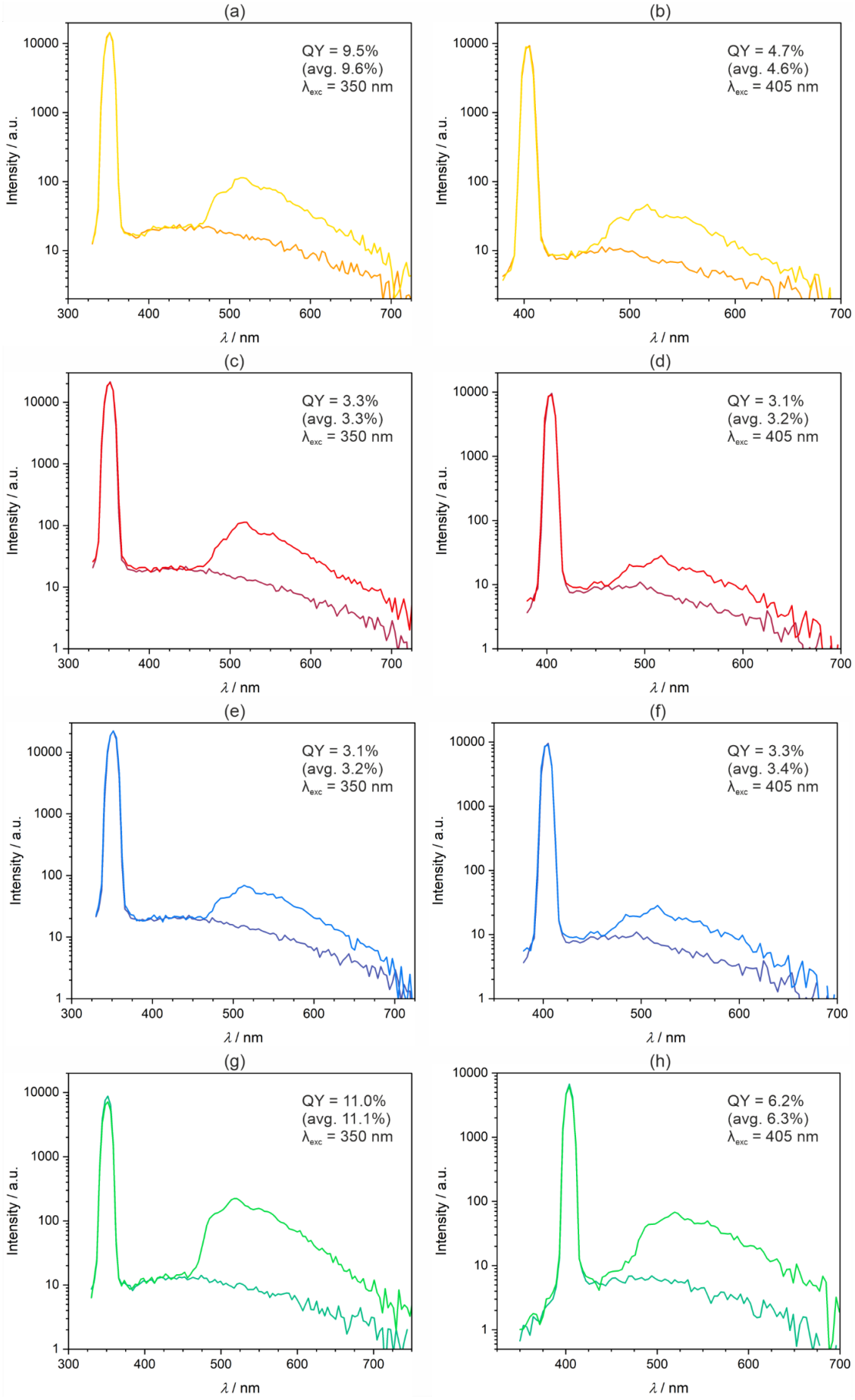

Fig. S13 Representative emission spectra of the powder samples of **1** (a and b), **2** (c and d), **3** (e and f), and **4** (g and h), which were employed for the absolute emission quantum yield determination. The employed excitation wavelengths and the obtained quantum yield (Φ, QY) values are indicated in the figure. The indicated QY value corresponds to the presented spectrum (a single representative measurement) while the average QY values from a series of repeated measurements are given in the brackets (avg.). The background signal is given in a darker color in each figure.

Table S10 The summary of the emission lifetimes for **1**–**4** under the 374 nm diode laser excitation for the indicated emission maxima, presented together with the room-temperature emission quantum yields obtained using the 350 nm and 405 nm Xe lamp excitation.

compound	**1**		**2**		**3**		**4**	
emission lifetimes, τ								
temperature	λ_{em} / nm	τ / μs	λ_{em} / nm	τ / μs	λ_{em} / nm	τ / μs	λ_{em} / nm	τ / μs
298 K	484	0.971(11)	484	0.975(16)	484	0.677(13)	484	1.072(7)
	515	0.970(11)	515	1.005(9)	515	0.681(8)	515	1.073(5)
	550	1.002(11)	550	0.983(12)	550	0.568(8)	550	1.077(7)
77 K	476	21.15(5)	472	22.96(5)	475	23.36(5)	475	21.87(6)
	510	21.04(5)	508	22.80(6)	510	23.18(5)	510	21.61(5)
	545	20.95(6)	540	21.62(6)	540	23.15(5)	540	21.62(5)
absolute emission quantum yield, Φ (QY)								
λ / nm	350	405	350	405	350	405	350	405
Φ / %	9.6(7)	4.6(5)	4.7(6)	3.8(8)	3.2(3)	3.4(2)	11.0(2)	6.3(4)

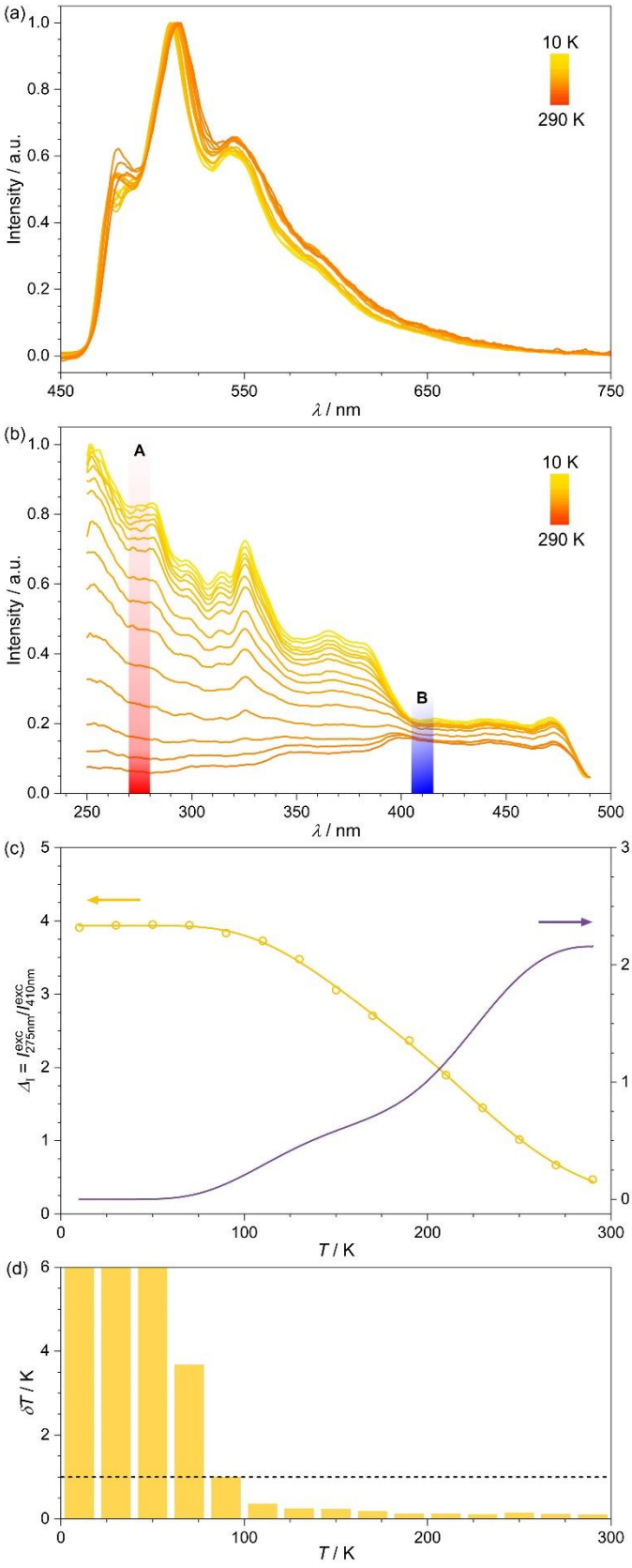

Fig. S14 Temperature-variable photoluminescence characteristics of **1**, collected in the 10–290 K range: the emission spectra under the 320 nm excitation (a), the excitation spectra followed at λ_{em} = 510 nm (b), the temperature dependence of the thermometric parameter, Δ_I, defined as the ratio between the integrated areas of excitation centered at 275 nm (A) and 410 nm (B), accompanied by its relative thermal sensitivity (c), and its temperature uncertainty at the selected temperature values (d). Red (A) and blue (B) areas in (b) indicate wavelengths used for the definition of the thermometric parameter, whereas the dashed line in (d) marks the δT threshold of 1 K. The related parameters of the fitted curve, obtained using the Mott-Seitz model, are gathered in Table S11. The intensity values in (a) and (b) are normalized for clarity.

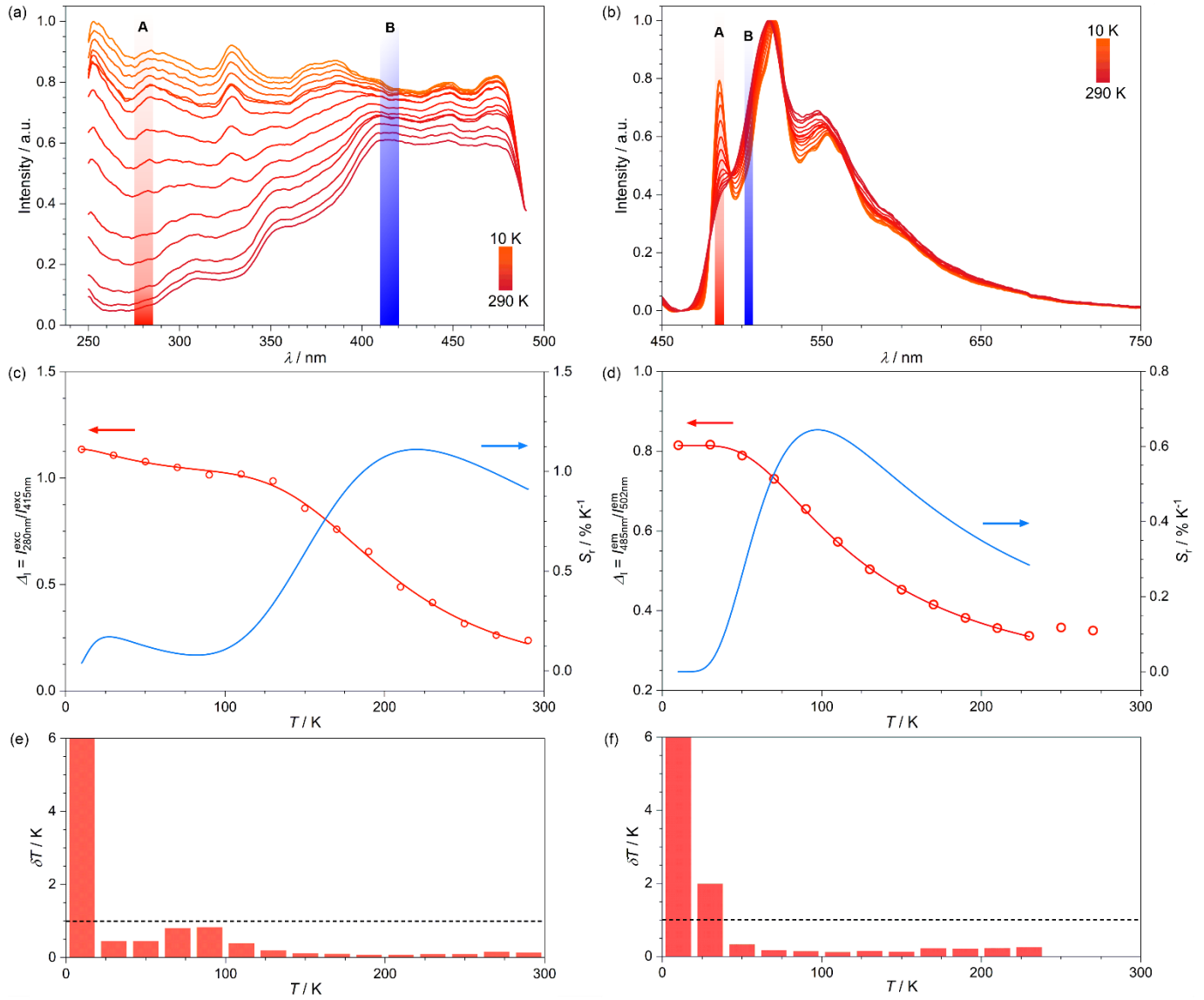

Fig. S15 Temperature-variable photoluminescence characteristics of **2**, collected in the 10–290 K range: excitation spectra followed at λ_{em} = 515 nm (a), the emission spectra under the 410 nm excitation (b), the temperature dependence of the thermometric parameter, Δ_I, defined as the ratio between the integrated areas of excitation centered at 280 nm (A) and 415 nm (B), accompanied by its relative thermal sensitivity (c), the temperature dependence of the thermometric parameter, Δ_I, defined as the ratio between the integrated areas of emission intensity centered at 485 nm (A) and 502 nm (B), accompanied by its relative thermal sensitivity (d), together with the respective temperature uncertainties at the selected temperature values, (e) and (f). In (a) and (b) the blue areas marked with B represent ranges used as denominators in the definition of Δ_I parameters, while the red areas marked with A correspond to the ranges of which the integrated areas were used as numerators in such a definition. The dashed lines in (e) and (f) mark the δT threshold of 1 K. The related parameters of the fitted curves in (c) and (d), obtained using the Mott-Seitz model, are gathered in Table S11. The intensity values in (a) and (b) are normalized for clarity.

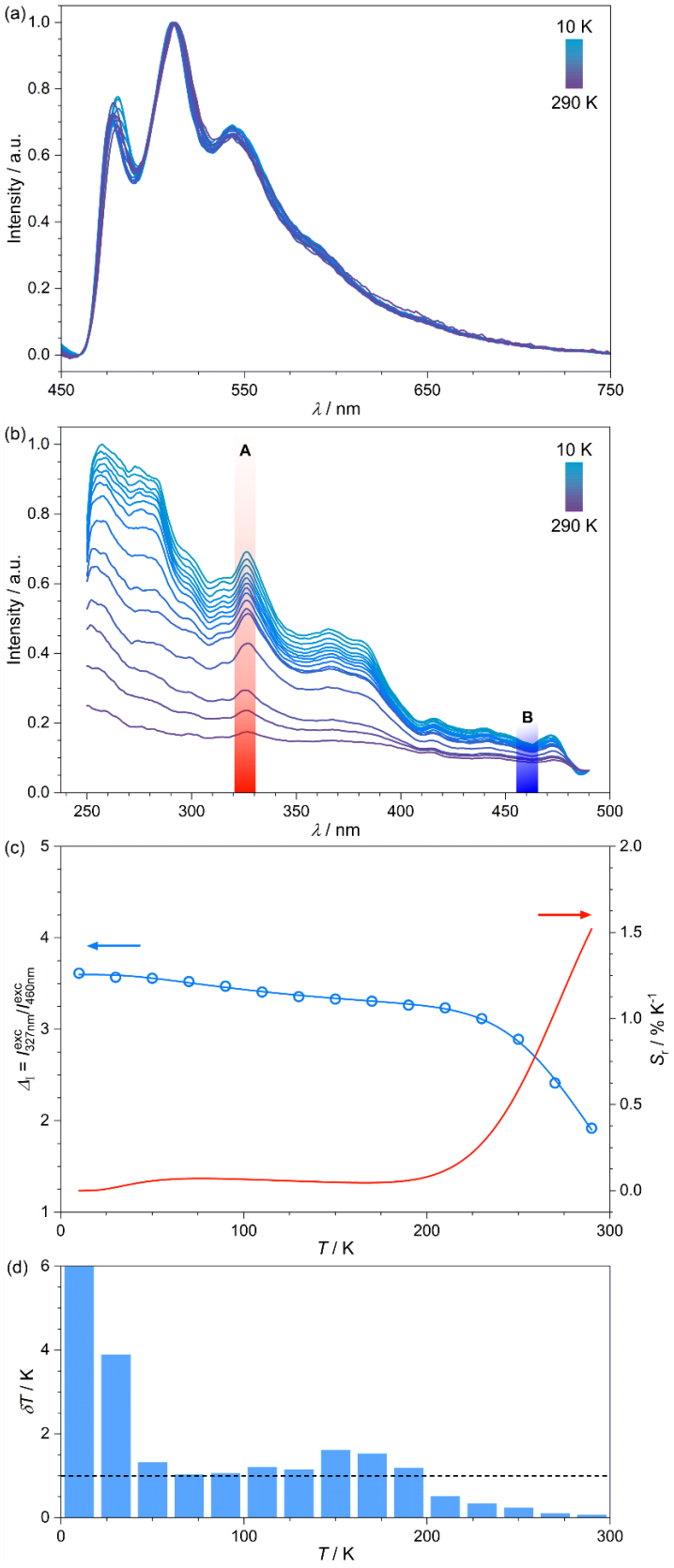

Fig. S16 Temperature-variable photoluminescence characteristics of **3**, collected in the 10–290 K range: the emission spectra under the 320 nm excitation (a), the excitation spectra followed at λ_{em} = 515 nm (b), the temperature dependence of the thermometric parameter, Δ_I, defined as the ratio between the integrated areas of excitation centered at 327 nm (A) and 460 nm (B), accompanied by its relative thermal sensitivity (c), and its temperature uncertainty at the selected temperature values (d). Red (A) and blue (B) areas in (b) indicate wavelengths used for the definition of the thermometric parameter, whereas the dashed line in (d) marks the δT threshold of 1 K. The related parameters of the fitted curve, obtained using the Mott-Seitz model, are gathered in Table S11. The intensity values in (a) and (b) are normalized for clarity.

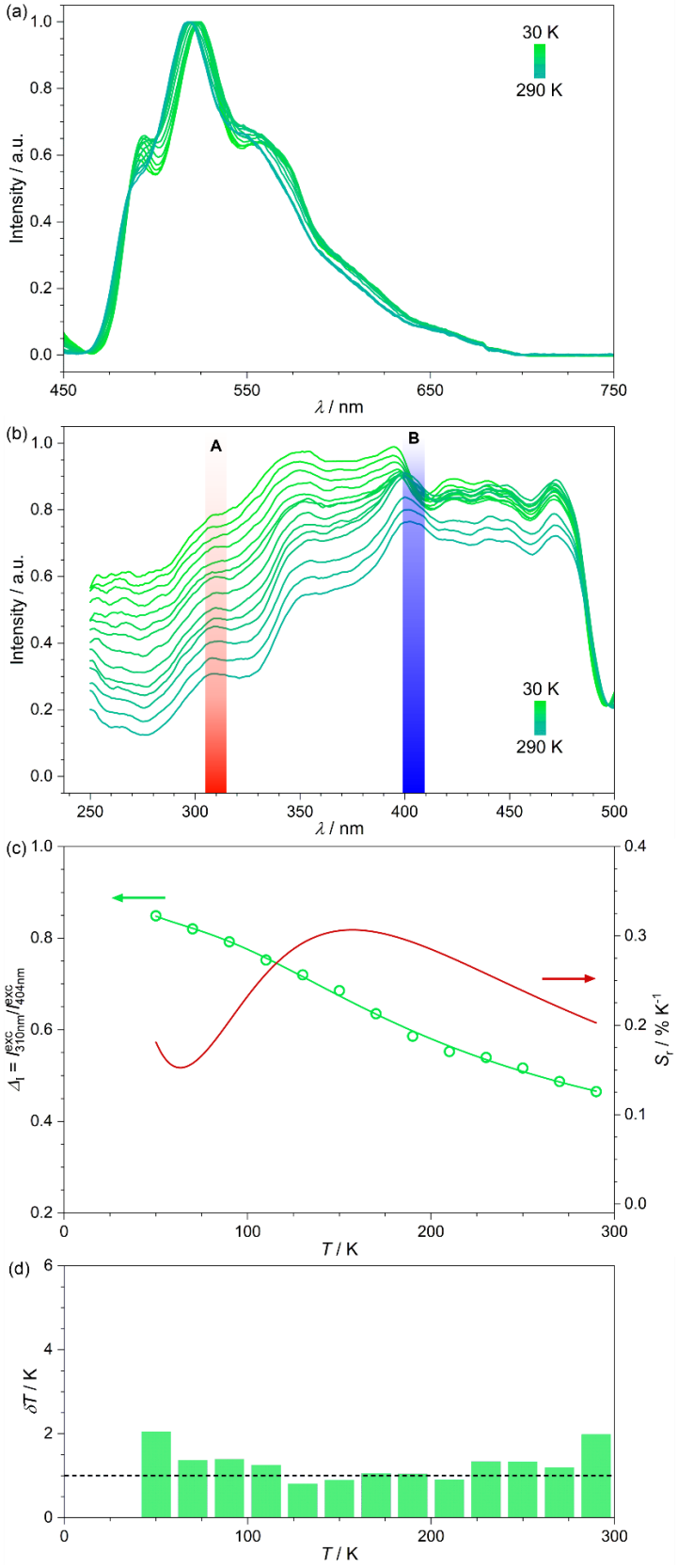

Fig. S17 Temperature-variable photoluminescence characteristics of **4**, collected in the 30–290 K range: the emission spectra under the 365 nm excitation (a), the excitation spectra followed at λ_{em} = 500 nm (b), the temperature dependence of the thermometric parameter, Δ_I, defined as the ratio between the integrated areas of excitation centered at 310 nm (A) and 404 nm (B), accompanied by its relative thermal sensitivity (c), and its temperature uncertainty at the selected temperature values (d). Red and blue areas in (b) indicate wavelengths used for the definition of the thermometric parameter, whereas the dashed line in (d) marks the δT threshold of 1 K. The related parameters of the fitted curve, obtained using the Mott-Seitz model, are gathered in Table S11. The intensity values in (a) and (b) are normalized for clarity.

Comment to Fig. S14–S17 and Table S11 – temperature-variable luminescence studies

Before analyzing the temperature-variable luminescence data, both the emission and excitation spectra were smoothed with the Savitzky-Golay filter (2nd order polynomial with 11 points in a window). The uncertainty of the resulting signal intensity values was calculated as the standard deviation of the difference between the original data and the smoothed dataset in the window of 11 points.

From the smoothed data, the backgrounds were removed. In the case of emission spectra, it was observed that the sample's emission starts around 465 nm and a Gaussian background was modeled with the maxima at 460 nm (with the values of the signal at that point for each temperature) and plateau-matching with the flattening of the emission over 660 nm. With excitation spectra, a simpler approach was employed. It was assumed that the values at the minimum at 495 nm do not change with temperature, so all of the curves were shifted so that the values at that point would be identical to those at 290 K. The resulting spectra are presented in Fig. S14–S17.

Initially, the thermometric parameters, Δ, were defined as the ratio between the intensities at two wavelengths at a certain temperature (A and B). Then, its uncertainty, $\delta\Delta$, was extracted from the uncertainties of intensities, δA and δB, following the equation S1:

$$\delta\Delta = \sqrt{\delta A^2 \frac{1}{B^2} + \delta B^2 \frac{A^2}{B^4}} \qquad \text{eq. S1}$$

Such simplified thermometric parameters were used to determine the optimal wavelengths for ratiometric thermometry. First, based on the apparent signal-to-noise ratios, suitable ranges were chosen, i.e., 275–475 nm for excitation and 475–600 nm for emission spectra. Then, for each pair of wavelengths, the ratio of Δ at the lowest temperature to Δ at the highest temperature was calculated. For the pair with the largest change in the thermometric parameter, the integrated intensities (I_A and I_B) were calculated, as a sum of all of the intensities of points less than 5 nm from one at the optimal wavelength (eq. S2). Their uncertainties (δI_A and δI_B) were estimated as square roots of sums of squares of uncertainties at each point (eq. S3).

$$I_A = \sum_{i=-5\ nm}^{5\ nm} A_i \qquad I_B = \sum_{i=-5\ nm}^{5\ nm} B_i \qquad \text{eq. S2}$$

$$\delta I_A = \sqrt{\sum_{i=-5\ nm}^{5\ nm} \delta A_i{}^2} \qquad \delta I_B = \sqrt{\sum_{i=-5\ nm}^{5\ nm} \delta B_i{}^2} \qquad \text{eq. S3}$$

The set of final thermometric parameters, Δ_I, was therefore defined as the ratio between integrated intensities centered at the two wavelengths at a certain temperature (A and B). The related uncertainty, $\delta\Delta_I$, was extracted based on the uncertainties of intensities using δI_A and δI_B, following the equation S4:

$$\delta\Delta_I = \sqrt{\delta I_A{}^2 \frac{1}{I_B{}^2} + \delta I_B{}^2 \frac{I_A{}^2}{I_B{}^4}} \qquad \text{eq. S4}$$

The temperature dependence of Δ_I was fitted employing the Mott–Seitz model, [S10] with one (for **2**, eq. S5) or two (for **1**, **3**, and **4**, eq. S6) exponential components:

$$\Delta_I(T) = \frac{\Delta_0}{1+\alpha_1 e^{-\Delta E_1/T}} \qquad \text{eq. S5}$$

$$\Delta_I(T) = \frac{\Delta_0}{1+\alpha_1 e^{-\Delta E_1/T}+\alpha_2 e^{-\Delta E_2/T}} \qquad \text{eq. S6}$$

where Δ_0, α_i, and ΔE_i are parameters, whose values are collected in Table S11, and T stands for the temperature in K. The relative thermal sensitivity, S_r,[S10] was determined based on the fitted curve, following the equation S7:

$$S_r = \frac{1}{\Delta_I}\left|\frac{\partial\Delta_I}{\partial T}\right| \qquad \text{eq. S7}$$

Then, the uncertainty of temperature measurement, δT, [S10] was estimated with the equation S8:

$$\delta T = \frac{1}{S_r}\frac{\delta\Delta_I}{\Delta_I} \qquad \text{eq. S8}$$

The excitation spectra of all of the compounds **1**–**4** showed significant temperature dependence, with S_r exciding 1% K^{-1} for **1** and **2** at 200 K and 185 K and above respectively (Fig. S14 and S15). The best excitation sensitivity for **3** and **4** lies in a similar region, between 150 K and 300 K (Fig. 4 and 5). The thermometric response of the emission spectra was much weaker, and the parameters were only calculated for compound **2**. The highest sensitivity of them lies in the lower temperature region than for the excitation, with the maximum between 100 and 200 K.

Table S11 Summary of the extracted parameters from the fitting of the temperature dependences of the thermometric parameters using the Mott–Seitz model for excitation and emission spectra of **1**–**4**.

parameter	**1**		**2**		**3**		**4**	
	excitation	emission	excitation	emission	excitation	emission	excitation	emission
Δ_0	4.10(2)	—	1.06(2)	1.543(5)	3.60(1)	—	1.07(2)	—
α_1	$2.6(2)\cdot10^{3}$	—	$1.25(8)\cdot10^{3}$	$2.68(4)\cdot10^{2}$	$2.1(2)\cdot10^{-1}$	—	$5.9(7)\cdot10^{2}$	—
ΔE_1 / K	$6(4)\cdot10^{5}$	—	$6(2)\cdot10^{2}$	4.01(9)	$1.5(2)\cdot10^{2}$	—	8(1)	—
α_2	$5.5(4)\cdot10^{2}$	—	—	—	$32(16)\cdot10^{3}$	—	$1.0(5)\cdot10^{2}$	—
ΔE_2 / K	$1.1(2)\cdot10^{1}$	—	—	—	$3.1(1)\cdot10^{3}$	—	$4(2)\cdot10^{-1}$	—

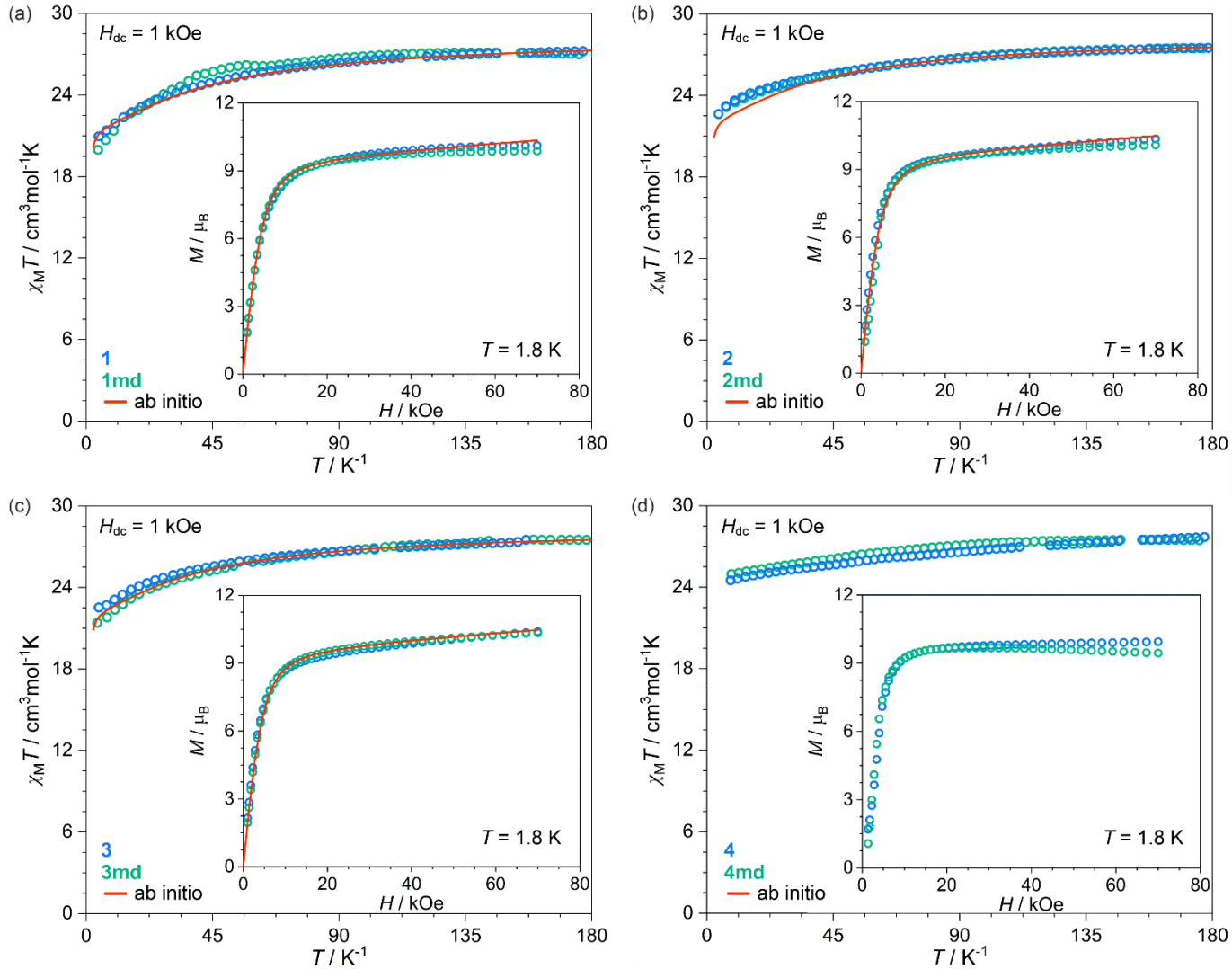

Fig. S18 Direct-current (*dc*) magnetic characteristics, including the temperature dependences of the $\chi_M T$ product under the external magnetic field of H_{dc} = 1 kOe, and the field dependences of molar magnetization, M, collected at T = 1.8 K (the insets), for **1** and **1md** (a), **2** and **2md** (b), **3** and **3md** (c), and **4** and **4md** (d). Colored points represent the experimental $\chi_M T(T)$ and $M(H)$ curves for **1**–**4** and **1md**–**4md**, while the solid red lines are the results of the theoretical analysis obtained using the *ab initio* calculations (red solid lines). To facilitate the comparison, the respective results for magnetically diluted samples are calculated for the molar number of paramagnetic metal centers.

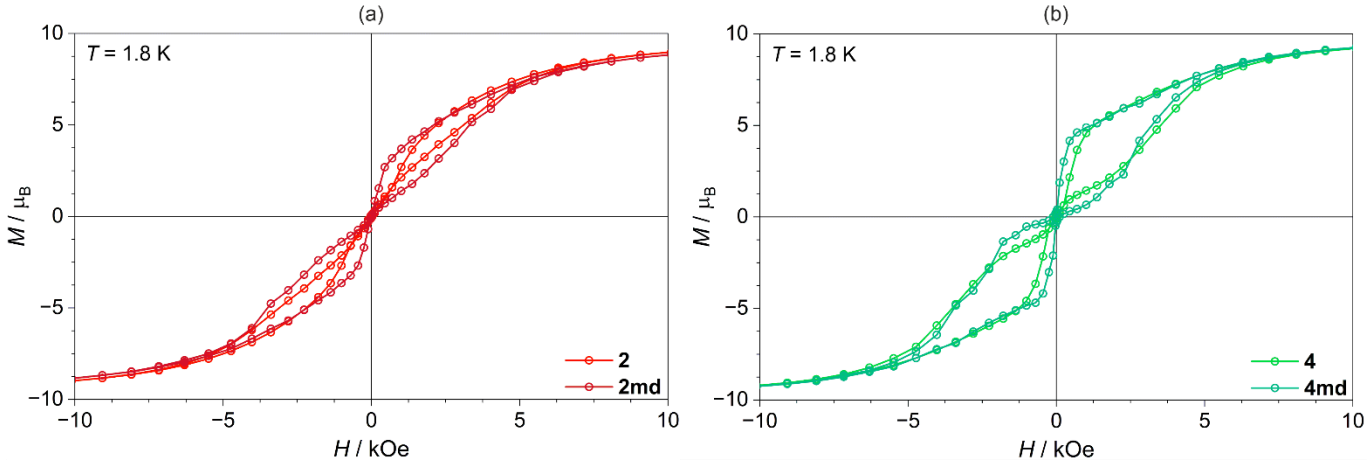

Fig. S19 Magnetization versus applied field hysteresis loops at 1.8 K for **2** and **2md** (a) as well as **4** and **4md** (b). To facilitate the comparison, the respective results for magnetically diluted samples are calculated for the molar number of paramagnetic metal centers.

Comment to Fig. S18 and S20–S22 as well as Tables S12–S15 – *ab initio* calculations

The *ab initio* calculations were performed using the crystal structures taken directly from the single-crystal X-ray diffraction experiments without any further optimization of the molecular geometry. Due to the insufficient quality of structural data, compound **4** was excluded from the main analysis (the rough results of the *ab initio* calculations, which were performed analogously to the other compounds as described below, are shown as the addition to the ESI, see Table S20, Fig. S48, and the related comment).

For each symmetrically independent Dy(III) center, the two molecular fragments were used for simulations. The smaller one (**S**) consisted only of the Dy(III) center with coordinated organic and cyanido ligands together with NO_3^- counterions. The bigger one (**B**) consisted of the Dy(III) center, coordinated organic ligands, the whole dicyanido(2-phenylpyridinato)platinate(II) metalloligands, and NO_3^- counterions. The respective calculated clusters were visualized in Fig. S20–S22. To examine local magnetic properties of the Dy(III) centers, State Average Complete Active Space Self-Consistent Field (SA-CASSCF) calculations were performed using the OpenMolcas quantum chemistry software package.[S11] Scalar relativistic effects were taken into account by employing two-component second-order Douglas-Kroll-Hess (DKH2) Hamiltonian together with relativistic Atomic Natural Orbital basis sets of the ANO-RCC type (Table S12).[S12–S14] To save the disk space for computations, the Cholesky decomposition of ERI-s (electron repulsion integrals) was used with the $1.0 \cdot 10^{-8}$ threshold.

In the CASSCF step, the active space was composed of seven 4f-orbitals of the Dy(III) centers with 9 active electrons – CAS(9in7), then 21 sextets, 224 quartets, and 490 doublet spin-adapted states arising from different possible electrons distributions in 4f orbitals were evaluated. In the next step, all sextets, 128 quartets, and 130 doublets previously optimized as spin-free states were mixed within the Restricted Active Space State Interaction (RASSI) submodule by Spin-Orbit-Coupling (SOC) within the atomic mean-field (AMFI) approximation.[S15,S16] In the final step, the resulting 898 spin-orbit states were analyzed using the SINGLE_ANISO module to obtain main magnetic axes and the pseudo-*g*-tensors of each Kramers doublet, decompose SO states of the ground Dy(III) $^6H_{15/2}$ multiplet into ones with a definite projection of the total momentum on the located quantization *z*-axis of the ground doublet and simulate crystal field parameters used for the magnetic data analysis.[S17,S18] The energy splitting of the ground $^6H_{15/2}$ multiplet of the Dy(III) centers with pseudo-*g*-tensor components and the composition of the ground doublet in the $|J = 15/2, m_J\rangle$ basis are presented in Tables S13–S15 (the used structural cluster, **S** or **B**, are indicated there).

The calculations performed with bigger structural fragments (cluster **B**) give more reliable results than the ones based using smaller computation clusters for all of compounds **1**–**3**. This statement is supported by the comparison between the calculated $M(H)$ and $\chi_M T(T)$ curves with the experimental ones. Moreover, in the case of one of the Dy(III) complexes in **2**, taking the larger fragment changes the alignment of the anisotropy axis from the perpendicular position to the axially aligned O-donor ligands to the parallel one, as suspected by the results of the *ac* magnetic properties. According to the calculations, using larger molecular fragments yields in lowering of the calculated energy barrier for all of the compounds. For compound **2**, the energy barrier is moderate, while the anisotropy of the pseudo-*g*-tensor and the state purity of the ground Kramers doublet is high. It is the only compound for which anisotropy is proper enough to expect zero-field SMM characteristics (excluding **4**). In the case of the other two, substantial transversal components of the *g*-tensor should shorten the relaxation times due to the fast QTM. Such conclusions are all in full agreement with the experimental data. For **3**, the center with two pyridine ligands seems to be worse magnetically than one with one coordinated methanol molecule, which stays in line with its SMM performance being closer to **1**, than **2**.

Table S12 Description and contractions of the basis set employed in the *ab initio* calculations of the Dy^{III} crystal field.

Basis set
Dy.ANO-RCC-VTZP 8S7P5D3F2G1H
N.ANO-RCC-VDZP 3S2P1D (first coordination sphere) N.ANO-RCC-VDZ 3S2P (other atoms)
O.ANO-RCC-VDZP 3S2P1D (first coordination sphere) O.ANO-RCC-VDZ 3S2P1D (other atoms)
C.ANO-RCC-VDZ 3S2P
H.ANO-RCC-VDZ 2S
Pt.ANO-RCC-VDZ 7S6P4D1F

Table S13 The set of representative results of the *ab initio* calculations for **1**, including the main magnetic axes alignment in relation to the axially aligned O-donor ligands, the energy difference between the first two doublets of the ground $^6H_{15/2}$ multiplet of indicated Dy(III) centers with pseudo-*g*-tensor components, and the composition of the ground doublet presented in the $|J = 15/2, m_J\rangle$ basis.

Dy1 center			
fragment/model		**S** (smaller fragment, see Comment on Page S39 and Table S12)	**B** (bigger fragment, see Comment on Page S39 and Table S12)
axis alignment		perpendicular	perpendicular
energy gap / cm^{-1}		121.1	98.9
pseudo-*g*-tensor	g_x	0.3510	0.8913
	g_y	0.9472	3.7619
	g_z	18.9098	16.6222
composition of the ground doublet		37.9% |−15/2⟩; 37.9% |+15/2⟩; 7.2% |−11/2⟩; 7.2% |+11/2⟩; 2.4% |−7/2⟩; 2.3% |+7/2⟩; 1.2% |−3/2⟩; 1.0% |+3/2⟩; 0.8% |+1/2⟩; 0.5% |−1/2⟩; 0.5% |+5/2⟩; 0.3% |−9/2⟩; 0.3% |−5/2⟩; 0.2% |−13/2⟩; 0.2% |+9/2⟩; 0.1% |+13/2⟩	43.5% |+15/2⟩; 27.0% |−15/2⟩; 9.3% |+11/2⟩; 5.9% |−11/2⟩; 3.8% |+7/2⟩; 2.4% |−7/2⟩; 2.0% |+3/2⟩; 1.3% |−1/2⟩; 1.2% |−3/2⟩; 0.9% |−5/2⟩; 0.7% |+1/2⟩; 0.5% |−9/2⟩; 0.5% |+5/2⟩; 0.4% |+9/2⟩; 0.3% |−13/2⟩; 0.3% |+13/2⟩

Dy2 center			
fragment/model		**S** (smaller fragment, see Comment on Page S39 and Table S12)	**B** (bigger fragment, see Comment on Page S39 and Table S12)
axis alignment		perpendicular	perpendicular
energy gap / cm^{-1}		85.6	62.9
pseudo-*g*-tensor	g_x	0.8913	0.3510
	g_y	3.7619	0.9472
	g_z	16.6222	18.9098
composition of the ground doublet		87.6% |+15/2⟩; 9.8% |+11/2⟩; 1.3% |+7/2⟩; 0.5% |+3/2⟩; 0.3% |−1/2⟩; 0.1% |−9/2⟩; 0.1% |−5/2⟩; 0.1% |+9/2⟩	83.8% |+15/2⟩; 9.1% |+11/2⟩; 3.8% |−15/2⟩; 1.2% |+7/2⟩; 0.6% |+3/2⟩; 0.4% |−11/2⟩; 0.4% |−1/2⟩; 0.2% |−5/2⟩; 0.1% |−13/2⟩; 0.1% |−9/2⟩; 0.1% |−7/2⟩; 0.1% |+9/2⟩

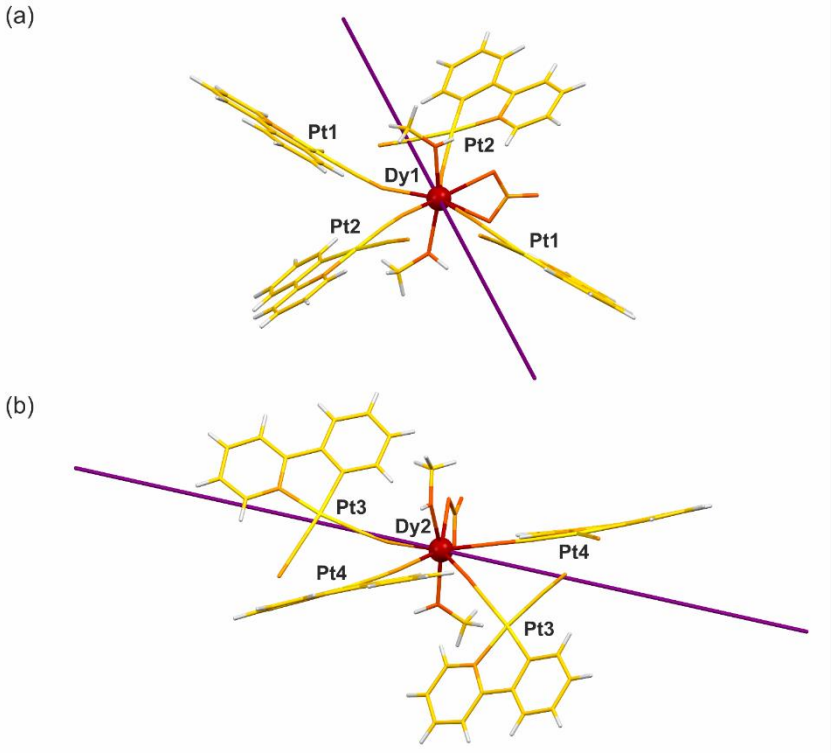

Fig. S20 The visualization of the structural fragments of **1** which were employed for the *ab initio* calculations of the crystal field effect upon the $^6H_{15/2}$ manifold of the Dy(III) centers. In (a) and (b), the bigger fragments (**B**) of the indicated Dy centers are presented (Table S13). The alignment of the magnetic easy axes, resulting from the *ab initio* analysis, is indicated by purple lines.

Table S14 The set of representative results of the *ab initio* calculations for **2**, including the main magnetic axes alignment in relation to the axially aligned O-donor ligands, the energy difference between the first two doublets of the ground $^6H_{15/2}$ multiplet of indicated Dy(III) centers with pseudo-*g*-tensor components, and the composition of the ground doublet presented in the $|J = 15/2, m_J\rangle$ basis.

Dy1 center			
fragment/model		**S** (smaller fragment, see Comment on Page S39 and Table S12)	**B** (bigger fragment, see Comment on Page S39 and Table S12)
axis alignment		perpendicular	perpendicular
energy / cm^{-1}		89.1	66.9
pseudo-*g*-tensor	g_x	0.3335	0.2060
	g_y	0.9154	0.5091
	g_z	18.8880	19.2186
composition of the ground doublet		85.5% $\|-15/2\rangle$; 8.4% $\|-11/2\rangle$; 2.3% $\|+15/2\rangle$; 1.7% $\|-7/2\rangle$; 0.7% $\|-3/2\rangle$; 0.4% $\|-9/2\rangle$; 0.4% $\|+1/2\rangle$; 0.2% $\|+5/2\rangle$; 0.2% $\|+11/2\rangle$; 0.1% $\|+9/2\rangle$; 0.1% $\|+13/2\rangle$	78.1% $\|-15/2\rangle$; 14.7% $\|+15/2\rangle$; 2.9% $\|-11/2\rangle$; 0.1% $\|-9/2\rangle$; 0.9% $\|-7/2\rangle$; 0.7% $\|-3/2\rangle$; 0.7% $\|+11/2\rangle$; 0.3% $\|+1/2\rangle$; 0.2% $\|+9/2\rangle$; 0.1% $\|-13/2\rangle$; 0.1% $\|-1/2\rangle$; 0.1% $\|+3/2\rangle$; 0.1% $\|+5/2\rangle$; 0.1% $\|+7/2\rangle$

Dy2 center			
fragment/model		**S** (smaller fragment, see Comment on Page S39 and Table S12)	**B** (bigger fragment, see Comment on Page S39 and Table S12)
axis alignment		perpendicular	parallel
energy gap / cm^{-1}		77.5	52.6
pseudo-*g*-tensor	g_x	0.5220	0.0200
	g_y	1.6467	0.0275
	g_z	18.3439	19.4871
composition of the ground doublet		77.2% $\|+15/2\rangle$; 11.4% $\|+11/2\rangle$; 5.3% $\|-15/2\rangle$; 2.2% $\|+7/2\rangle$; 1.1% $\|+3/2\rangle$; 0.8% $\|-11/2\rangle$; 0.6% $\|-1/2\rangle$; 0.3% $\|-9/2\rangle$; 0.3% $\|-5/2\rangle$; 0.2% $\|-13/2\rangle$; 0.2% $\|-7/2\rangle$; 0.2% $\|+1/2\rangle$; 0.2% $\|+5/2\rangle$; 0.1% $\|-3/2\rangle$	57.6% $\|+15/2\rangle$; 36.2% $\|-15/2\rangle$; 2.9% $\|+11/2\rangle$; 1.9% $\|-11/2\rangle$; 0.5% $\|+7/2\rangle$; 0.3% $\|-7/2\rangle$; 0.2% $\|+9/2\rangle$; 0.1% $\|-13/2\rangle$; 0.1% $\|-9/2\rangle$; 0.1% $\|+13/2\rangle$

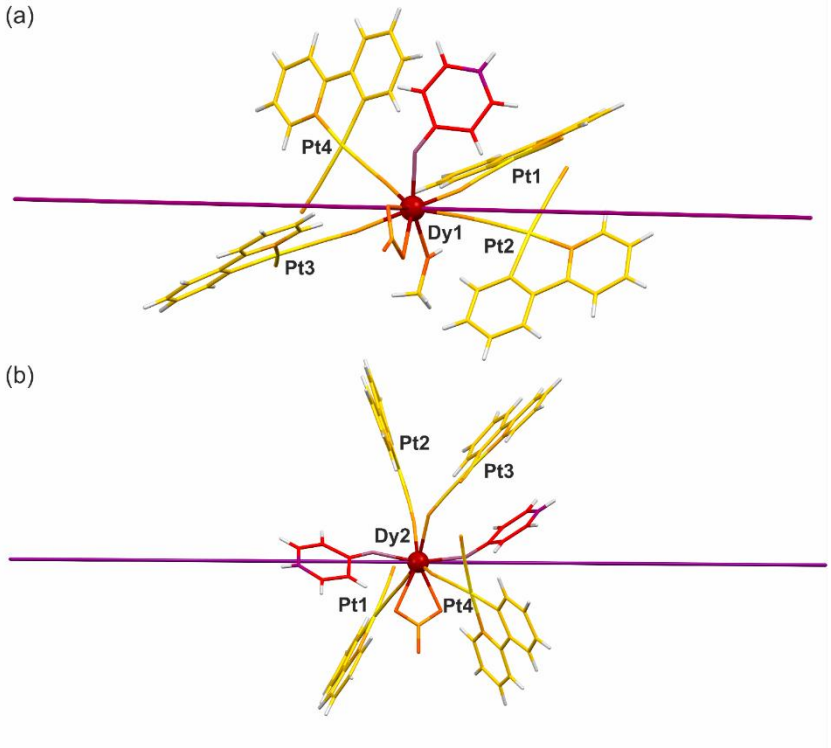

Fig. S21 The visualization of the structural fragments of **2** which were employed for the *ab initio* calculations of the crystal field effect upon the $^{6}H_{15/2}$ manifold of the Dy(III) centers. In (a) and (b), the bigger fragments (**B**) of the indicated Dy centers are presented (Table S14). The alignment of the magnetic easy axes, resulting from the *ab initio* analysis, is indicated by purple lines.

Table S15 The set of representative results of the *ab initio* calculations for **3**, including the main magnetic axes alignment in relation to the axially aligned O-donor ligands, the energy difference between the first two doublets of the ground $^6H_{15/2}$ multiplet of indicated Dy(III) centers with pseudo-*g*-tensor components, and the composition of the ground doublet presented in the $|J = 15/2, m_J\rangle$ basis.

Dy1 center			
fragment/model		**S** (smaller fragment, see Comment on Page S39 and Table S12)	**B** (bigger fragment, see Comment on Page S39 and Table S12)
axis alignment		perpendicular	perpendicular
energy / cm^{-1}		92.7	56.6
pseudo-*g*-tensor	g_x	0.2531	0.3356
	g_y	0.6490	0.9420
	g_z	19.0519	18.8683
composition of the ground doublet		88.0% |−15/2⟩; 6.9% |−11/2⟩; 1.8% |+15/2⟩; 1.5% |−7/2⟩; 0.6% |−3/2⟩; 0.2% |−9/2⟩; 0.2% |+1/2⟩; 0.1% |−5/2⟩; 0.1% |−1/2⟩; 0.1% |+3/2⟩; 0.1% |+5/2⟩; 0.1% |+7/2⟩; 0.1% |+9/2⟩; 0.1% |+11/2⟩	88.6% |−15/2⟩; 6.0% |−11/2⟩; 1.9% |−7/2⟩; 0.9% |−3/2⟩; 0.7% |+15/2⟩; 0.5% |−9/2⟩; 0.4% |+1/2⟩; 0.2% |−1/2⟩; 0.2% |+5/2⟩; 0.2% |+9/2⟩; 0.1% |−13/2⟩; 0.1% |−5/2⟩; 0.1% |+3/2⟩; 0.1% |+7/2⟩; 0.1% |+13/2⟩

Dy2 center			
fragment/model		**S** (smaller fragment, model **2**, see Comment on Page S39 and Table S12)	**B** (bigger fragment, model **2**, see Comment on Page S39 and Table S12)
axis alignment		perpendicular	perpendicular
energy / cm^{-1}		76.5	5.7
pseudo-*g*-tensor	g_x	0.5966	0.7781
	g_y	1.9934	1.4980
	g_z	18.0794	17.0392
composition of the ground doublet		51.3% |+15/2⟩; 29.0% |−15/2⟩; 8.4% |+11/2⟩; 4.8% |−11/2⟩; 1.9% |+7/2⟩; 1.1% |−7/2⟩; 0.9% |+3/2⟩; 0.6% |−1/2⟩; 0.5% |−3/2⟩; 0.4% |−5/2⟩; 0.3% |+1/2⟩; 0.2% |−9/2⟩; 0.2% |+5/2⟩; 0.1% |−13/2⟩; 0.1% |+9/2⟩; 0.1% |+13/2⟩	64.7% |+15/2⟩; 8.3% |−15/2⟩; 6.8% |+11/2⟩; 5.3% |+3/2⟩; 4.5% |+13/2⟩; 3.7% |+5/2⟩; 1.7% |−5/2⟩; 1.1% |−13/2⟩; 1.0% |+9/2⟩; 0.8% |−9/2⟩; 0.6% |−11/2⟩; 0.4% |−3/2⟩; 0.4% |+1/2⟩; 0.3% |−1/2⟩; 0.2% |+7/2⟩; 0.1% |−7/2⟩

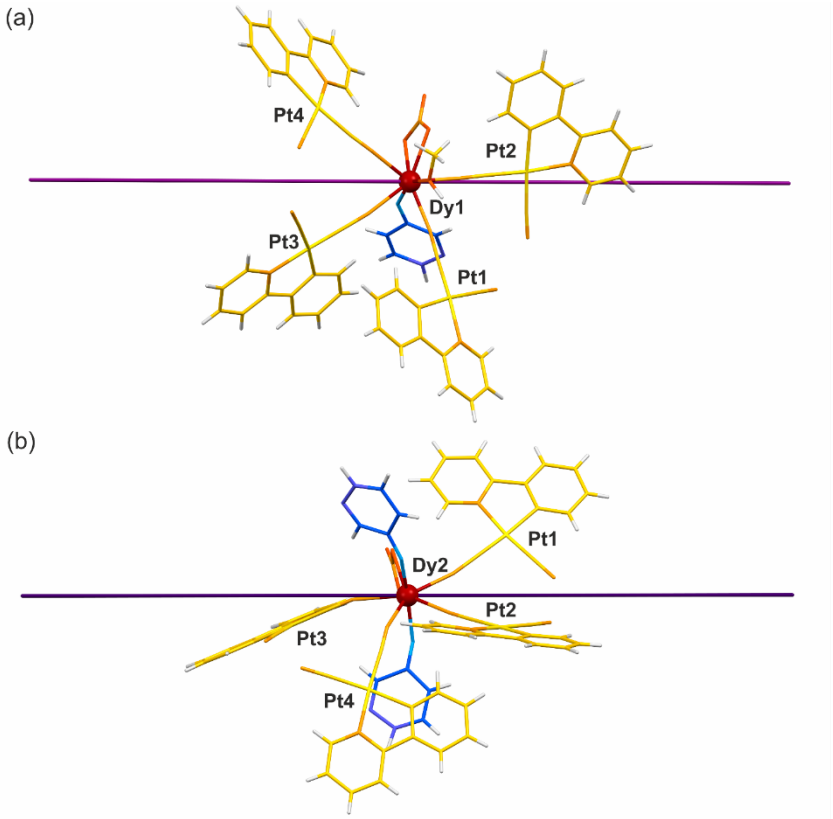

Fig. S22 The visualization of the structural fragments of **3** which were employed for the *ab initio* calculations of the crystal field effect upon the $^6H_{15/2}$ manifold of the Dy(III) centers. In (a) and (b), the bigger fragments (**B**) of the indicated Dy centers are presented (Table S15). The alignment of the magnetic easy axes, resulting from the *ab initio* analysis, is indicated by purple lines.

Comment to Fig. S23–S47 and Tables S16–S19 – *ac* magnetic characteristics

All field- and temperature-variable alternate-current (*ac*) magnetic characteristics were fitted using the relACs program.[S19] Simultaneous fitting procedures for $\chi'(\omega)$, $\chi''(\omega)$, and $\chi''(\chi')$ plots were employed using the generalized Debye model, described by the eq. S9:

$$\chi(\omega) = \chi_S + \frac{\chi_T - \chi_S}{1+(i\omega\tau)^{1-\alpha}} \quad , \qquad \text{eq. S9}$$

where χ is the magnetic susceptibility in cm^3mol^{-1}, χ_S is the adiabatic susceptibility in cm^3mol^{-1}, χ_T is the isothermal susceptibility in cm^3mol^{-1}, ω is a frequency in Hz, τ is the relaxation time in s, and α represents the distribution of relaxation times.[S20]

In some cases, two distinct relaxation processes were visible within the gathered data. Then, the magnetic susceptibility was treated as a sum of two susceptibilities, each following the generalized Debye model for a single relaxation process, thus the fitting was performed for the resulting sum:

$$\chi(\omega) = \chi^I(\omega) + \chi^{II}(\omega) \ . \qquad \text{eq. S10}$$

The obtained best-fit curves are gathered in Fig. S23–S47 as plots (a–c), while the resulting relaxation times were plotted against the magnetic field or temperature as plots (d). The latter were simultaneously fitted within relACs using the whole set of dependencies for each system, taking into account the minimal number (to avoid parameterization) of magnetic relaxation processes, chosen from an Orbach thermal relaxation, a field-induced direct process, a quantum tunneling of magnetization (QTM) effect, and a two-phonon Raman spin-lattice relaxation. The most general expression is represented by the eq. S11:

$$\tau^{-1}(H,T) = \tau_0 \, exp\left(\frac{-\Delta E}{k_B T}\right) + AH^n T + \frac{B_1}{(1+B_2H^2)} + CT^N \quad , \qquad \text{eq. S11}$$

where the first term describes the Orbach thermal relaxation pathway, the second one represents the field-induced direct process, the third component stands for the temperature-independent QTM effect, and the last one depicts the Raman spin-lattice relaxation.[S21] The indicated magnetic field, *H*, is in Oe, while the temperature, *T*, is in K.

For **4**, it was noted, that the *C* parameter of the Raman relaxation changes significantly with the applied external magnetic field. Such a case was not possible to take into account within the reACs program, so the field dependence of the relaxation time was fitted separately, following the corrected equation:

$$\tau^{-1}(H,T) = AH^n T + \frac{B_1}{(1+B_2H^2)} + \left(\frac{1+aH^2}{1+bH^2}\right) CT^N + const \quad , \qquad \text{eq. S12}$$

where *const* represents the Orbach thermal relaxation, while *a* and *b* describe the field-dependence of the term corresponding to the Raman relaxation pathway.[S22]

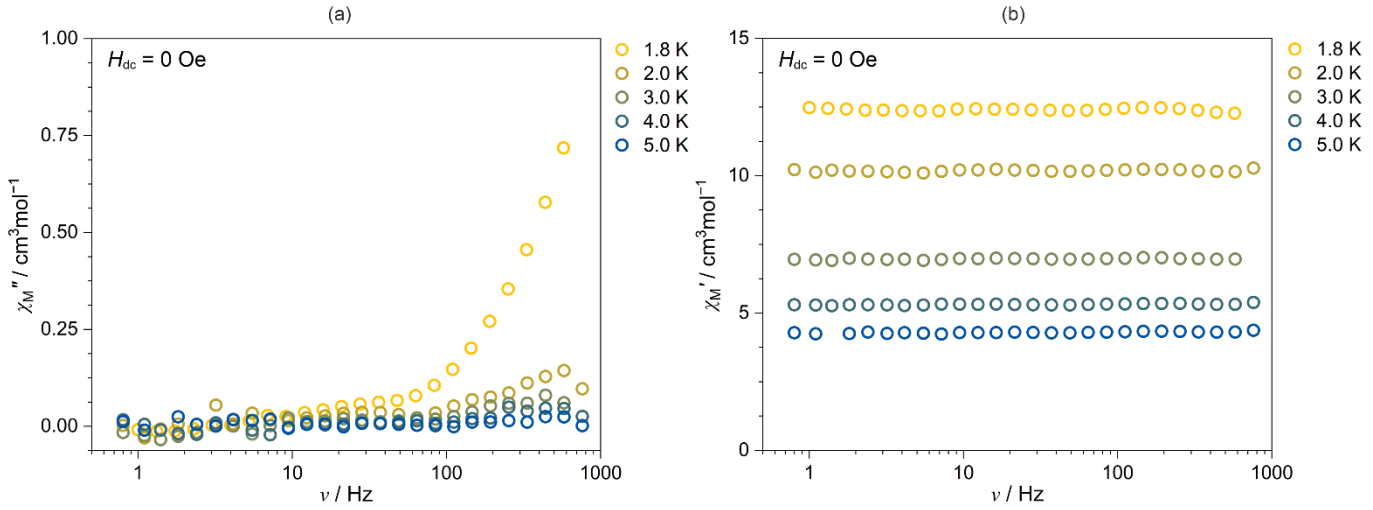

Fig. S23 Temperature-variable alternate-current (*ac*) magnetic characteristics of **1** under zero *dc* field, including the frequency dependences of (a) the out-of-phase susceptibility, χ_M''(υ), and (b) the in-phase susceptibility, χ_M'(υ), at the indicated temperatures. The maxima on the χ_M''(υ) plots, representing relaxation times, are located outside the measurement range. Therefore no fitting was done as such would result in unreliable parameters.

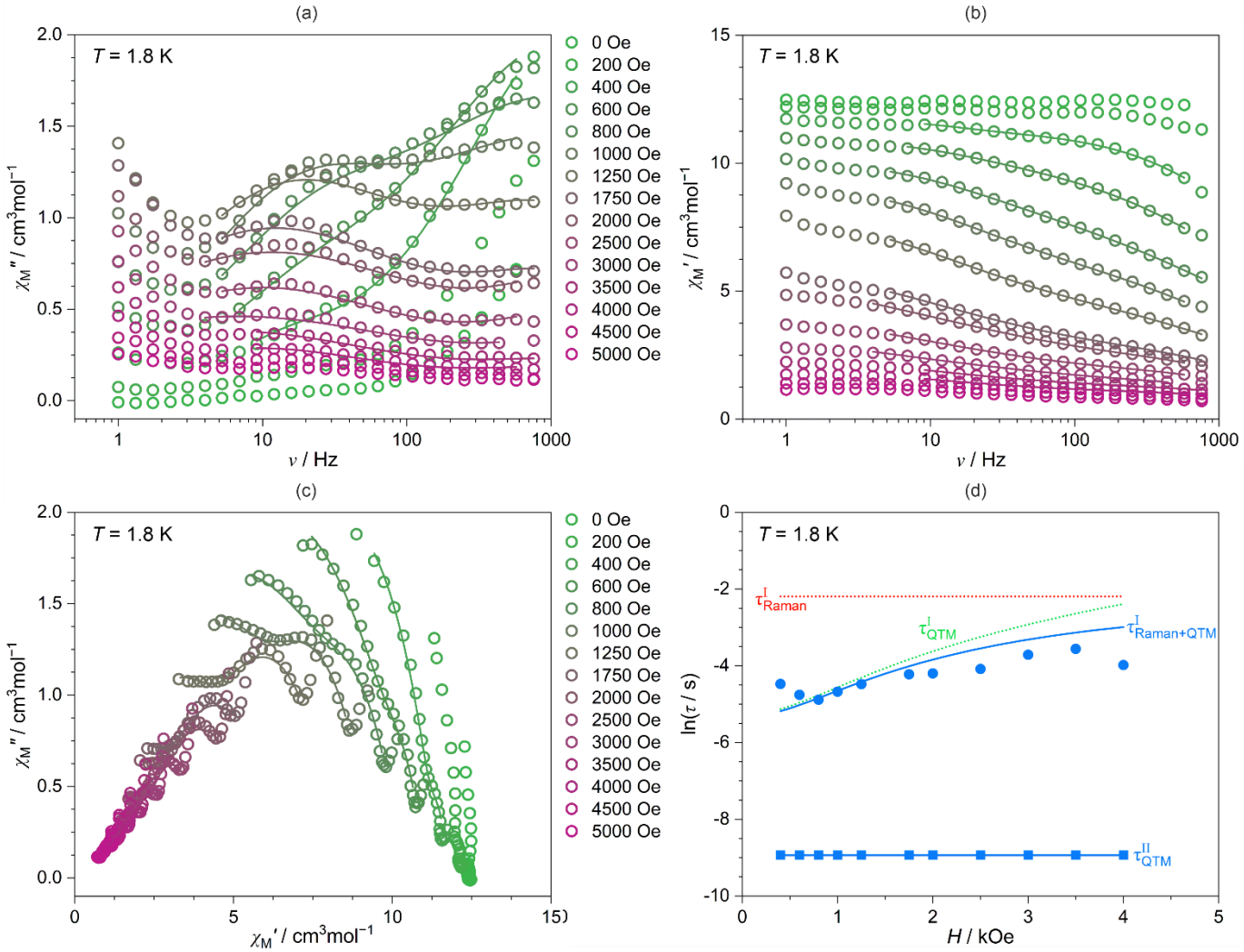

Fig. S24 Magnetic-field-variable full *ac* magnetic characteristics of **1** at T = 1.8 K, shown with the related analyses. The Fig. includes the frequency dependences of (a) the out-of-phase susceptibility, χ_M"(υ), and (b) the in-phase susceptibility, χ_M'(υ), under the indicated H_{dc} values, (c) the related Argand plots, χ_M"(χ_M'), and (d) the field dependence of the resulting relaxation times, τ. Colored solid curves in (a–c) represent the best fits obtained using the generalized Debye model for a double relaxation process. The blue solid lines in (d) show the simultaneous fit for both T and H dependencies of relaxation time, while the dashed colored lines represent the respective course of each relaxation process included. The obtained best-fit parameters are gathered in Table S16.

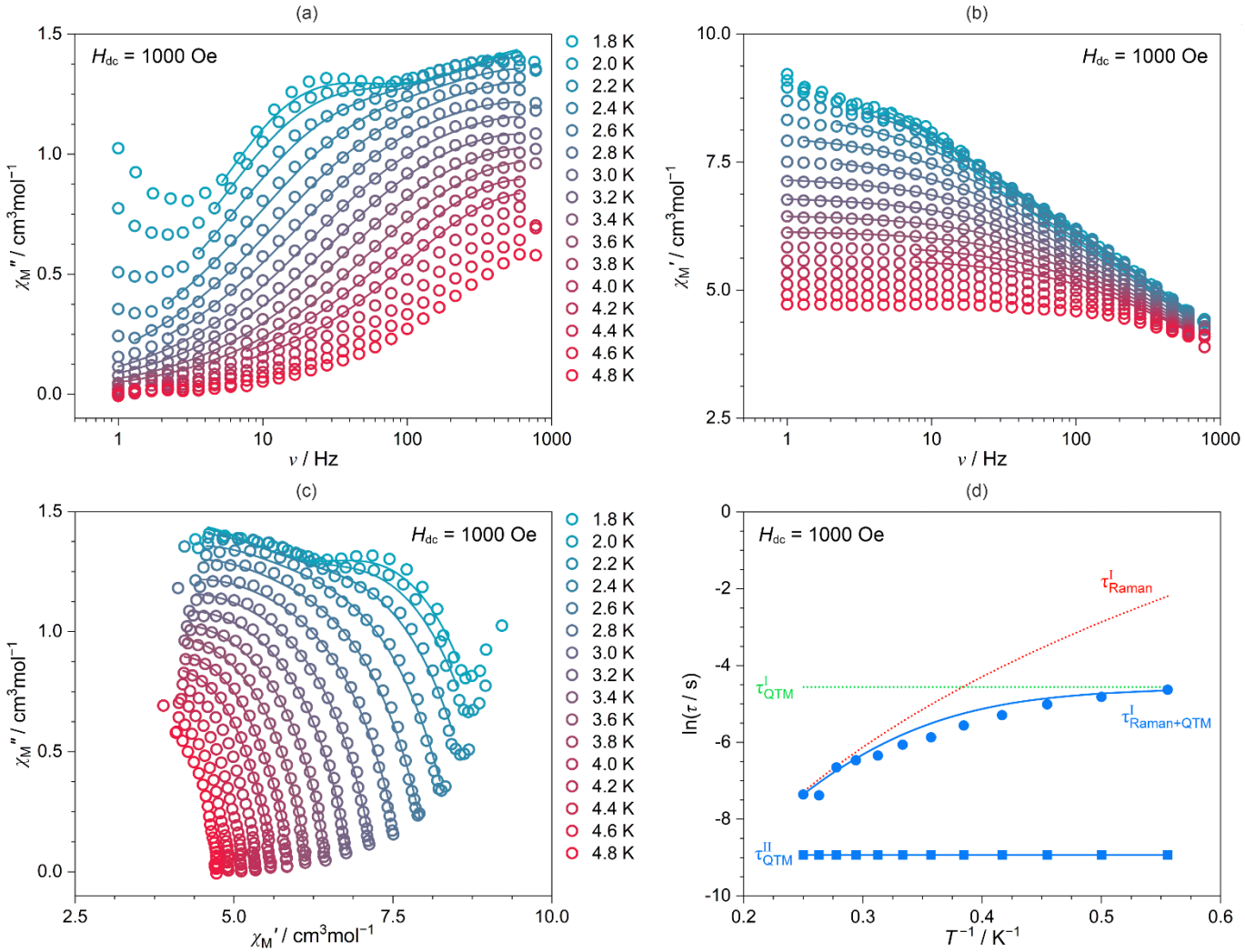

Fig. S25 Temperature-variable full *ac* magnetic characteristics of **1** under H_{dc} = 1 kOe, shown with the related analyses. This Fig. includes the frequency dependences of (a) the out-of-phase susceptibility, χ_M''(υ), and (b) the in-phase susceptibility, χ_M'(υ), collected in the indicated T regime, (c) the related Argand plots, χ_M''(χ_M'), and (d) the temperature dependence of the resulting relaxation times, τ. Colored solid curves in (a–c) represent the best fits obtained using the generalized Debye model for a double relaxation process. The blue solid lines in (d) show the simultaneous fit for both T and H dependencies of the relaxation time, while the dashed colored lines represent the respective course of each process included. The obtained best-fit parameters are gathered in Table S16.

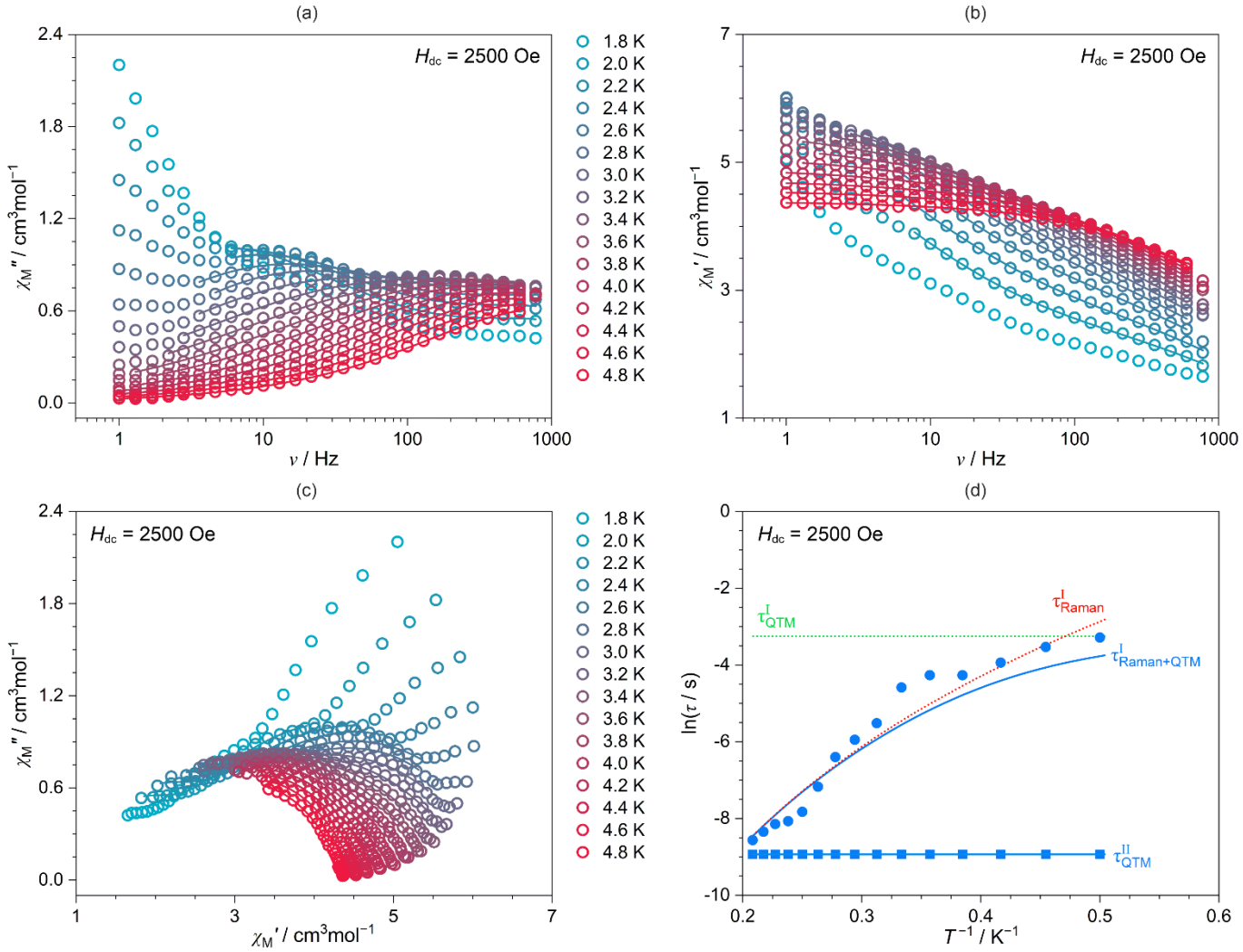

Fig. S26 Temperature-variable full *ac* magnetic characteristics of **1** under H_{dc} = 2.5 Oe, shown with the related analyses. This Fig. includes the frequency dependences of (a) the out-of-phase susceptibility, χ_M''(υ), and (b) the in-phase susceptibility, χ_M'(υ), collected in the indicated T regime, (c) the related Argand plots, χ_M''(χ_M'), and (d) the temperature dependence of the resulting relaxation times, τ. Colored solid curves in (a–c) represent the best fits obtained using the generalized Debye model for a double relaxation process. The blue solid lines in (d) show the simultaneous fit for both T and H dependencies of the relaxation time, while the dashed colored lines represent the respective course of each process included. The obtained best-fit parameters are gathered in Table S16.

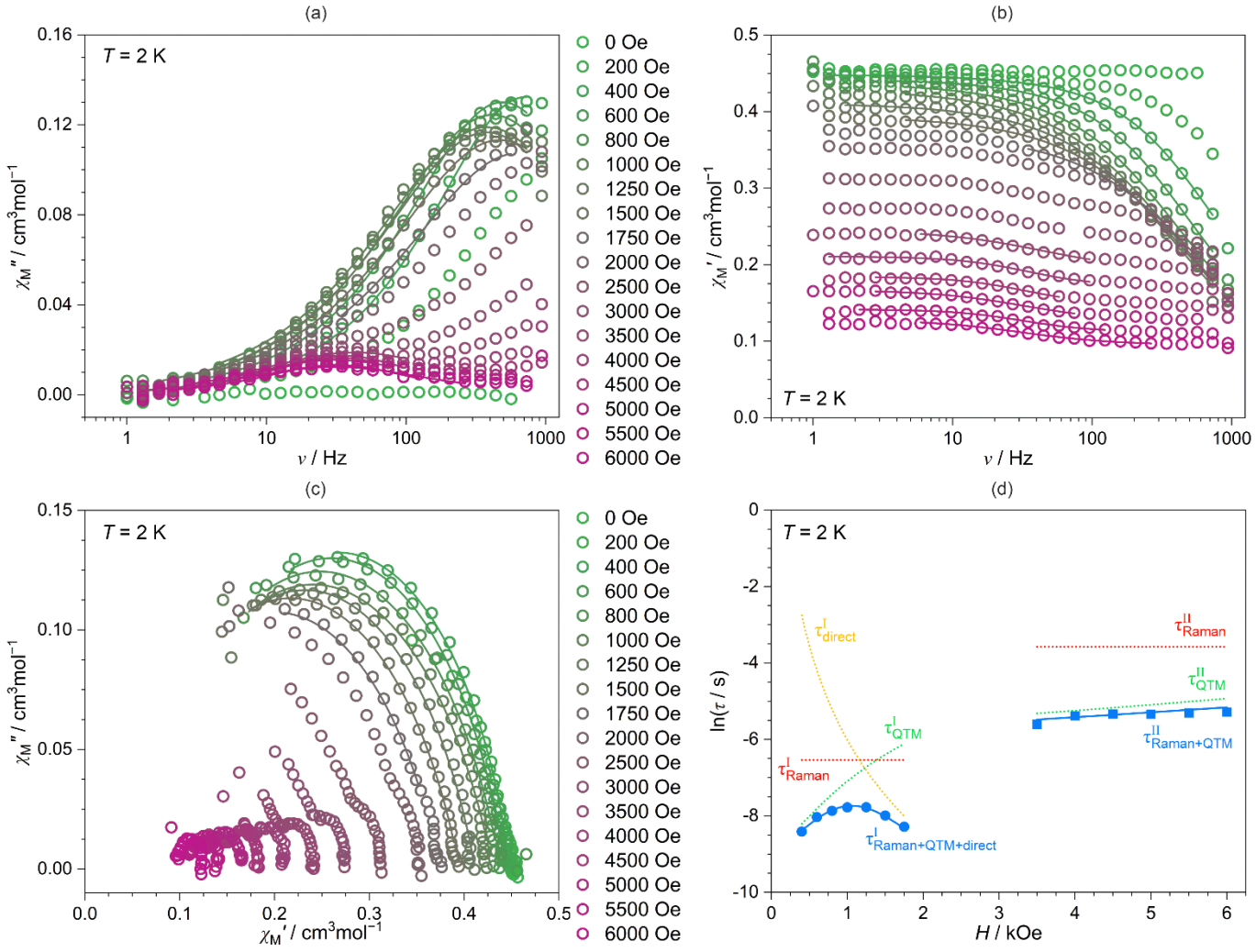

Fig. S27 Magnetic-field-variable full *ac* magnetic characteristics of **1md** at $T = 2$ K, shown with the related analyses. This Fig. includes the frequency dependences of (a) the out-of-phase susceptibility, χ_M"(υ), and (b) the in-phase susceptibility, χ_M'(υ), under the indicated H_{dc} values, (c) the related Argand plots, χ_M"(χ_M'), and (d) the field dependence of the resulting relaxation times, τ. Colored solid curves in (a–c) represent the best fits obtained using the generalized Debye model for a single relaxation process. The blue solid lines in (d) show the simultaneous fits for both T and H dependencies of the relaxation times, while the dashed colored lines represent the respective course of each process included. The obtained best-fit parameters are gathered in Table S16.

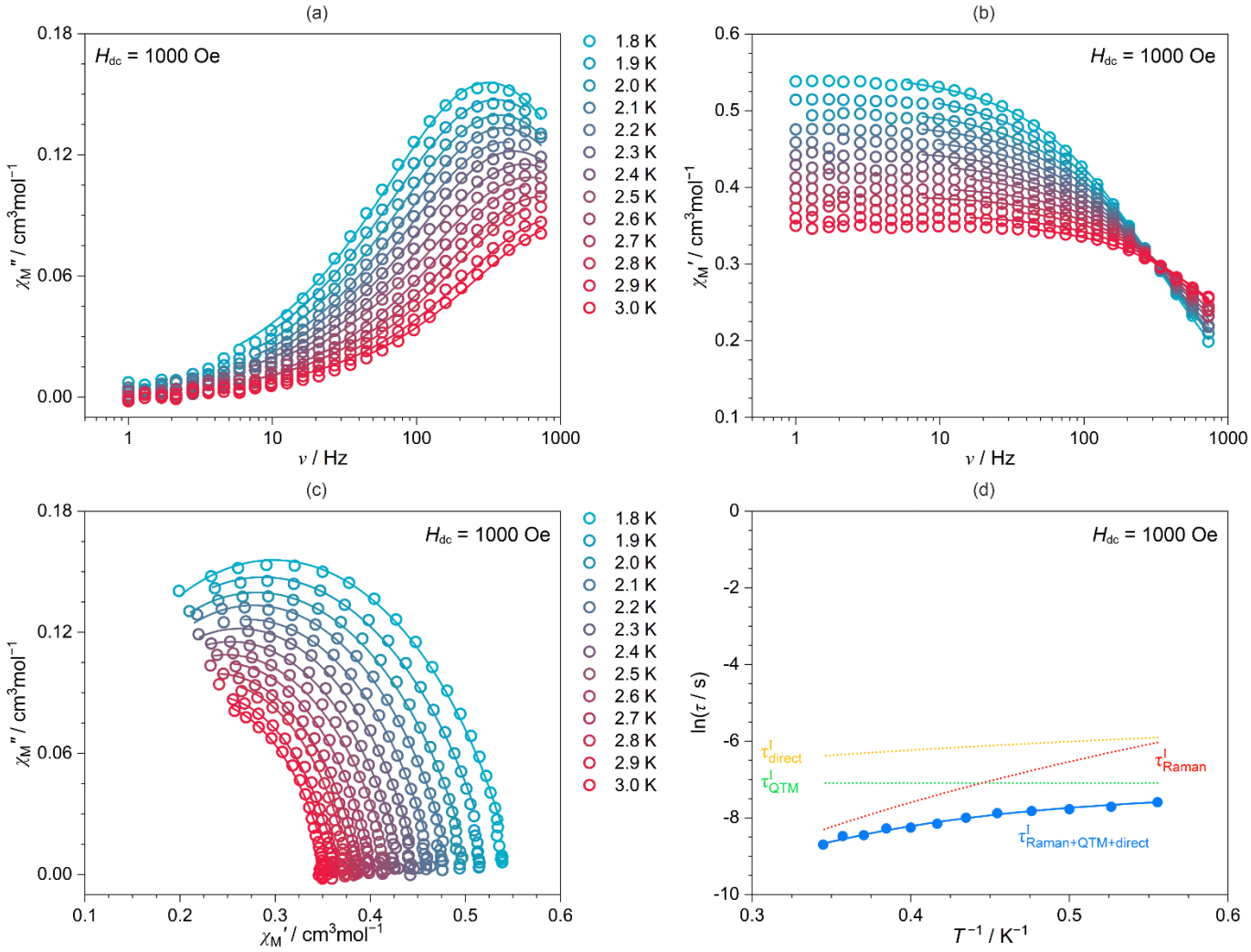

Fig. S28 Temperature-variable full *ac* magnetic characteristics of **1md** under H_{dc} = 1 kOe, shown with the related analyses. This Fig. includes the frequency dependences of (a) the out-of-phase susceptibility, χ_M''(υ), and (b) the in-phase susceptibility, χ_M'(υ), collected in the indicated T regime, (c) the related Argand plots, χ_M''(χ_M'), and (d) the temperature dependence of the resulting relaxation times, τ. Colored solid curves in (a–c) represent the best fits obtained using the generalized Debye model for a single relaxation process. The blue solid line in (d) shows the simultaneous fit for both T and H dependencies of the relaxation time, while the dashed colored lines represent the respective course of each process included. The obtained best-fit parameters are gathered in Table S16.

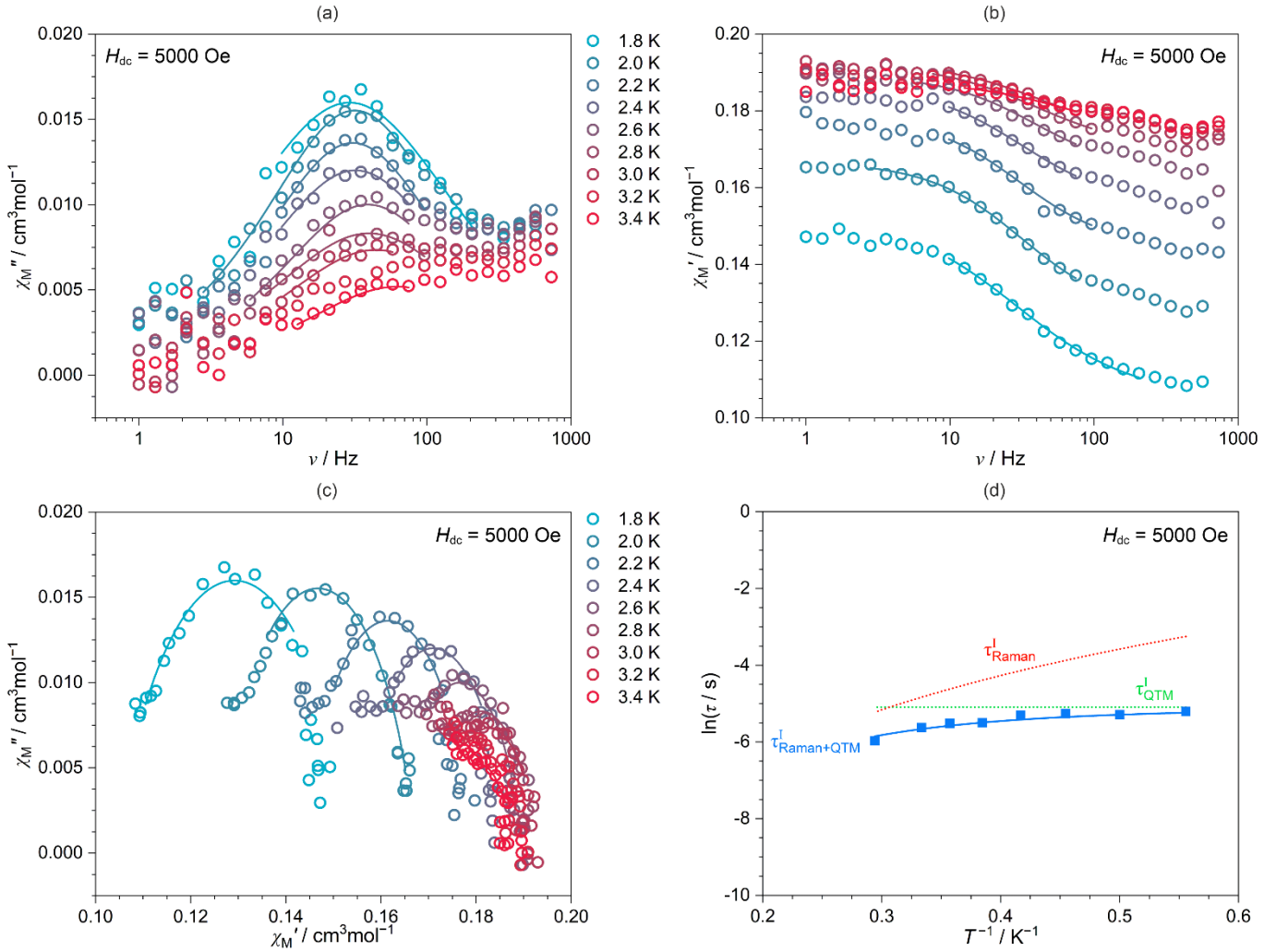

Fig. S29 Temperature-variable full *ac* magnetic characteristics of **1md** under H_{dc} = 5 kOe, shown with the related analyses. This Fig. includes the frequency dependences of (a) the out-of-phase susceptibility, χ_M''(υ), and (b) the in-phase susceptibility, χ_M'(υ), collected in the indicated T regime, (c) the related Argand plots, χ_M''(χ_M'), and (d) the temperature dependence of the resulting relaxation times, τ. Colored solid curves in (a–c) represent the best fits obtained using the generalized Debye model for a single relaxation process. The blue solid line in (d) shows the simultaneous fit for both T and H dependencies of the relaxation time, while the dashed colored lines represent the respective course of each process included. The obtained best-fit parameters are gathered in Table S16.

Table S16 Summary of the critical (best-fit) parameters of the relaxation processes determined for **1** and **1md**, obtained within the simultaneous fitting procedure of field and temperature dependencies of the relaxation time (see Fig. S24–S29 and the comment on Page S46), gathered together with the theoretical energy barriers obtained within the *ab initio* calculations performed using SC-XRD structural data collected for **1**.

compound	**1**	**1md**
relaxation I		
A / $s^{-1}K^{-1}Oe^{-n}$	—	$4.27(6)\cdot10^{-9}$
n	—	3.46(2)
B_1 / s^{-1}	$2.0(3)\cdot10^{2}$	$6(1)\cdot10^{3}$
B_2 / Oe^{-2}	$1.1(2)\cdot10^{-6}$	$4.0(2)\cdot10^{-6}$
C / $s^{-1}K^{-N}$	$2.1(2)\cdot10^{-3}$	25(5)
N	6.38(8)	4.77(2)
relaxation II		
B_1 / s^{-1}	7586 (fixed)	271(8)
B_2 / Oe^{-2}	—	$2.6(2)\cdot10^{-8}$
C / $s^{-1}K^{-N}$	—	4.2(3)
N	—	3.11(7)
energy barrier values (ΔE), obtained from the *ab initio* calculations (Table S13)	Dy1	98.9 cm^{-1}
	Dy2	62.9 cm^{-1}

Comment to Fig. S24-S29 and Table S16 – fitting of the *ac* magnetic data for 1 and 1md

Fitting procedure for 1

To make the fitting of the *ac* magnetic data possible, the generalized Debye model for a double relaxation process had to be employed. However, this led to overparameterization, and the initial temperature dependences of the resulting relaxation times were found unreliable. To avoid the latter, it was assumed that the faster relaxation can be described by an entirely field-independent process, thus the corresponding relaxation time, τ^{II}, was fixed at $1.318 \cdot 10^{-4}$ s. Then, the relaxation times for a slower relaxation process, τ^{I}, could be reasonably extracted and both *T* and *H* dependences could be reasonably fitted within a simultaneous fit employed in the relACs program taking into account the minimal number of different magnetic relaxation pathways, including the QTM effect and Raman spin-lattice relaxation.

Fitting procedure for 1md

As for the non-diluted sample **1**, the preliminary results of the *ac* magnetic characterization for **1md** revealed no reasonable signal related at zero *dc* field within the studied range of frequencies. After employing an external field, it was noted, that in the measured range there are two distinct relaxation processes visible. For the first of them, the optimal H_{dc} is 1 kOe, while with the field increasing it vanishes, and then another process appears at ca. 5 kOe (see Fig. S27). The whole set of relaxation times for both of them was simultaneously fitted taking into account *H* dependency and the minimal number of different magnetic relaxation processes. In the case of relaxation I (at the low field), the field-induced direct process, QTM effect, and the Raman spin-lattice relaxation were necessary to describe the observed field-induced SMM behavior, while for relaxation II, only the QTM effect and the Raman spin-lattice relaxation were found critical to reasonably reproduce the experimental data.

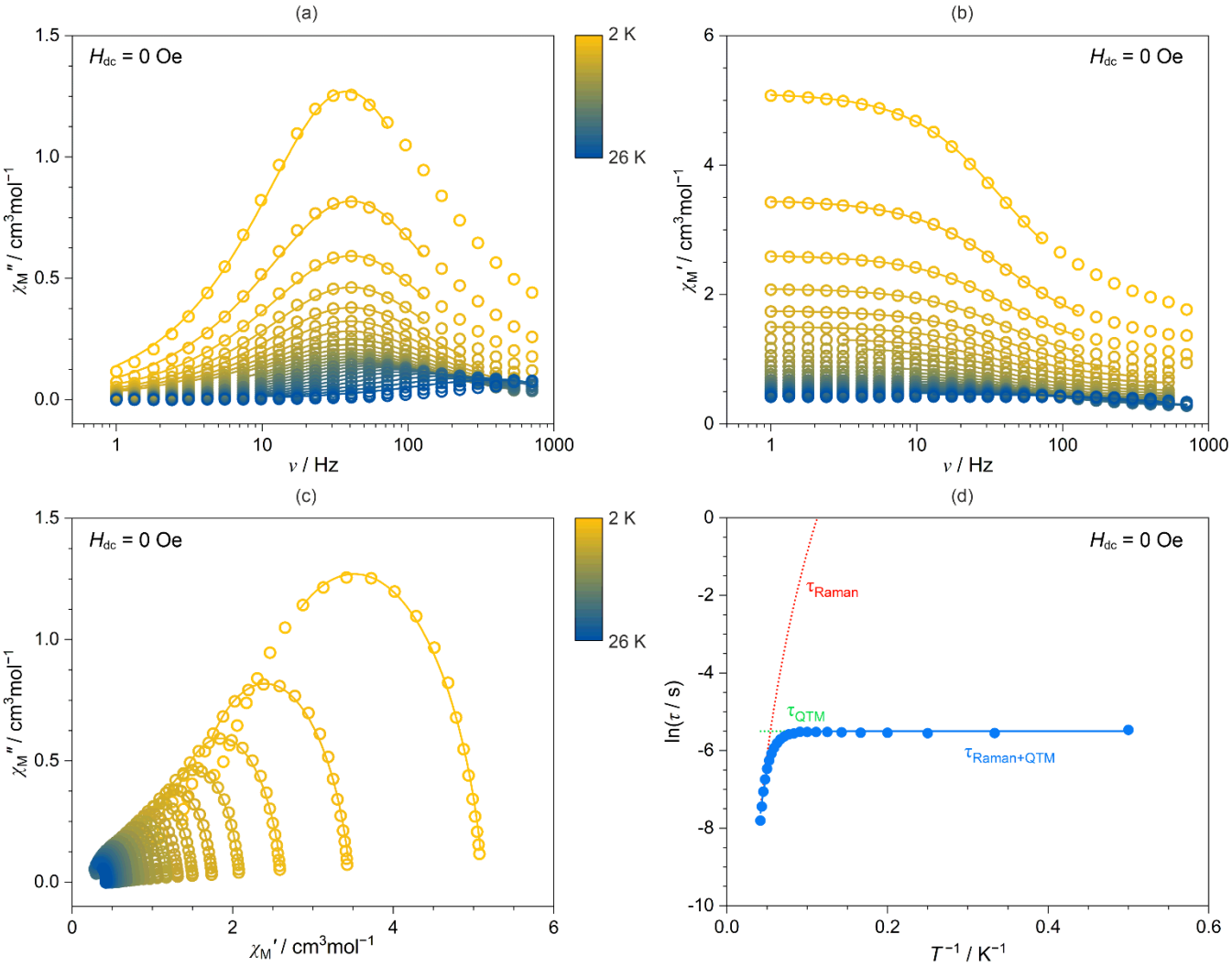

Fig. S30 Temperature-variable full *ac* magnetic characteristics of **2** under zero *dc* field, shown with the related analyses. This Fig. includes the frequency dependences of (a) the out-of-phase susceptibility, χ_M''(υ), and (b) the in-phase susceptibility, χ_M'(υ), collected in the indicated T regime, (c) the related Argand plots, χ_M''(χ_M'), and (d) the temperature dependence of the resulting relaxation times, τ. Colored solid curves in (a–c) represent the best fits obtained using the generalized Debye model for a single relaxation process. The blue solid line in (d) shows the simultaneous fit for both T and H dependencies of the relaxation time, while the dashed colored lines represent the respective course of each process included. The obtained best-fit parameters are gathered in Table S17.

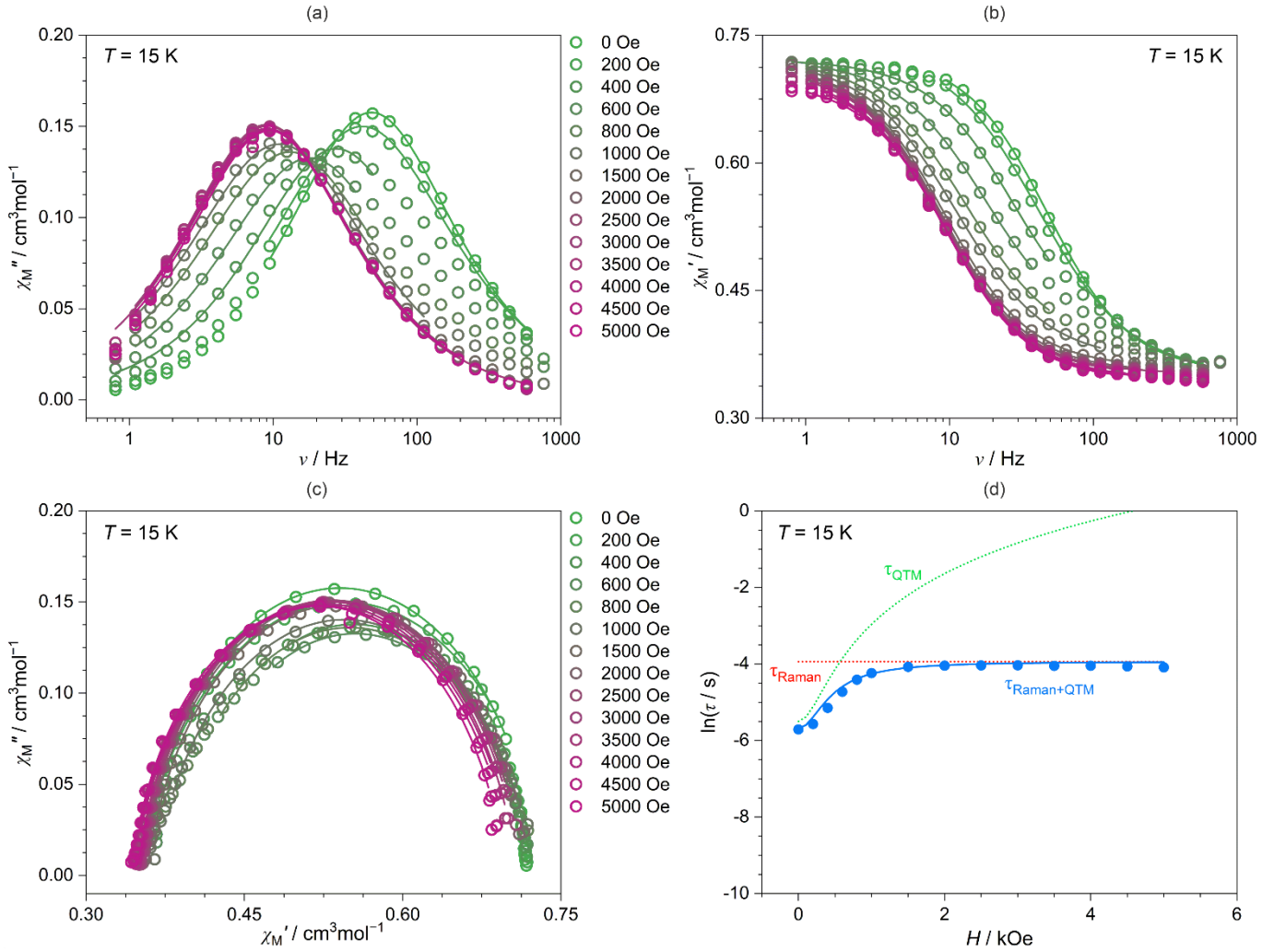

Fig. S31 Magnetic-field-variable full *ac* magnetic characteristics of **2** at $T = 15$ K, shown with the related analyses. This Fig. includes the frequency dependences of (a) the out-of-phase susceptibility, χ_M"(υ), and (b) the in-phase susceptibility, χ_M'(υ), under the indicated H_{dc} values, (c) the related Argand plots, χ_M"(χ_M'), and (d) the field dependence of the resulting relaxation times, τ. Colored solid curves in (a–c) represent the best fits obtained using the generalized Debye model for a single relaxation process. The blue solid line in (d) shows the simultaneous fit for both T and H dependencies of the relaxation time, while the dashed colored lines represent the respective course of each process included. The obtained best-fit parameters are gathered in Table S17.

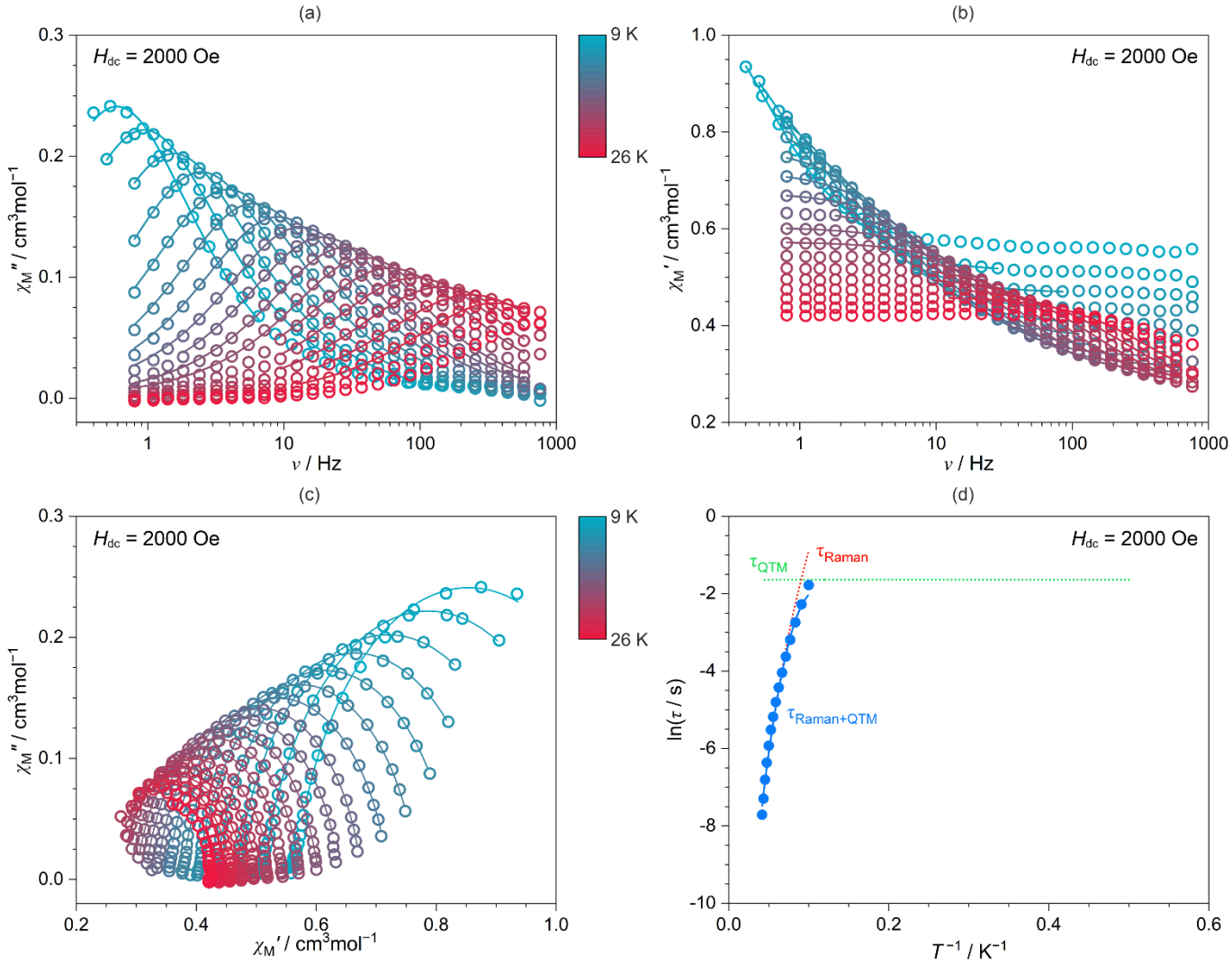

Fig. S32 Temperature-variable full *ac* magnetic characteristics of **2** under H_{dc} = 2 kOe, shown with the related analyses. This Fig. includes the frequency dependences of (a) the out-of-phase susceptibility, χ_M''(υ), and (b) the in-phase susceptibility, χ_M'(υ), collected in the indicated T regime, (c) the related Argand plots, χ_M''(χ_M'), and (d) the temperature dependence of the resulting relaxation times, τ. Colored solid curves in (a–c) represent the best fits obtained using the generalized Debye model for a single relaxation process. The blue solid line in (d) shows the simultaneous fit for both T and H dependencies of the relaxation time, while the dashed colored lines represent the respective course of each process included. The obtained best-fit parameters are gathered in Table S17.

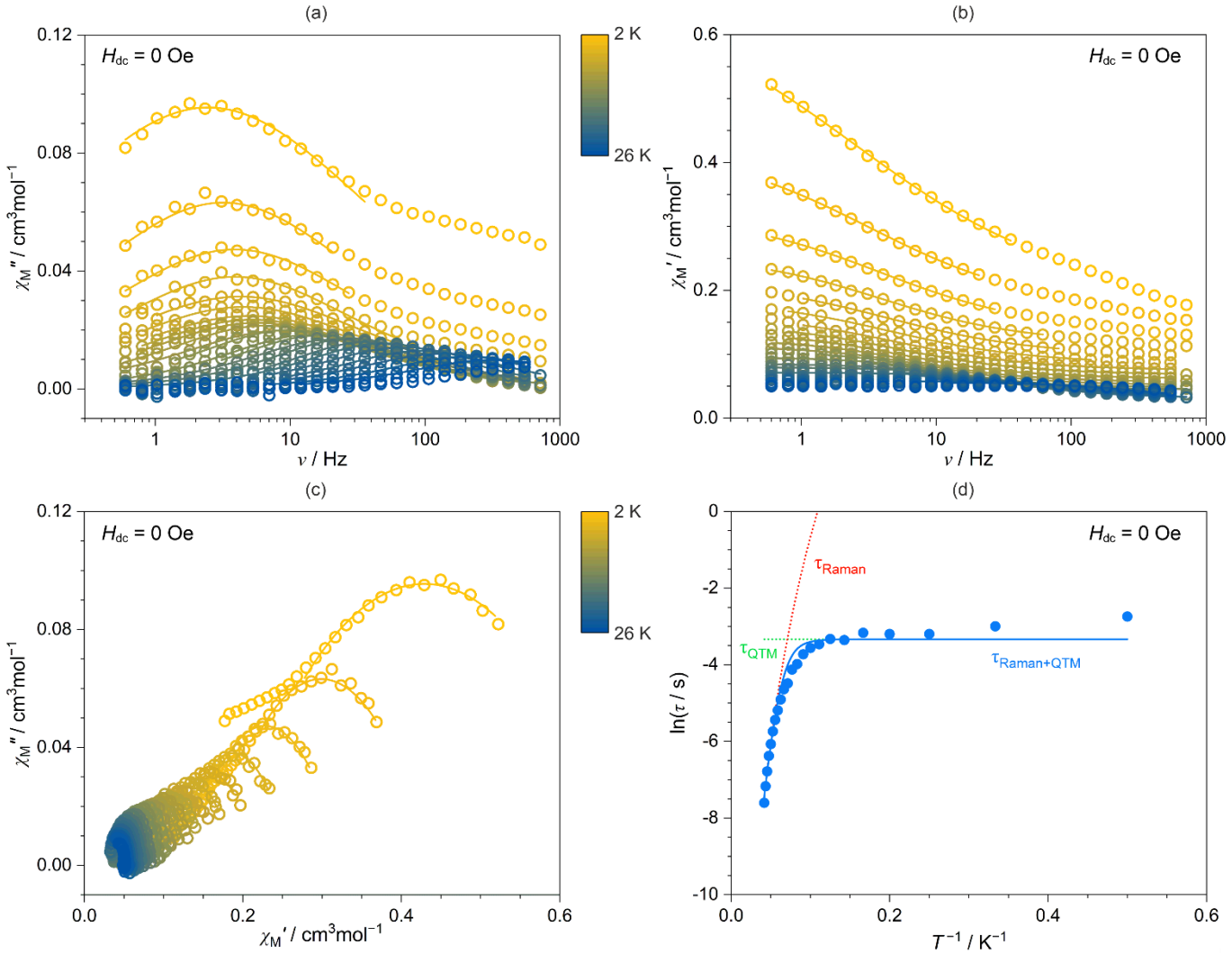

Fig. S33 Temperature-variable full *ac* magnetic characteristics of **2md** under zero *dc* field, shown with the related analyses. This Fig. includes the frequency dependences of (a) the out-of-phase susceptibility, χ_M''(υ), and (b) the in-phase susceptibility, χ_M'(υ), collected in the indicated T regime, (c) the related Argand plots, χ_M''(χ_M'), and (d) the temperature dependence of the resulting relaxation times, τ. Colored solid curves in (a–c) represent the best fits obtained using the generalized Debye model for a single relaxation process. The blue solid line in (d) shows the simultaneous fit for both T and H dependencies of the relaxation time, while the dashed colored lines represent the respective course of each process included. The obtained best-fit parameters are gathered in Table S17.

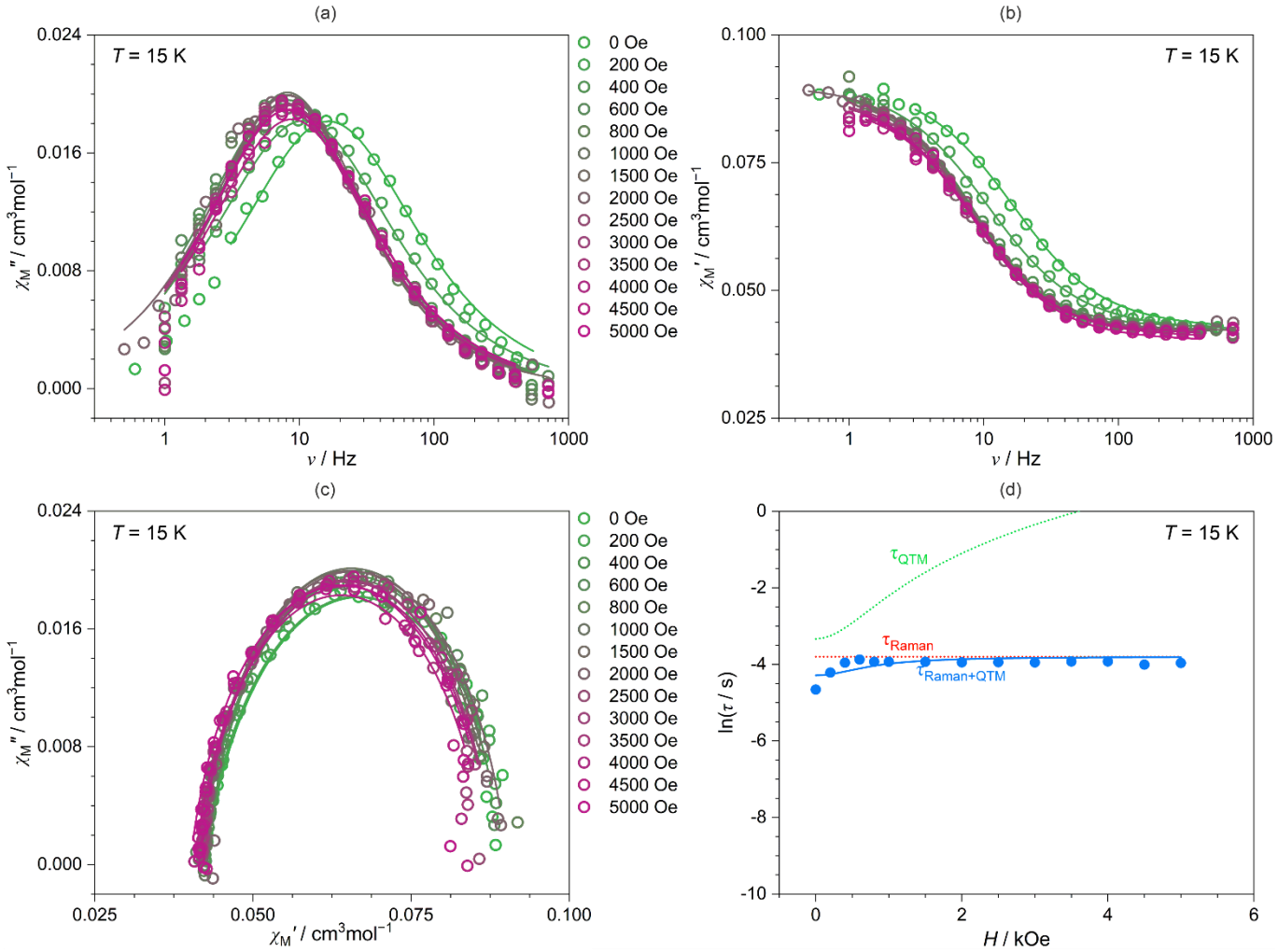

Fig. S34 Magnetic-field-variable full *ac* magnetic characteristics of **2md** at $T = 15$ K, shown with the related analyses. This Fig. includes the frequency dependences of (a) the out-of-phase susceptibility, χ_M"(υ), and (b) the in-phase susceptibility, χ_M'(υ), under the indicated H_{dc} values, (c) the related Argand plots, χ_M"(χ_M'), and (d) the field dependence of the resulting relaxation times, τ. Colored solid curves in (a–c) represent the best fits obtained using the generalized Debye model for a single relaxation process. The blue solid line in (d) shows the simultaneous fit for both T and H dependencies of the relaxation time, while the dashed colored lines represent the respective course of each process included. The obtained best-fit parameters are gathered in Table S17.

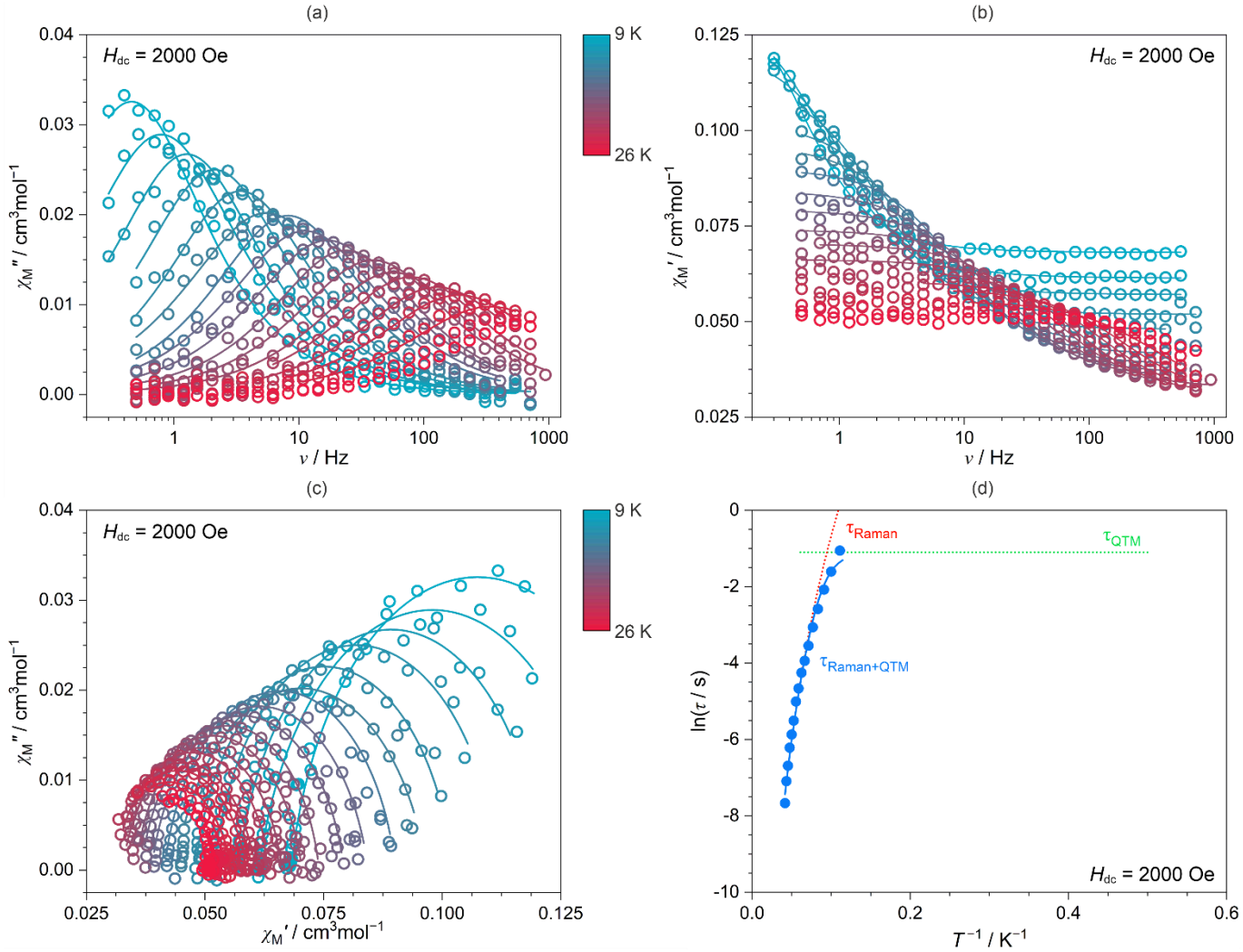

Fig. S35 Temperature-variable full *ac* magnetic characteristics of **2md** under H_{dc} = 2 kOe, shown with the related analyses. This Fig. includes the frequency dependences of (a) the out-of-phase susceptibility, χ_M''(υ), and (b) the in-phase susceptibility, χ_M'(υ), collected in the indicated T regime, (c) the related Argand plots, χ_M''(χ_M'), and (d) the temperature dependence of the relaxation time, τ. Colored solid curves in (a–c) represent the best fits obtained using the generalized Debye model for a single relaxation process. The blue solid line in (d) shows the simultaneous fit for both T and H dependencies of the relaxation time, while the dashed colored lines represent the respective course of each process included. The obtained best-fit parameters are gathered in Table S17.

Table S17 Summary of the critical (best-fit) parameters of the relaxation processes determined for **2** and **2md**, obtained within the simultaneous fitting procedure of field and temperature dependencies of the relaxation time (see Fig. S30–S35 and the comment on Page S46), gathered together with the theoretical energy barriers obtained within the *ab initio* calculations performed using SC-XRD structural data collected for **2**.

compound	**2**	**2md**
B_1 / s^{-1}	$2.44(6)\cdot10^{2}$	28(2)
B_2 / Oe^{-2}	$1.2(1)\cdot10^{-5}$	$2.1(6)\cdot10^{-6}$
C / $s^{-1}K^{-N}$	$7.2(2)\cdot10^{-8}$	$6.8(2)\cdot10^{-8}$
N	7.529(9)	7.24(2)
energy barrier values (ΔE), obtained from the *ab initio* calculations (smaller fragment, Table S14)	Dy1	89.1 cm^{-1}
	Dy2	77.5 cm^{-1}

Comment to Fig. S25-S30 and Table S17 – fitting of the *ac* magnetic data for 2 and 2md

Fitting procedure

The whole set of dependences for **2** and **2md** was simultaneously fitted taking into account the Raman spin-lattice relaxation and QTM effect. The set of dependences of **2** was found possible to be also described using only the Orbach thermal relaxation pathway and the QTM effect, but the lack of agreement between the experimental and theoretical energy barrier of the Orbach process, as well as impossibility of describing similarly the dataset collected for **2md**, suggest to include only the initially selected terms of eq. S11. None of the parameters had to be constrained, and the fit was stable for both **2** and **2md**.

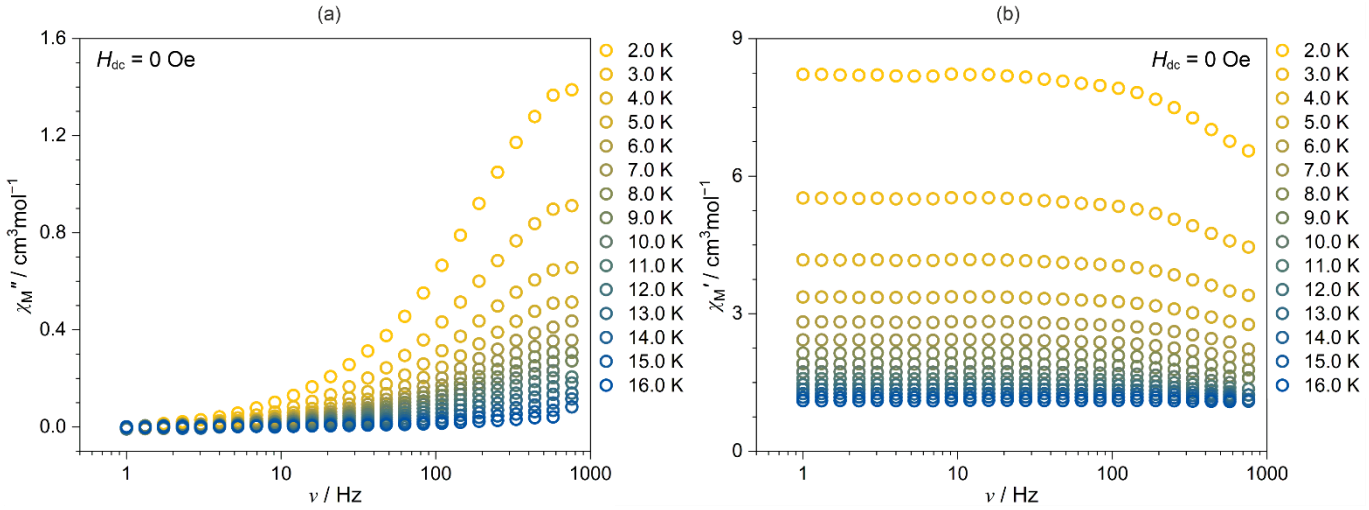

Fig. S36 Temperature-variable *ac* magnetic characteristics of **3** under zero *dc* field, including the frequency dependences of (a) the out-of-phase susceptibility, χ_M''(υ), and (b) the in-phase susceptibility, χ_M'(υ), at the indicated temperatures. The maxima on the χ_M''(υ) plots, representing relaxation times, are located outside the measurement range. Therefore no fitting was done as such would result in unreliable parameters.

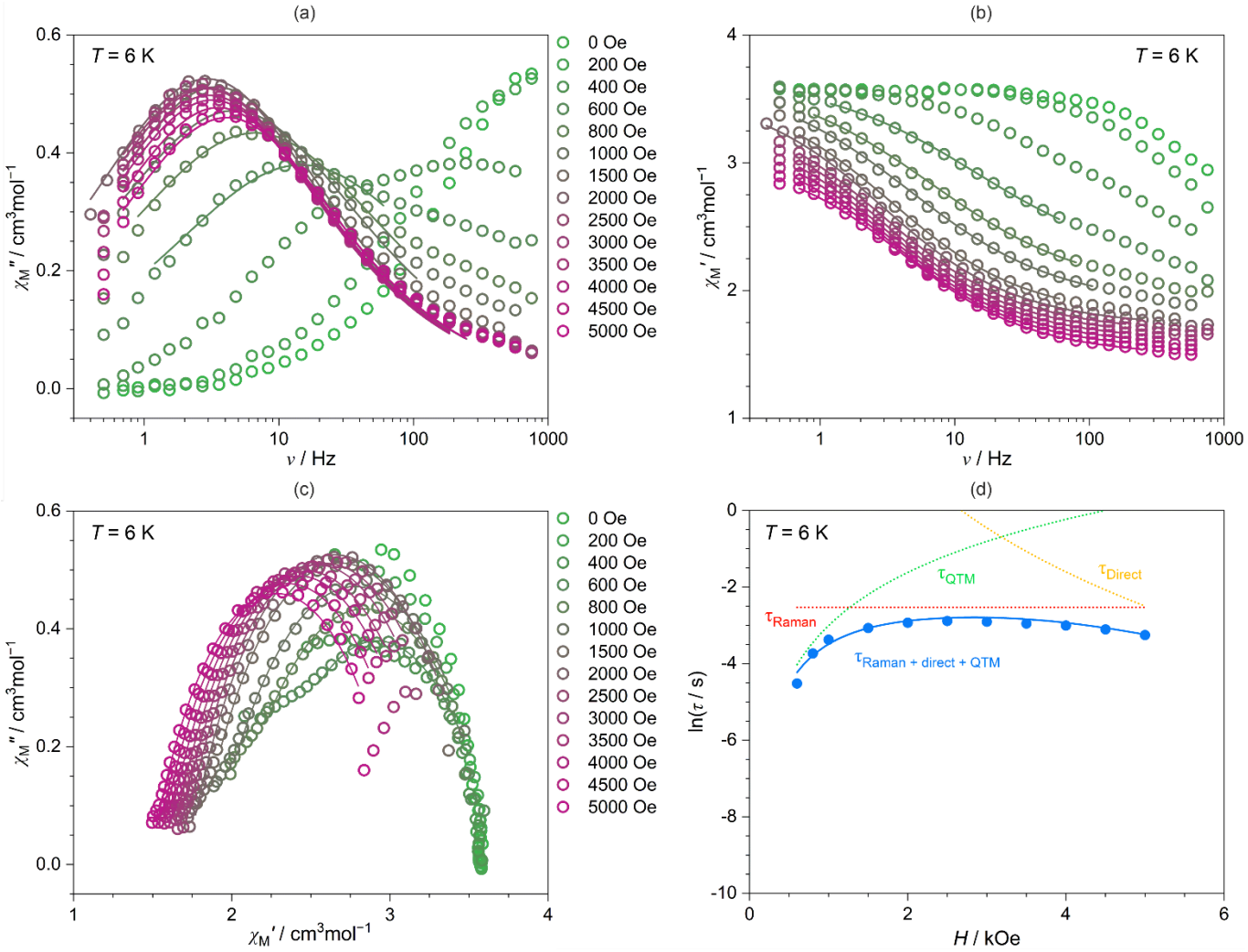

Fig. S37 Magnetic-field-variable full *ac* magnetic characteristics of **3** at T = 6 K, shown with the related analyses. This Fig. includes the frequency dependences of (a) the out-of-phase susceptibility, χ_M"(υ), and (b) the in-phase susceptibility, χ_M'(υ), under the indicated H_{dc} values, (c) the related Argand plots, χ_M"(χ_M'), and (d) the field dependence of the resulting relaxation times, τ. Colored solid curves in (a–c) represent the best fits obtained using the generalized Debye model for a single relaxation process. The blue solid line in (d) shows the simultaneous fit for both T and H dependencies of the relaxation time, while the dashed colored lines represent the respective course of each process included. The obtained best-fit parameters are gathered in Table S18.

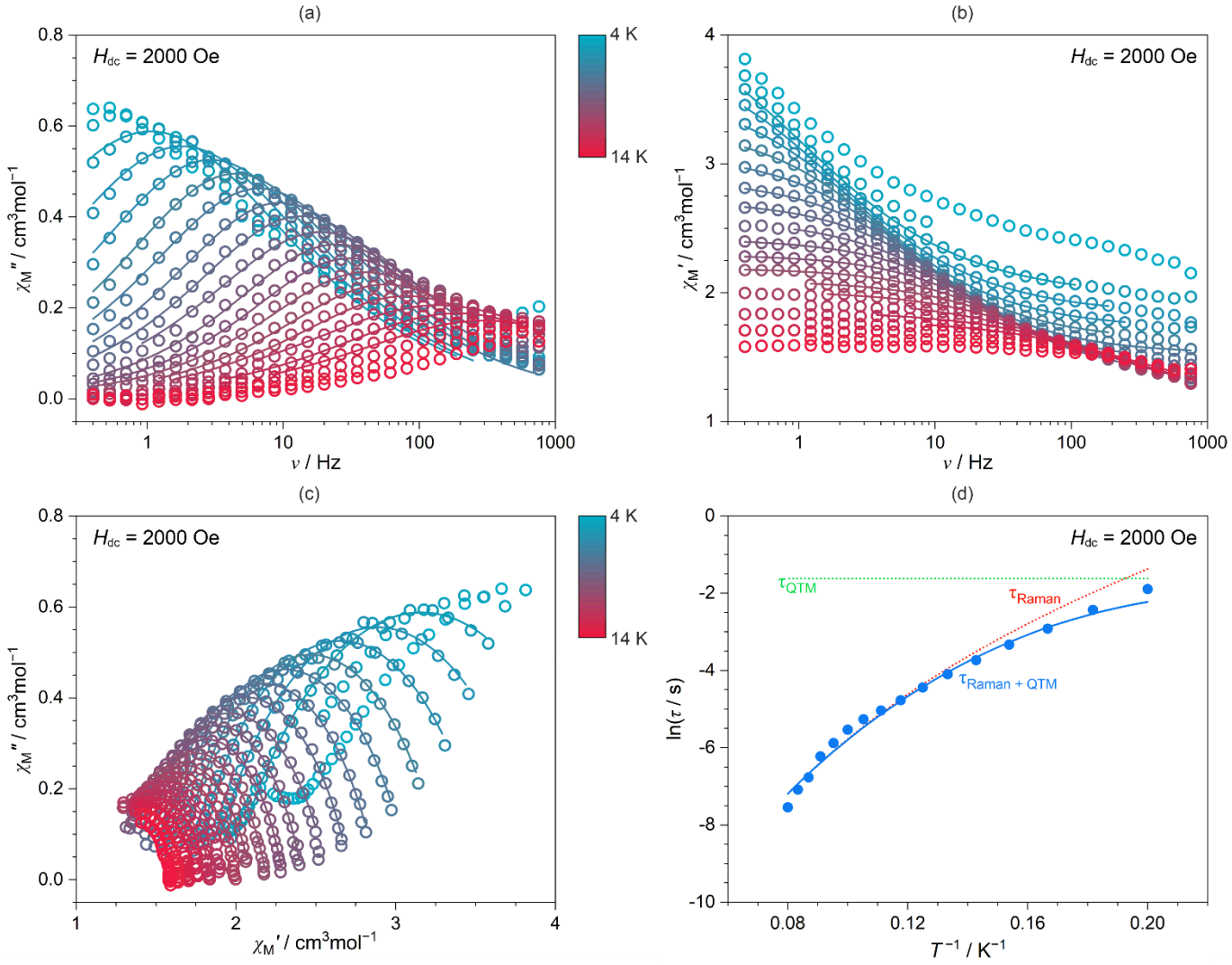

Fig. S38 Temperature-variable full *ac* magnetic characteristics of **3** under H_{dc} = 2 kOe, shown with the related analyses. This Fig. includes the frequency dependences of (a) the out-of-phase susceptibility, χ_M''(υ), and (b) the in-phase susceptibility, χ_M'(υ), collected in the indicated T regime, (c) the related Argand plots, χ_M''(χ_M'), and (d) the temperature dependence of the resulting relaxation times, τ. Colored solid curves in (a–c) represent the best fits obtained using the generalized Debye model for a single relaxation process. The blue solid line in (d) shows the simultaneous fit for both T and H dependencies of the relaxation time, while the dashed colored lines represent the respective course of each process included. The obtained best-fit parameters are gathered in Table S18.

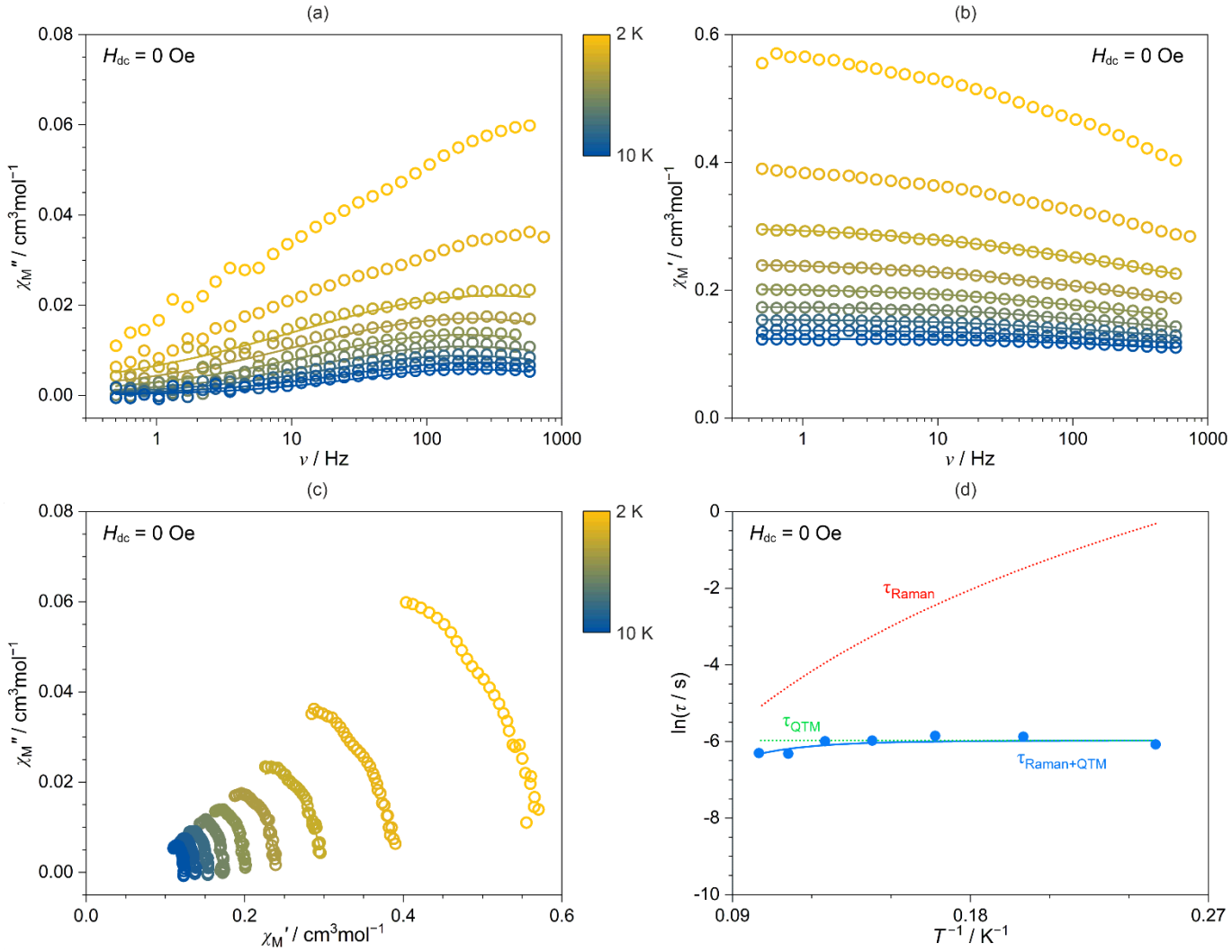

Fig. S39 Temperature-variable full *ac* magnetic characteristics of **3md** under zero *dc* field, shown with the related analyses. This Fig. includes the frequency dependences of (a) the out-of-phase susceptibility, χ_M''(υ), and (b) the in-phase susceptibility, χ_M'(υ), collected in the indicated T regime, (c) the related Argand plots, χ_M''(χ_M'), and (d) the temperature dependence of the resulting relaxation times, τ. Colored solid curves in (a–c) represent the best fits obtained using the generalized Debye model for a single relaxation process. The blue solid line in (d) shows the simultaneous fit for both T and H dependencies of the relaxation time, while the dashed colored lines represent the respective course of each process included. The obtained best-fit parameters are gathered in Table S18.

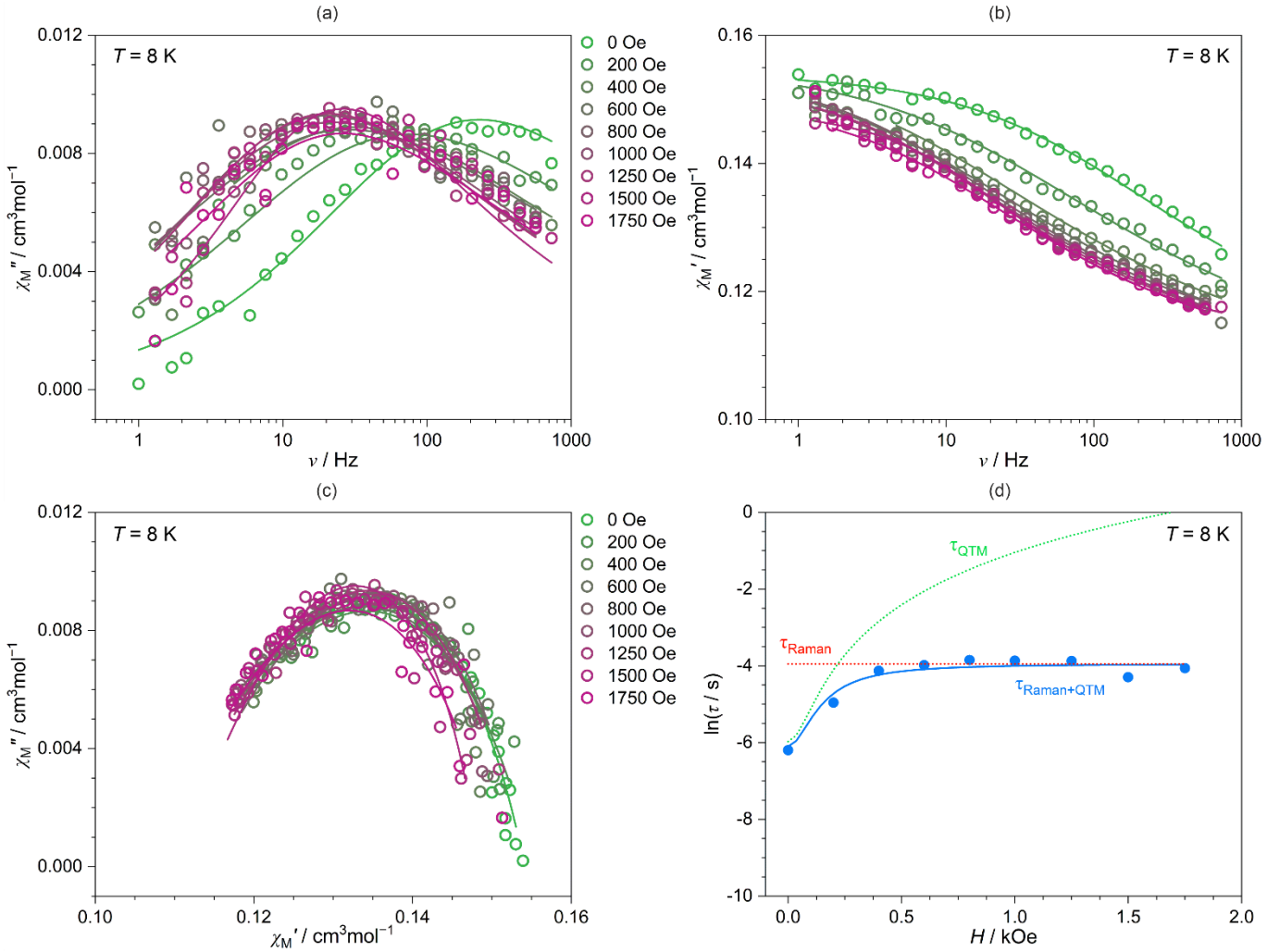

Fig. S40 Magnetic-field-variable full *ac* magnetic characteristics of **3md** at T = 8 K, shown with the related analyses. This Fig. includes the frequency dependences of (a) the out-of-phase susceptibility, χ_M"(υ), and (b) the in-phase susceptibility, χ_M'(υ), under the indicated H_{dc} values, (c) the related Argand plots, χ_M"(χ_M'), and (d) the field dependence of the relaxation time, τ. Colored solid curves in (a–c) represent the best fits obtained using the generalized Debye model for a single relaxation process. The blue solid line in (d) shows the simultaneous fit for both T and H dependencies of the relaxation time, while the dashed colored lines represent the respective course of each process included. The obtained best-fit parameters are gathered in Table S18.

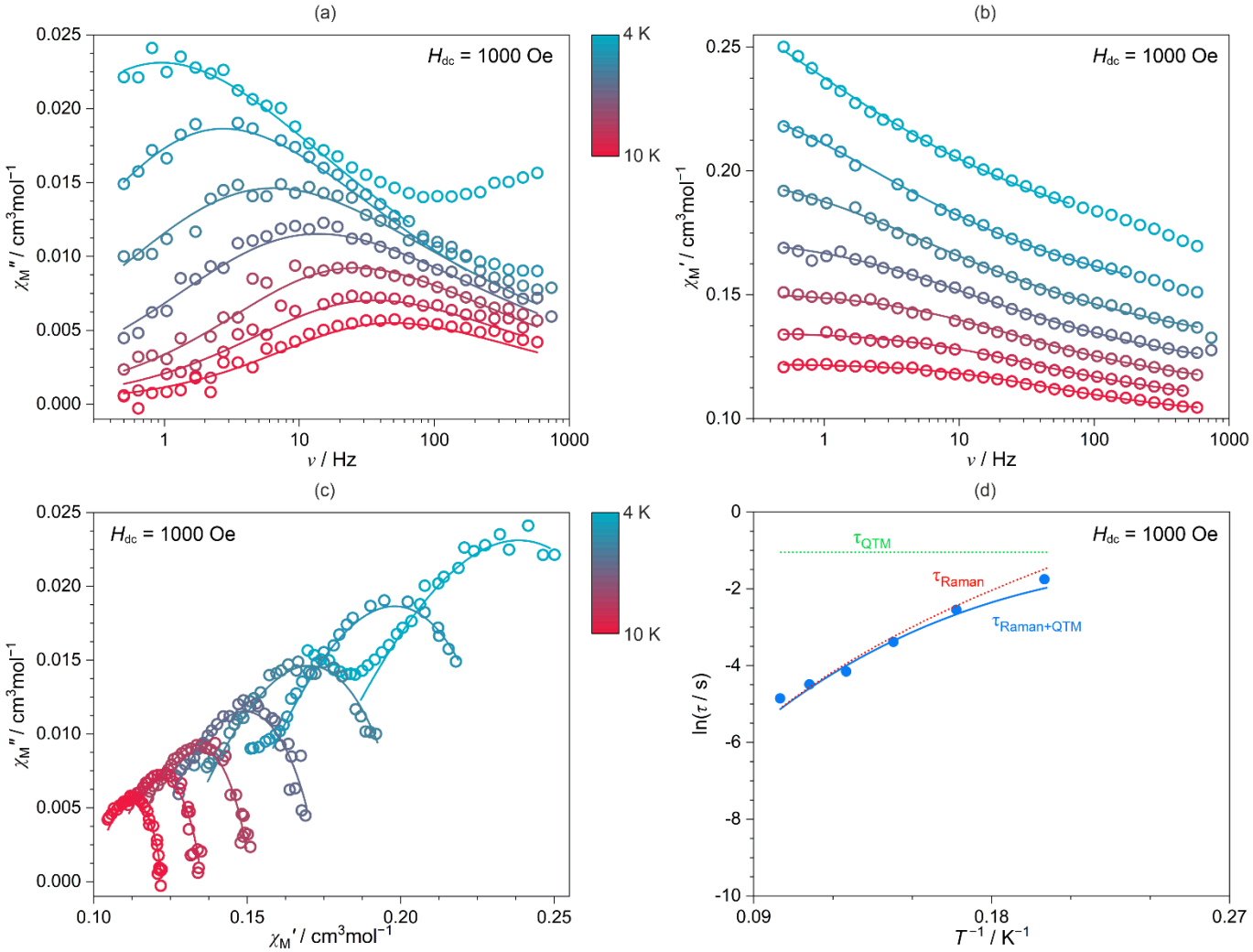

Fig. S41 Temperature-variable full *ac* magnetic characteristics of **3md** under H_{dc} = 1 kOe, shown with the related analyses. This Fig. includes the frequency dependences of (a) the out-of-phase susceptibility, χ_M''(υ), and (b) the in-phase susceptibility, χ_M'(υ), collected in the indicated T regime, (c) the related Argand plots, χ_M''(χ_M'), and (d) the temperature dependence of the resulting relaxation times, τ. Colored solid curves in (a–c) represent the best fits obtained using the generalized Debye model for a single relaxation process. The blue solid line in (d) shows the simultaneous fit for both T and H dependencies of the relaxation time, while the dashed colored lines represent the respective course of each process included. The obtained best-fit parameters are gathered in Table S18.

Table S18 Summary of the critical (best-fit) parameters of the relaxation processes determined for **3** and **3md**, obtained within the simultaneous fitting procedure of field and temperature dependencies of the relaxation time (see Fig. S37–S41 and the comment on Page S46), gathered together with the theoretical energy barriers obtained within the *ab initio* calculations performed using SC-XRD structural data collected for **3**.

compound	**3**	**3md**
A / $s^{-1}K^{-1}Oe^{-n}$	$3.7(8)\cdot10^{-15}$	—
B_1 / s^{-1}	$7.8(7)\cdot10^{7}$	$3.9(3)\cdot10^{2}$
B_2 / Oe^{-2}	3.9(4)	$1.5(3)\cdot10^{-4}$
C / $s^{-1}K^{-N}$	$1.43(5)\cdot10^{-5}$	$1.0(2)\cdot10^{-3}$
N	6.35(2)	5.24(2)
energy barrier values (ΔE), obtained from the *ab initio* calculations (smaller fragment, Table S15)	Dy1	92.7 cm^{-1}
	Dy2	76.5 cm^{-1}

Comment to Fig. S37–S41 and Table S18 – fitting of the *ac* magnetic data for 3 and 3md

Fitting procedure for 3 and 3md

The whole set of dependences for **3** was simultaneously fitted taking into account the Raman spin-lattice relaxation, the QTM effect, and the field-induced direct process. For **3md**, the inclusion of the direct process was found unnecessary, as the relaxation time drop was negligible for the highest fields. None of the parameters had to be constrained, and the fit was stable for both **3** and **3md**.

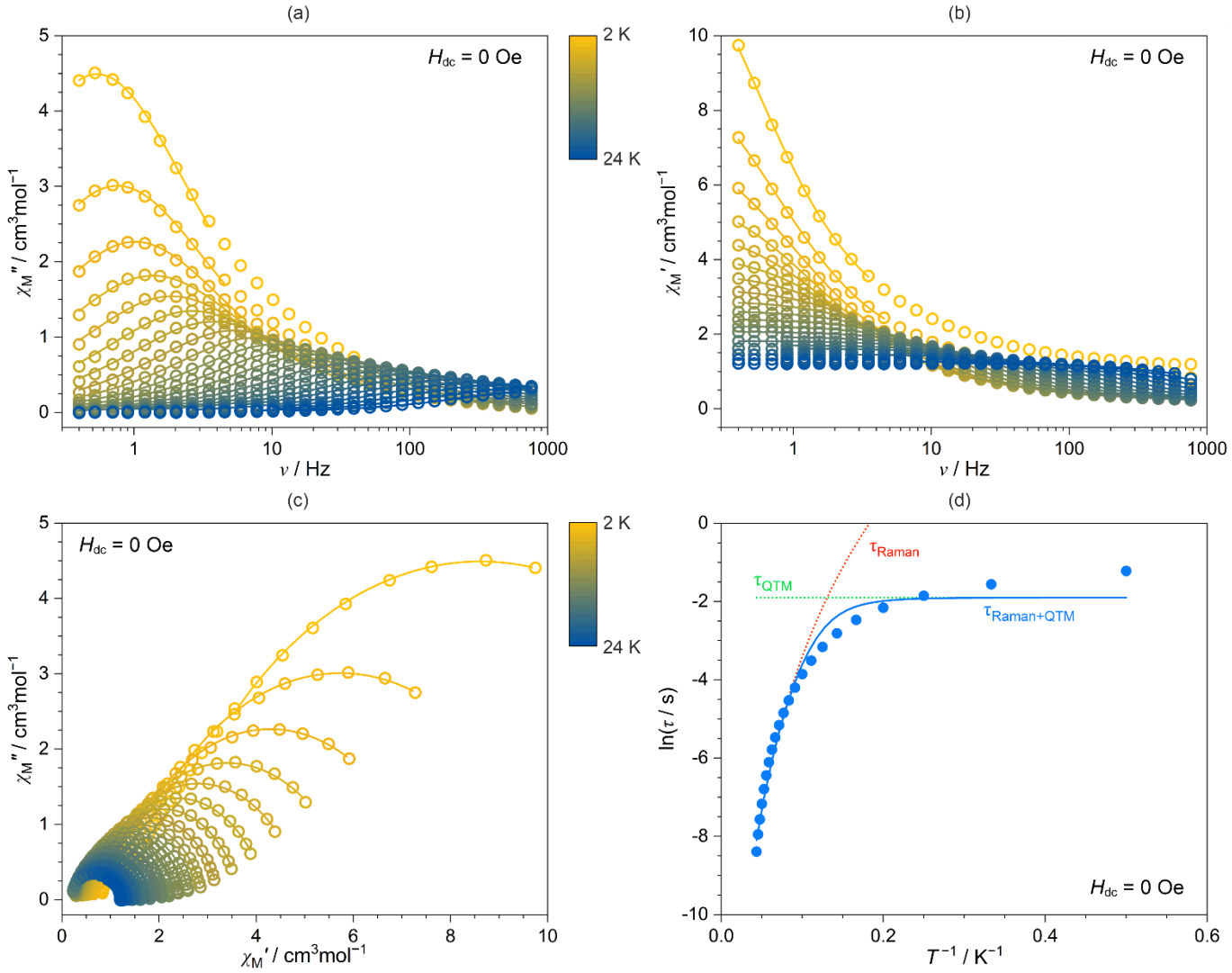

Fig. S42 Temperature-variable full *ac* magnetic characteristics of **4** under zero *dc* field, shown with the related analyses. This Fig. includes the frequency dependences of (a) the out-of-phase susceptibility, χ_M''(υ), and (b) the in-phase susceptibility, χ_M'(υ), collected in the indicated T regime, (c) the related Argand plots, χ_M''(χ_M'), and (d) the temperature dependence of the resulting relaxation times, τ. Colored solid curves in (a–c) represent the best fits obtained using the generalized Debye model for a single relaxation process. The blue solid line in (d) shows the simultaneous fit for both T and H dependencies of the relaxation time, while the dashed colored lines represent the respective course of each process included. The obtained best-fit parameters are gathered in Table S19.

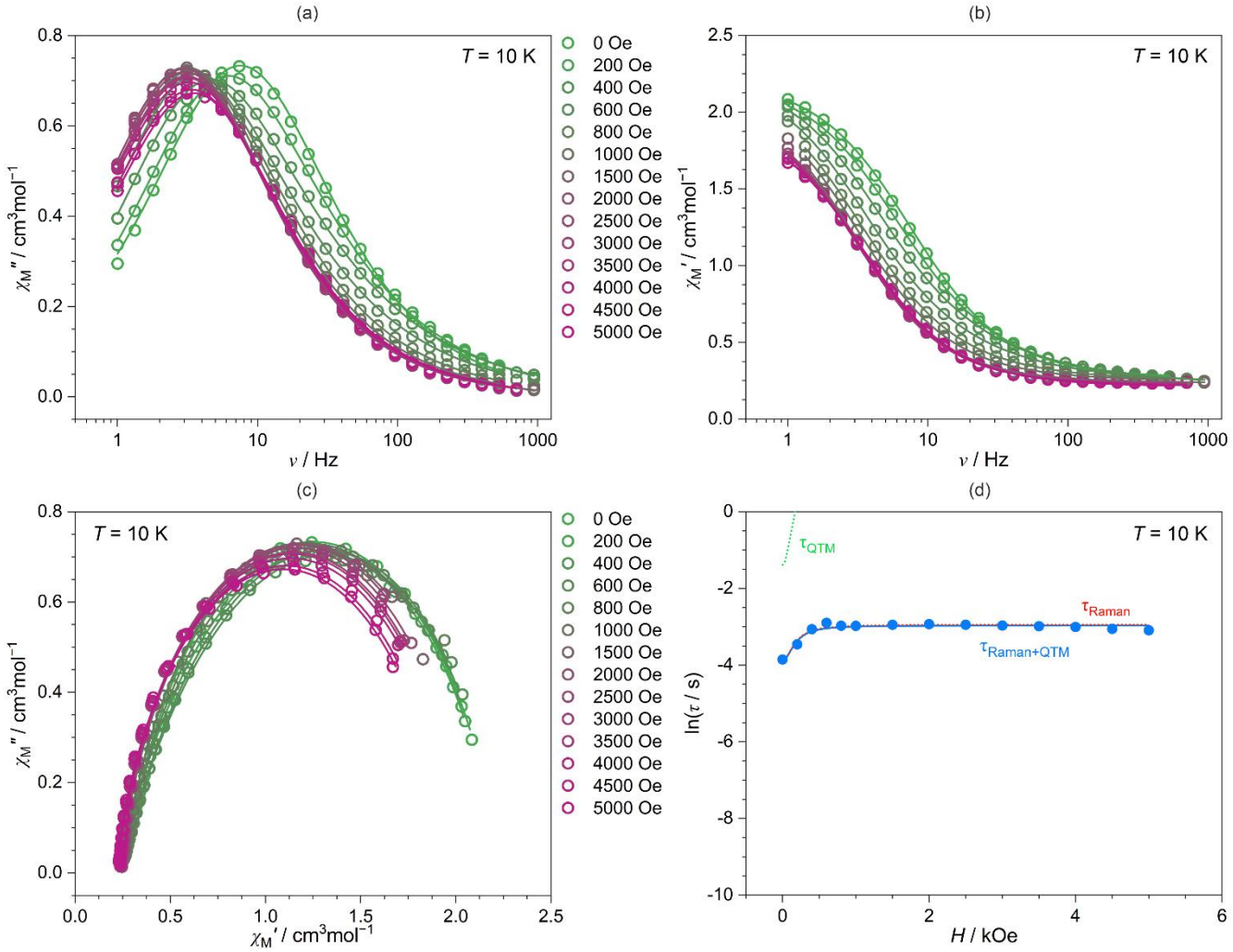

Fig. S43 Magnetic-field-variable full *ac* magnetic characteristics of **4** at $T = 10$ K, shown with the related analyses. This Fig. includes the frequency dependences of (a) the out-of-phase susceptibility, χ_M"(υ), and (b) the in-phase susceptibility, χ_M'(υ), under the indicated H_{dc} values, (c) the related Argand plots, χ_M"(χ_M'), and (d) the field dependence of the resulting relaxation times, τ. Colored solid curves in (a–c) represent the best fits obtained using the generalized Debye model for a single relaxation process. The blue solid line in (d) shows the simultaneous fit for both T and H dependencies of the relaxation time, while the dashed colored lines represent the respective course of each process included. The obtained best-fit parameters are gathered in Table S19.

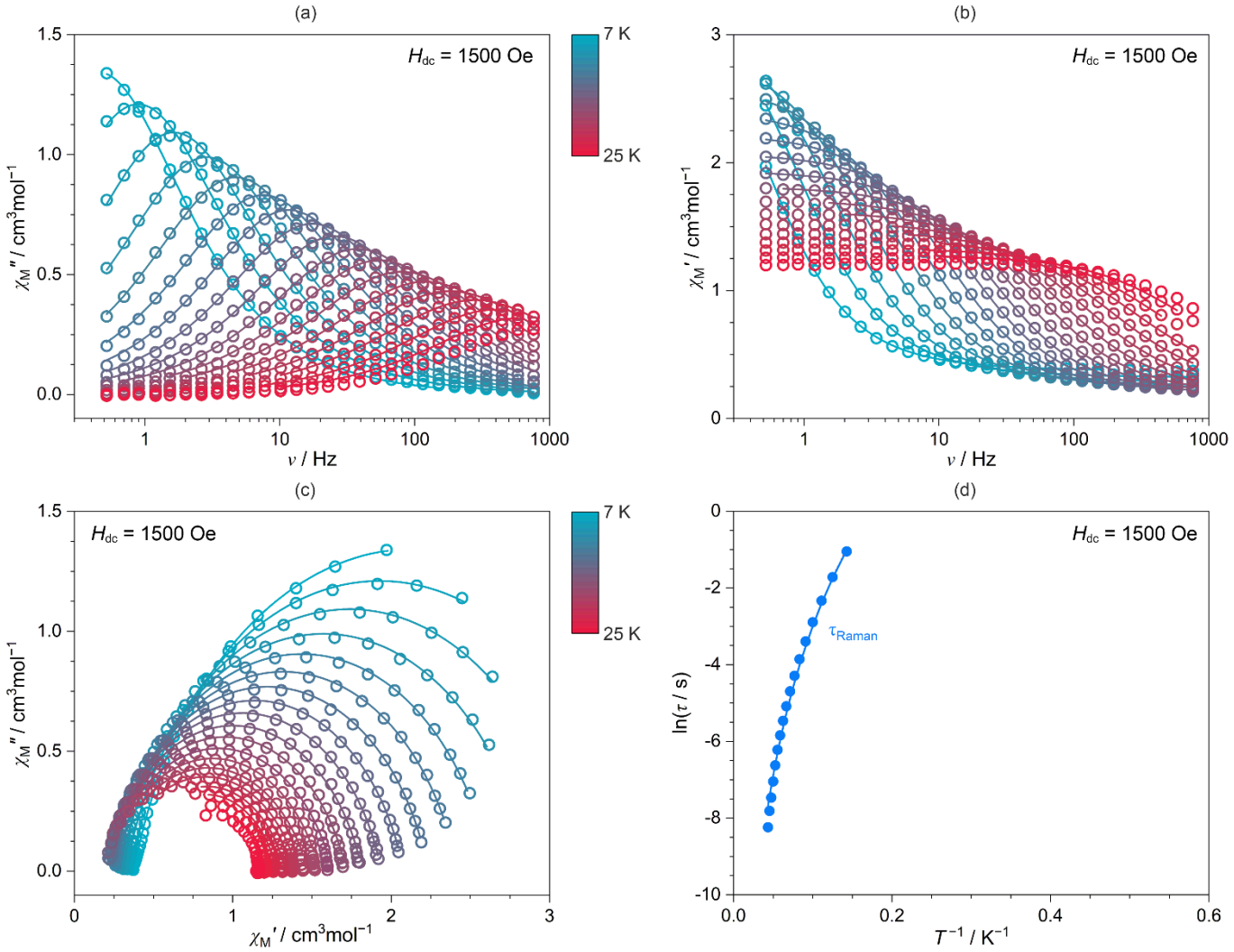

Fig. S44 Temperature-variable full *ac* magnetic characteristics of **4** under H_{dc} = 1.5 kOe, shown with the related analyses. This Fig. includes the frequency dependences of (a) the out-of-phase susceptibility, χ_M''(υ), and (b) the in-phase susceptibility, χ_M'(υ), collected in the indicated T regime, (c) the related Argand plots, χ_M''(χ_M'), and (d) the temperature dependence of the resulting relaxation times, τ. Colored solid curves in (a–c) represent the best fits obtained using the generalized Debye model for a single relaxation process. The blue solid line in (d) shows the simultaneous fit for both T and H dependencies of the relaxation time, while the dashed colored lines represent the respective course of each process included. The obtained best-fit parameters are gathered in Table S19.

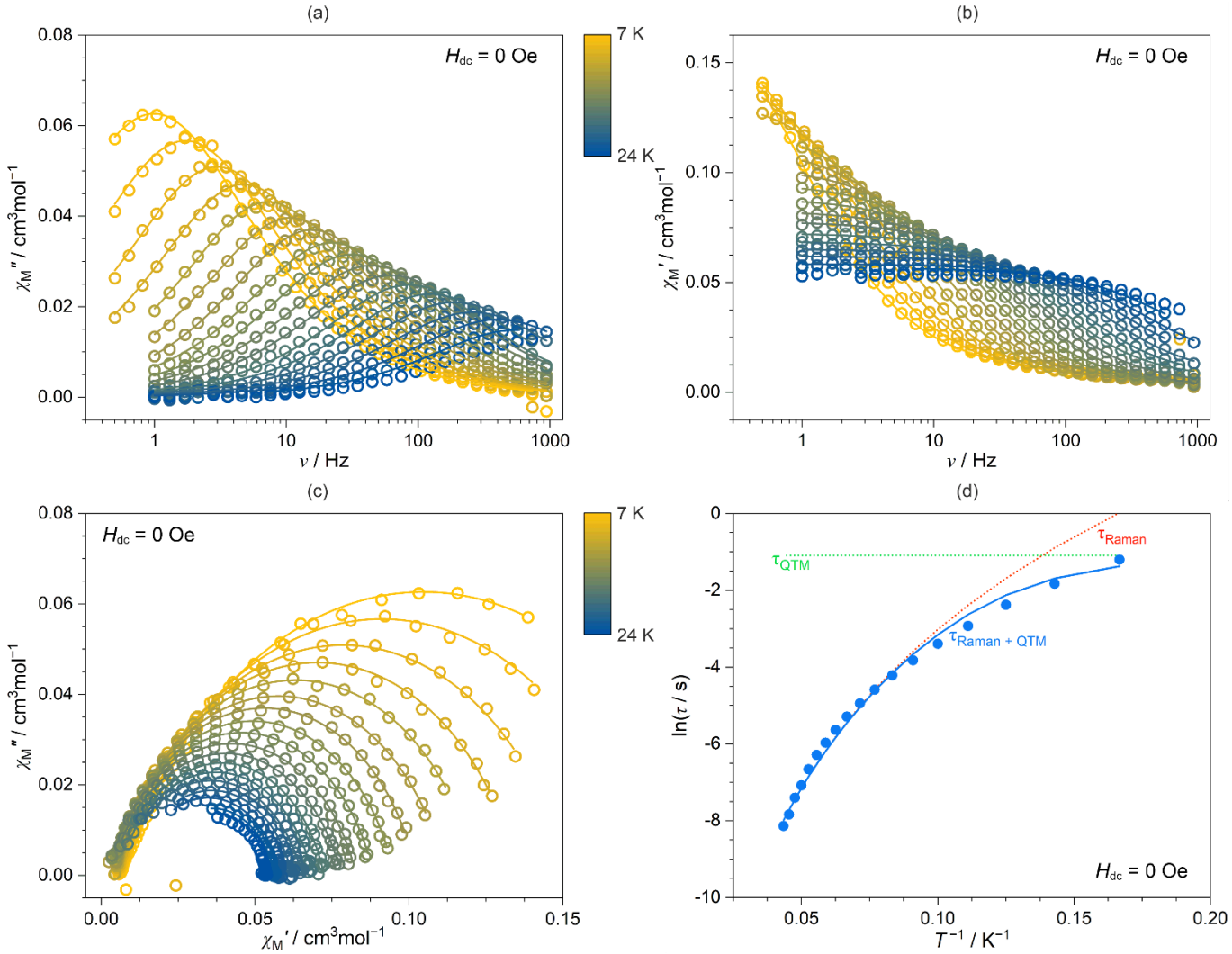

Fig. S45 Temperature-variable full *ac* magnetic characteristics of **4md** under zero *dc* field, shown with the related analyses. This Fig. includes the frequency dependences of (a) the out-of-phase susceptibility, χ_M''(υ), and (b) the in-phase susceptibility, χ_M'(υ), collected in the indicated T regime, (c) the related Argand plots, χ_M''(χ_M'), and (d) the temperature dependence of the resulting relaxation times, τ. Colored solid curves in (a–c) represent the best fits obtained using the generalized Debye model for a single relaxation process. The blue solid line in (d) shows the simultaneous fit for both T and H dependencies of the relaxation time, while the dashed colored lines represent the respective course of each process included. The obtained best-fit parameters are gathered in Table S19.

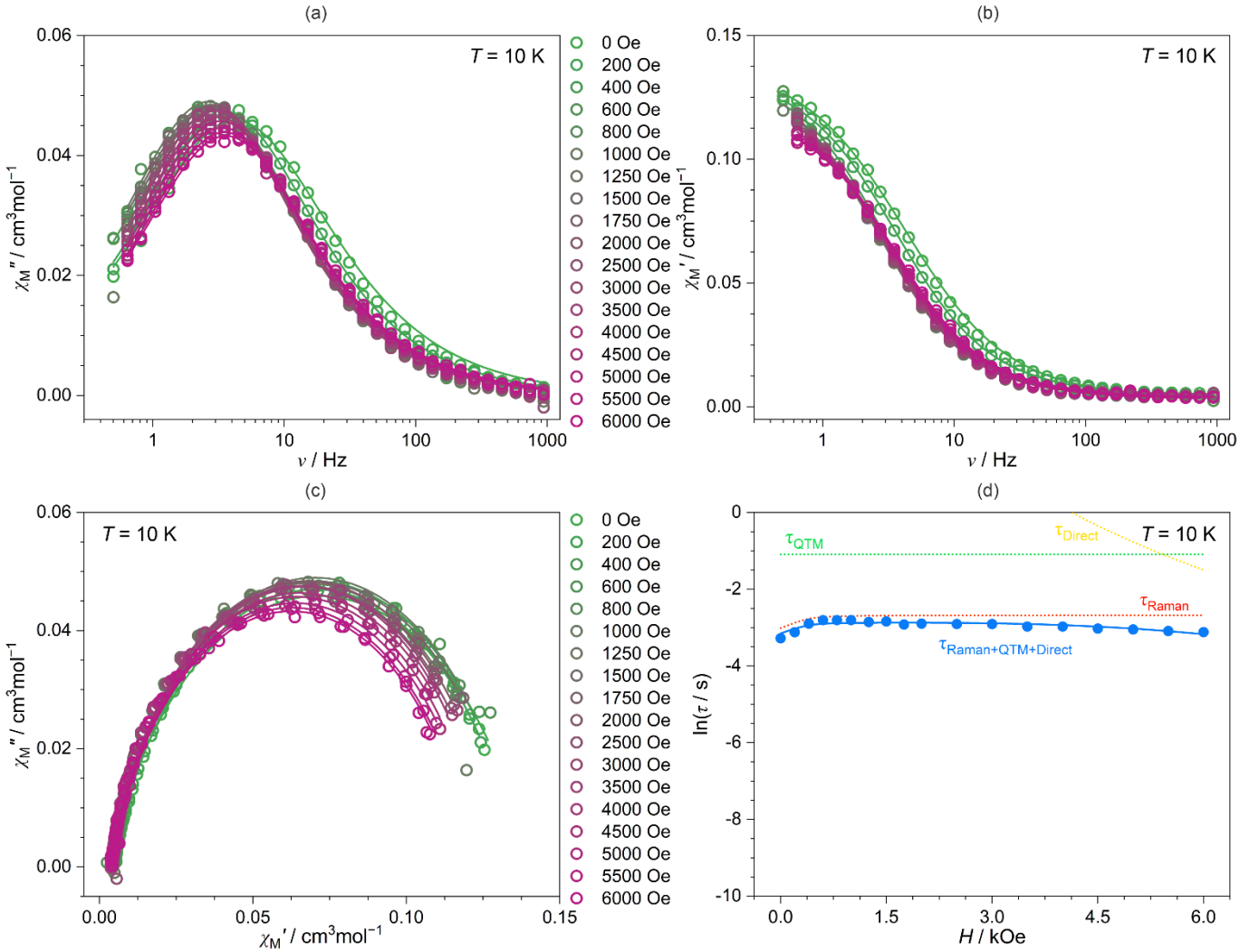

Fig. S46 Magnetic-field-variable full *ac* magnetic characteristics of **4md** at T = 10 K, shown with the related analyses. This Fig. includes the frequency dependences of (a) the out-of-phase susceptibility, χ_M"(υ), and (b) the in-phase susceptibility, χ_M'(υ), under the indicated H_{dc} values, (c) the related Argand plots, χ_M"(χ_M'), and (d) the field dependence of the resulting relaxation times, τ. Colored solid curves in (a–c) represent the best fits obtained using the generalized Debye model for a single relaxation process. The blue solid line in (d) shows the simultaneous fit for both T and H dependencies of the relaxation time, while the dashed colored lines represent the respective course of each process included. The obtained best-fit parameters are gathered in Table S19.

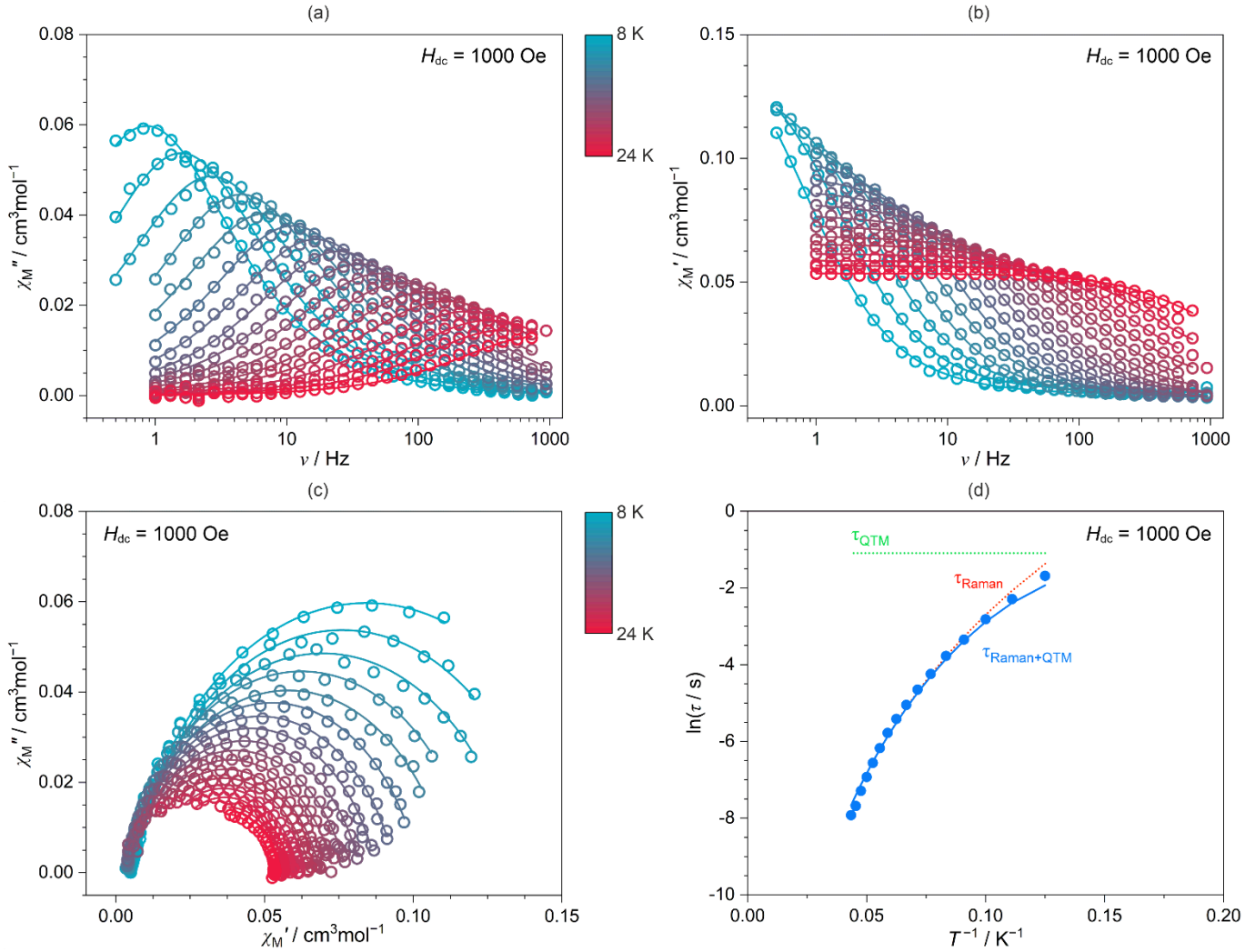

Fig. S47 Temperature-variable full *ac* magnetic characteristics of **4md** under H_{dc} = 1 kOe, shown with the related analyses. This Fig. includes the frequency dependences of (a) the out-of-phase susceptibility, χ_M''(υ), and (b) the in-phase susceptibility, χ_M'(υ), collected in the indicated T regime, (c) the related Argand plots, χ_M''(χ_M'), and (d) the temperature dependence of the resulting relaxation times, τ. Colored solid curves in (a–c) represent the best fits obtained using the generalized Debye model for a single relaxation process. The blue solid line in (d) shows the simultaneous fit for both T and H dependencies of the relaxation time, while the dashed colored lines represent the respective course of each process included. The obtained best-fit parameters are gathered in Table S19.

Table S19 Summary of the critical (best-fit) parameters of the relaxation processes determined for **4** and **4md**, obtained within the simultaneous fitting procedure of field and temperature dependencies of the relaxation time (see Fig. S42–S47 and the comment on Page S46). No comparison with the results of the *ab initio* calculations was accessible for this compound.

compound	**4**	**4md**
A / $s^{-1}K^{-1}Oe^{-n}$	—	$48(17)\cdot10^{-17}$
B_1 / s^{-1}	6.7(7)	3.0(3)
B_2 / Oe^{-2}	$3(9)\cdot10^{-5}$	0*
a / Oe^{-2}	$1.50(7)\cdot10^{-5}$	$1.62(5)\cdot10^{-5}$
b / Oe^{-2}	$2.3(1)\cdot10^{-5}$	$2.27(6)\cdot10^{-5}$
C / $s^{-1}K^{-N}$	$7.0(2)\cdot10^{-3}$	$2.22(5)\cdot10^{-5}$
N	5.63(1)	5.964(8)

*See Comment on Page S77.

Comment to Fig. S42-S47 and Table S19 – fitting of the *ac* magnetic data for 4 and 4md

Fitting procedure for 4 and 4md

Initially, an attempt was made to fit simultaneously the whole set of field- and temperature-dependences of relaxation times for **4** taking into account the Raman spin-lattice relaxation and QTM effect. As it was found impossible, the separate individual fits for temperature-dependences under zero *dc* field and H_{dc} = 1500 Oe were done using the relaxation pathways of the QTM effect and the Raman spin-lattice relaxation. From them, it was noted, that the parameters related to the Raman spin-lattice relaxation changed, especially the value of the *C* parameter. Knowing that, the equation of Raman spin-lattice relaxation was changed to Van Vleck's field-dependent one (see Comment on page S46), and the fitting procedure was redone, this time converging to a solution.
The fitting procedure for **4md** was analogous to that of **4**, but the field-induced direct process also had to be considered to reasonably reproduce the experimental data. For this compound, it was found impossible to reliably determine a field dependence of the QTM effect, as the relaxation time that it could be affected was outside the measured range, therefore the parameter B_2 was fixed at 0.

Additional comment on the concept of SMM-based coordination polymers exemplified by compounds 1–4

The obtained compounds **1**–**4** are coordination chains based on cyanido-bridged Dy(III) and Pt(II) centers where the lanthanide complexes were shown to reveal the SMM characteristics. Therefore, they can be treated as examples of SMM-based coordination frameworks. At the same time, it is well-known that coordination chains based on magnetically anisotropic metal complexes, including Dy(III) complexes, can also behave as so-called Single-Chain Magnets (SCMs).[S23,S24] This issue should be, thus, commented on.
The term ″Single-Chain Magnet (SCM)″ refers to the coordination systems based on magnetically coupled paramagnetic metal centers and/or organic radicals. Then, the slow relaxation of the magnetization effect results from the combination of intrinsic single-ion anisotropy of at least some of the employed metal centers and their efficient magnetic coupling with the neighboring metal centers usually placed within a coordination chain (other factors, such as magnetic isolation of these coordination chains within the crystal structure, also contribute to the high-performance SCM effect).[S23,S24]
In this context, the obtained compounds are indeed coordination chains but they are built of paramagnetic Dy(III) centers bearing substantial magnetic anisotropy and diamagnetic Pt(II)–cyanido metalloligands. The latter complex is thus used to magnetically isolate the Dy(III) centers within the coordination system. As a result, the observed slow magnetic relaxation effects are due to the properties of Dy(III) complexes, thus they are considered as Single-Molecule Magnets (SMMs). The only difference between the presented type of Dy(III) SMMs and broadly explored mononuclear Dy(III) molecules serving as SMMs is their incorporation in the more rigid coordination skeleton with organic ligands and cyanido-based metalloligands. Such an approach, relying on the construction of coordination polymers based on SMMs, has been already presented and discussed in the literature.[S25] In other words, the presented compounds are examples of coordination polymers incorporating Dy(III) SMMs linked by diamagnetic metalloligands which results in the slow magnetic relaxation characteristics assignable to the intrinsic property of each magnetically isolated Dy(III) complex.

Table S20 The set of representative results of the *ab initio* calculations for **4**, including the main magnetic axes alignment in relation to the axially aligned O-donor ligands, the energy difference between the first two doublets of the ground $^6H_{15/2}$ multiplet of indicated Dy(III) centers with pseudo-*g*-tensor components, and the composition of the ground doublet presented in the $|J = 15/2, m_J\rangle$ basis. Please note that these calculations are based on the structural model which is of a much lower quality than obtained for other reported compounds (see the comment on Page S80).

Dy1 center			
fragment/model		**S** (smaller fragment, see Comment on Page S39 and Table S12)	**B** (bigger fragment, see Comment on Page S39 and Table S12)
axis alignment		perpendicular	perpendicular
energy gap / cm^{-1}		93.4	9.0
pseudo-*g*-tensor	g_x	0.8913	1.0057
	g_y	3.7619	1.4662
	g_z	16.6222	17.6243
composition of the ground doublet		78.7% $\|-15/2\rangle$; 9.8% $\|-11/2\rangle$; 6.5% $\|+15/2\rangle$; 2.0% $\|-7/2\rangle$; 0.8% $\|-3/2\rangle$; 0.8% $\|+11/2\rangle$; 0.3% $\|+1/2\rangle$; 0.2% $\|-5/2\rangle$; 0.2% $\|-1/2\rangle$; 0.2% $\|+7/2\rangle$; 0.1% $\|+3/2\rangle$; 0.1% $\|+5/2\rangle$; 0.1% $\|+9/2\rangle$; 0.1% $\|+13/2\rangle$	67.2% $\|+15/2\rangle$; 12.8% $\|-15/2\rangle$; 7.4% $\|+11/2\rangle$; 3.0% $\|+3/2\rangle$; 2.1% $\|-1/2\rangle$; 1.9% $\|-11/2\rangle$; 1.9% $\|+7/2\rangle$; 1.3% $\|+5/2\rangle$; 0.7% $\|-3/2\rangle$; 0.5% $\|-5/2\rangle$; 0.4% $\|+13/2\rangle$; 0.3% $\|-9/2\rangle$; 0.3% $\|-7/2\rangle$; 0.2% $\|+9/2\rangle$; 0.1% $\|-13/2\rangle$

Dy2 center			
fragment/model		**S** (smaller fragment, see Comment on Page S39 and Table S12)	**B** (bigger fragment, see Comment on Page S39 and Table S12)
axis alignment		perpendicular	parallel
energy gap / cm^{-1}		62.4	77.7
pseudo-*g*-tensor	g_x	0.3510	0.0055
	g_y	0.9472	0.0120
	g_z	18.9098	19.5678
composition of the ground doublet		56.7% $\|-15/2\rangle$; 15.2% $\|+15/2\rangle$; 12.4% $\|-11/2\rangle$; 3.6% $\|-7/2\rangle$; 3.3% $\|+11/2\rangle$; 2.1% $\|-3/2\rangle$; 1.5% $\|+1/2\rangle$; 1.0% $\|+5/2\rangle$; 1.0% $\|+7/2\rangle$; 0.8% $\|+9/2\rangle$; 0.6% $\|-1/2\rangle$; 0.6% $\|+3/2\rangle$; 0.5% $\|-5/2\rangle$; 0.5% $\|+13/2\rangle$; 0.2% $\|-9/2\rangle$; 0.1% $\|-13/2\rangle$	87.9% $\|-15/2\rangle$; 7.4% $\|+15/2\rangle$; 2.4% $\|-11/2\rangle$; 1.5% $\|-9/2\rangle$; 0.2% $\|-7/2\rangle$; 0.2% $\|+11/2\rangle$; 0.1% $\|-13/2\rangle$; 0.1% $\|+9/2\rangle$

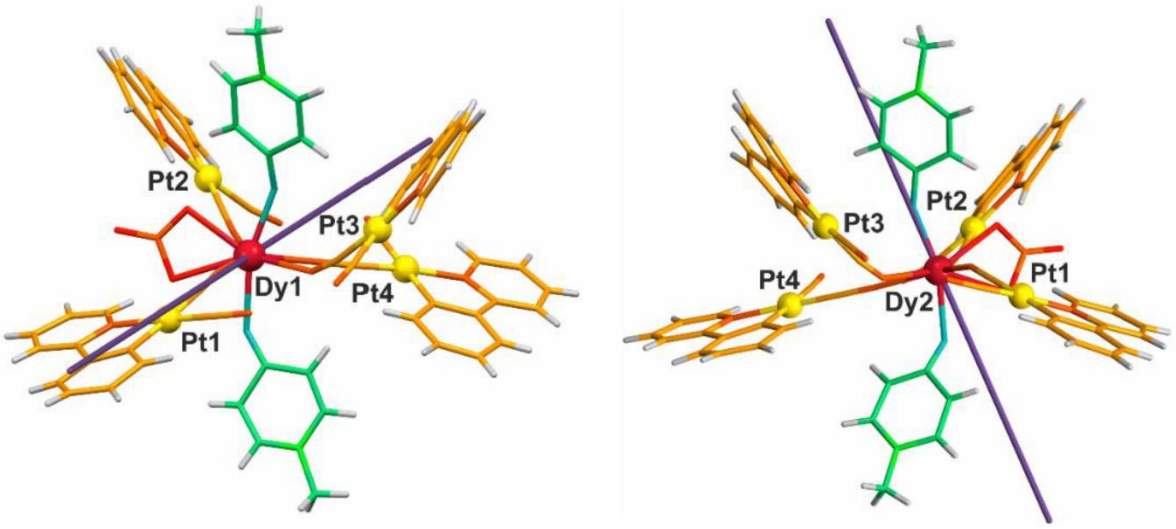

Fig. S48 The visualization of the structural fragments of **4** which were employed for the *ab initio* calculations of the crystal field effect upon the $^6H_{15/2}$ manifold of the Dy(III) centers. In (a) and (b), the bigger fragments (**B**) of the indicated Dy centers are presented (Table S20). The alignment of the magnetic easy axes, resulting from the *ab initio* analysis, is indicated by purple lines. Please note that these calculations are based on the structural model which is of a much lower quality than obtained for other reported compounds (see the comment below).

Comment to Table S20 and Fig. S48 – the results of *ab initio* calculations for 4

The presented results of the *ab initio* calculations should be considered and analyzed with caution. A significant structural disorder was found for the crystals of **4** which makes all the calculations based on the related structural model much less reliable than for the other compounds (see Tables S1 and S13–S15). Nevertheless, it was possible to proceed with the *ab initio* calculations following the same procedure as performed for **1**–**3**. The results are in line with the experimental data and results for relative compounds. The Dy2 center in **4** shows analogous properties to the Dy2 center in **2**, including distinct axial anisotropy, purity of states, and parallel alignment of the easy magnetization axis with the O-donor ligands for larger molecular fragments (compare Table S14 and Table S20). Analogously, the Dy1 center in **4** is rather similar to the Dy1 center in **2**, revealing much weaker magnetic anisotropy and a tiny energy barrier (compare Table S15 and Table S20). Therefore, it can be postulated that in the *ac* measurements of **4**, only the behavior of the Dy2 center is visible, explaining the presence of only one relaxation in the compound even though two crystallographically distinct magnetic centers are detected. However, as stated above, these results should be rather considered as the approximate ones as they are based on the structural model of a high structural disorder which can be of crucial importance for such subtle calculations as *ab initio* studies.

References to the Supporting Information

S1 M. M. Mdleleni, J. S. Bridgewater, R. J. Watts and P. C. Ford, Synthesis, structure, and spectroscopic properties of ortho-metalated platinum (II) complexes, *Inorg. Chem.*, 1995, **34**, 2334–2342.

S2 J. Forniés, S. Fuertes, J. A. López, A. Martín and V. Sicilia, New Water Soluble and Luminescent Platinum(II) Compounds, Vapochromic Behavior of $[K(H_2O)][Pt(bzq)(CN)_2]$, New Examples of the Influence of the Counterion on the Photophysical Properties of d^8 Square-Planar Complexes, *Inorg. Chem.*, 2008, **47**, 7166–7176.

S3 P. Beak and J. Bonham, The Deuteration of Some N-Methyl-4-pyridones, *J. Am. Chem. Soc.*, 1965, **87**, 3365–3371.

S4 G. M. Sheldrick, SHELXS-97 and SHELXL-97, Program for crystal structure solution, University of Göttingen, Göttingen, Germany, 1997.

S5 G. M. Sheldrick, SHELXT – Integrated space-group and crystal-structure determination, *Acta Cryst.*, 2015, **A71**, 3–8.

S6 L. J. Farrugia, WinGX and ORTEP for Windows: an update, *J. Appl. Cryst.*, 2012, **45**, 849–854.

S7 S. Chorazy, J. J. Zakrzewski, J. Wang, S. Ohkoshi and B. Sieklucka, Incorporation of hexacyanidoferrate(III) ion in photoluminescent trimetallic Eu(3-pyridone)$[Co_{1-x}Fe_x(CN)_6]$ chains exhibiting tunable visible light absorption and emission properties, *CrystEngComm*, 2018, **20**, 5695–5706.

S8 M. Llunell, D. Casanova, J. Cirera, J. Bofill, P. Alemany, S. Alvarez, M. Pinsky and D. Avnir, SHAPE v. 2.1. Program for the Calculation of Continuous Shape Measures of Polygonal and Polyhedral Molecular Fragments, University of Barcelona, Barcelona, Spain, 2013.

S9 D. Casanova, J. Cirera, M. Llunell, P. Alemany, D. Avnir and S. Alvarez, Minimal distortion pathways in polyhedral rearrangements, *J. Am. Chem. Soc.*, 2004, **126**, 1755–1763.

S10 J. Rocha, C. D. S. Brites and L. D. Carlos, Lanthanide organic framework luminescent thermometers, *Chem. Eur. J.*, 2016, **22**, 14782–14795.

S11 I. F. Galvam, M. Vacher, A. Alavi, C. Angeli, F. Aquilante, J. Autschbach, J. J. Bao, S. I. Bokarev, N. A. Bogdanov, R. K. Carlson, L. F. Chibotaru, J. Creutzberg, N. Dattani, M. G. Delcey, S. S. Dong, A. Dreuw, L. Freitag, L. M. Frutos, L. Gagliardi, F. Gendron, A. Giussani, L. Gonzalez, G. Grell, M. Guo, C. E. Hoyer, M. Johansson, S. Keller, S. Knecht, G. Kovacevic, E. Kallman, G. L. Manni, M. Lundberg, Y. Ma, S. Mai, J. P. Malhado, P. A. Malmqvist, P. Marquetand, S. A. Mewes, J. Norell, M. Olivucci, M. Oppel, Q. M. Phung, K. Perloot, F. Plasser, M. Reiher, A. M. Sand, I. Schapiro, P. Sharma, C. J. Stein, L. K. Sorensen, D. G. Truhlar, M. Ugandi, L. Ungur, A. Valentini, S. Vancoillie, V. Veryazov, O. Weser, T. A. Wesołowski, P.-O. Widmark, S. Wouters, A. Zech, J. P. Zobel and R. Lindh, OpenMolcas: From source code to insight, *J. Chem. Theory Comput.*, 2019, **15**, 5925–5964.

S12 B. O. Roos, R. Lindh, P.-Å. Malmqvist, V. Veryazov and P.-O. Widmark, Main group atoms and dimers studied with a new relativistic ANO basis set, *J. Phys. Chem. A*, 2004, **108**, 2851–2858.

S13 B. O. Roos, R. Lindh, P.- Å. Malmqvist, V. Veryazov and P.-O. Widmark, New relativistic ANO basis sets for transition metal atoms, *J. Phys. Chem. A*, 2005, **109**, 6575–6579.

S14 B. O. Roos, R. Lindh, P.-A. Malmqvist, V. Veryazov and P.-O. Widmark, A. C. Borin, New Relativistic Atomic Natural Orbital Basis Sets for Lanthanide Atoms with Applications to the Ce Diatom and LuF_3, *J. Phys. Chem. A*, 2008, **112**, 11431–11435.

S15 P. -Å. Malmqvist, B. O. Roos and B. Schimmelpfennig, The restricted active space (RAS) state interaction approach with spin–orbit coupling, *Chem. Phys. Lett.*, 2002, **357**, 230−240.

S16 B. A. Heß, C. M. Marian, U. Wahlgren and O. Gropen, A mean-field spin-orbit method applicable to correlated wavefunctions, *Chem. Phys. Lett.*, 1996, **251**, 365−371.

S17 L. F. Chibotaru and L. Ungur, Ab initio calculation of anisotropic magnetic properties of complexes. I. Unique definition of pseudospin Hamiltonians and their derivation, *J. Chem. Phys.*, 2012, **137**, 064112.

S18 L. Ungur and L. F. Chibotaru, Ab initio crystal field for lanthanides, *Chem. Eur. J.*, 2017, **23**, 3708–3718.

S19 M. Liberka, M. Zychowicz, W. Zychowicz and S. Chorazy, Neutral dicyanidoferrate(II) metalloligands for the rational design of dysprosium(III) single-molecule magnets, *Chem. Commun.*, 2022, **58**, 6381–6384.

S20 Y.-N. Guo, G.-F. Xu, Y. Guo and J. Tang, Relaxation dynamics of dysprosium (III) single molecule magnets,

Dalton Trans., 2011, **40**, 9953–9963.

S21 S. T. Liddle and J. van Slageren, Improving f-element single molecule magnets, *Chem. Soc. Rev.*, 2015, **44**, 6655─6669.

S22 D. Errulat, K. L. M. Harriman, D. A. Gálico, A. A. Kitos, A. Mansikkamäki and M. Murugesu, A trivalent 4f complex with two bis-silylamide ligands displaying slow magnetic relaxation, *Nat. Chem.*, 2023, **15**, 1100─1107.

S23 L. Bogani, A. Vindigni, R. Sessoli and D. Gatteschi, Single chain magnets: where to from here?, *J. Mater. Chem.*, 2008, **18**, 4750–4758.

S24 H.-L. Sun, Z.-M. Wang and S. Gao, Strategies towards single-chain magnets, *Coord. Chem. Rev.*, 2010, **254**, 1081–1100.

S25 K. Liu, X. Zhang, X. Meng, W. Shi, P. Cheng and A. K. Powell, Constraining the coordination geometries of lanthanide centers and magnetic building blocks in frameworks: a new strategy for molecular nanomagnets, *Chem. Soc. Rev.*, 2016, **45**, 2423–2439.